Many-body interactions in a dissipative frozen strontium Rydberg gas

DANIEL PAUL SADLER

Durham University

Doctoral Thesis

Many-Body Interactions in a Dissipative Frozen Strontium Rydberg Gas

Author: Daniel P. Sadler

Supervisor: Dr. Matthew P.A. Jones

Second Supervisor: Prof. Charles S. Adams

A thesis submitted in fulfilment of the requirements for the degree of Doctor of Philosophy

in the

Joint Quantum Centre
Department of Physics

December 2016

Declaration of Authorship

I confirm that no part of the material offered has previously been submitted by myself for a degree in this or any other University. Where material has been generated through joint work, the work of others has been indicated.

Daniel Paul Sadler
December 2016

This work was funded through an EPSRC Doctoral Studentship.

DURHAM UNIVERSITY

Abstract

Faculty of Science
Department of Physics

Doctor of Philosophy

Many-Body Interactions in a Dissipative Frozen Strontium Rydberg Gas

by Daniel P. Sadler

This thesis describes an investigation of Rydberg excitation within a high-density sample (up to $\sim 10^{12}\,\mathrm{cm}^{-3}$) of cold ($\sim 10\,\mu\mathrm{K}$) strontium atoms. This sample is prepared using a two-stage magneto-optical trap, cooling first on a broad singlet transition and then a narrow triplet transition. Rydberg atoms are then created using a two-photon, three-level ladder type scheme and detected using a novel autoionisation technique. It is shown that, in the regime of high optical thickness on the probing transition, a significant Rydberg population can be created by photons that are multiply scattered before leaving the cloud.

The multiply scattered field is density-dependent and has strikingly different spectral properties from the incident laser light. This spectrum is convolved with the spectrum of the Rydberg atoms created via direct laser excitation and the two spectra can be isolated in post analysis. This technique provides a probe of the spectral distribution of the re-scattered light *within* the cloud, which may be qualitatively different from that of the transmitted light, and previously has not been measured directly. Additionally, this Rydberg population arising from the multiply scattered field can be seen in the spatial distribution of the Rydberg excitations within the atom sample. Finally, a careful analysis of the time dynamics of the Rydberg system reveals that multiple scattering co-exists with signatures of the Rydberg blockade in this strongly dissipative regime.

Acknowledgements

Over my past four (plus) years in the Durham Atomic and Molecular Physics group I have been fortunate to meet a number wonderful and wonderfully ranty people. Chief among these is Dr. Matt Jones, who after guiding me through my Masters thesis decided rightly (or wrongly) to keep me around. I can honestly say that deciding to work for Matt on the strontium experiment was one of the best decisions I have ever made. I thank him for the patience and the support he has given me over the past 4 years. I would also like to thank Prof. Charles Adams and Dr. Bea Olmos for their help in understanding much of theory on which this thesis rests.

There is nothing quite like sharing a lab that has less than $10\,\mathrm{m}^2$ of floor space with up to 5 other people and I need to thank all of them: Dr. Graham Lochead, Dr. Dani Boddy, Dr. Elizabeth Bridge, Alistair Bounds, and Niamh Keegan. Graham was kind enough to show me the ropes as a fresh faced and annoying new starter. He taught me a significant chunk of what I know about the strontium experiment today and, more importantly, introduced me to JamJah. Dani was, and still, is a pillar of support and optimism who's healthy ways are finally rubbing off on me. I really could not have done any of this without her, we made a great team. Liz has the most patience of any person I have ever met and quickly realised I stopped talking if given chocolate. Her help and her friendship have been invaluable. Alistair and Niamh I have to thank for putting up with me during my final tyrannical months in the lab and for the great works they are continuing to produce.

Outside of the lab I quickly discovered that the Durham AtMol group is a uniquely friendly and helpful place to work. The amount I have learned in general conversation with Hannes Busche, David Paredes-Barato, David Schwer, Chris Wade, and Paul Huillery is really quite remarkable. Thanks for the insight you have all given me. While I am at it I suppose I should also thank Arin Mizouri and Kate Whittaker. These two were my co-conspirators in the founding of the FatMol cake club and office mates, alongside Hannes, in what has to have been the most talkative broom cupboard in history. Thanks for enabling me both of you.

Outside of the lab there are a legion of people I have to thank who kept me sane when equipment died, who humoured me while I excitedly talked physics at them in inappropriate places, and who kept me writing long after I had lost the will. Luke took the brunt of all of this and for that I will be forever sorry and eternally grateful. Finally, non of this would have been possible without the love and support of my parents. Without their support I could never have made it this far. Thank you for always being there when I needed you.

Contents

List of Figures

List of Tables

Chapter 1

Introduction

This thesis presents a study of Rydberg excitation within a laser cooled sample of strontium, an alkaline earth metal. While Rydberg physics has been studied extensively over the past century, the field has recently experienced a renaissance driven by the extremely strong interactions that can be engineered between Rydberg atoms. At the forefront of this revival is the research into many-body effects and more recently, the technological applications of these interacting systems within computing and metrology. Interest in such quantum technologies now extends far beyond the academic sphere, with the UK government recently intervening directly to provide significant funding to the field.

A Rydberg atom is an atom in which one or more valence electron has been excited to a high principle quantum number, normally where $n > 10$ [1]. The properties of such atoms scale strongly with n, for instance their atomic radii scale as n^2 and their radiative lifetimes scale as n^3 [2]. The induced dipole-dipole or Van der Waals (vdW) interactions between Rydberg atoms scale as n^{11}, allowing the creation of strong and tunable interactions between neutral atoms. These interactions allow entangled systems to be created via the 'Rydberg blockade' mechanism; whereby Rydberg excitation is suppressed by existing neighbouring Rydberg atoms within some macroscopic length scale known as the 'blockade radius'.

This new field has been driven by the ability to create long lived states via relatively simple laser excitation; the advent of frozen atomic samples where the interactions are dominant over thermal effects; and the development of narrow linewidth high power

short wavelength lasers. This has created new avenues into work on Rydberg photonics and quantum logic gates[3–5], hybrid quantum devices[6], and single atom transistors[7, 8]. This is alongside interest in their metrology applications, such as quantum sensing[9] and spin squeezing in optical lattice clocks[10].

In many of these works the figure of merit is the number of ground state atoms that sit within the blockade radius which necessitates high ground state densities. The aim of this work is to investigate the many-body effects associated with dense atomic gasses of strontium and explore the implications of this need for high optical depths. While optical depth effects and the physics of Rydberg atoms are discussed in more depth later in the thesis, it is worth motivating the choice of atomic strontium as the test bed for this work.

1.1 Strontium

Most research groups studying strontium have roots in the metrology field, where the fermionic isotope ^{87}Sr is a candidate for the next generation of optical clocks [11]. This is the only one of the stable strontium isotopes that has a nuclear spin of $I = 9/2$. All other stable isotopes of strontium are Bosonic and lack nuclear spin, giving them no hyperfine structure and making them an ideal system to model.

For the work presented in this thesis the crucial advantage that strontium confers is that it has two valence electrons. This 'divalent' nature means that strontium supports both singlet and triplet electronic spin states. While transitions between the singlet and triplet series states are dipole forbidden, state mixing effects make them weakly allowed. These weakly allowed transitions have very narrow linewidths and this property can be harnessed in numerous ways.

The weakly allowed $5s5p\,^3P_1$ state has a linewidth of only $2\pi \times 7.5\,\mathrm{kHz}$ and allows for all optical cooling of ^{88}Sr samples down to temperatures of 400 nK [12], these samples approaching the phase space densities required for Bose-Einstein condensation. This narrow line cooling technique compliments the robust slowing and cooling achievable via the $5s5p\,^1P_1$ state [13], which in stark contrast has a linewidth of $2\pi \times 30.2\,\mathrm{MHz}$ [14], and is invaluable for the production of ultra-cold samples when one considers the lack of sub-Doppler cooling in the Bosonic isotopes.

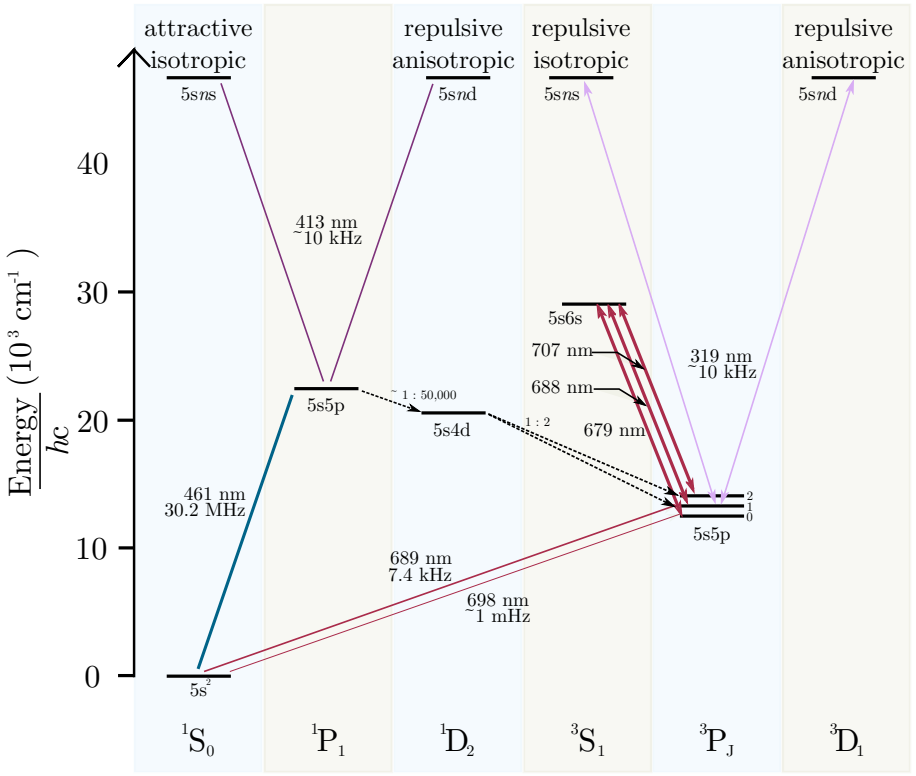

FIGURE 1.1: Key atomic energy levels in the ^{88}Sr isotope. Shown are the main cooling transitions at 461 nm and 689 nm, the clock transition at 698 nm, and the Rydberg excitation schemes via the $5s5p\,^1P_1$ state and $5s5p\,^3P_1$ state.

The triplet states have uses beyond sample preparation. The doubly forbidden $5s5p\,^3P_0$ state in ^{87}Sr has an even narrower linewidth, of the order of Hz, which is proving to be a viable future state of the atomic clock [15]. While the $5s5p\,^3P_2$ state is metastable [16] which could form an effective ground state. From this state triplet Rydberg atoms could be investigated with a single photon excitation. This thesis will focus on excitation via the $5s5p\,^1P_1$, using 461 nm and 413 nm radiation to access the $5sns\,^1S_1$ states. Previous work in the Durham group has used a similar scheme to access the $5snd\,^1D_2$ states. The highlighted states and excitation pathways can be seen in Figure 1.1 and progress towards exciting via the triplet states will be outlined.

Finally, aside from the triplet series and more uniquely to the Durham Strontium group, this divalent structure allows for the formation of doubly excited states. The excitation of these doubly excited atomic states can lead to the rapid ionisation of the atom. This controlled ionisation technique forms the basis of a novel Rydberg detection scheme with spatial, temporal, and atomic state resolution [9].

1.2 Outline

With the aim of the work and the motivation behind the use of strontium explored, the rest of this chapter will be used to explain the structure of the following document and outline the progress towards the stated aim.

An overview of the relevant Rydberg atom physics and how these systems are treated theoretically is presented in Chapter 2. This will focus on exploring the source of the long-range interactions for which Rydberg atoms are famed. Once this interaction is characterised, the three-level excitation scheme used to experimentally produce Rydberg states within this work will be introduced and excitation dynamics modelled for non-interacting clouds. This model will then be extended to include the Rydberg-Rydberg interactions and a technique introduced that allows the modelling of extended interacting samples. Results of these simulations are then introduced to show the types of physics that can be realised with achievable experimental parameters.

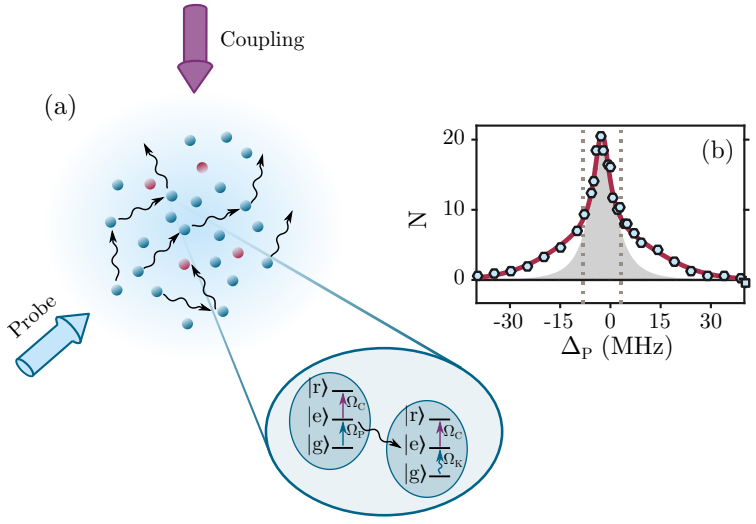

FIGURE 1.2: (a) A cartoon depicting a simplified experimental scenario. The probe and coupling lasers associated with Rydberg atom excitation are shown interacting with ground state atoms (blue) to excite Rydberg atoms (red) via the level scheme depicted. Crucial is that probe photons entering the cloud remain trapped (black curly arrows) and can lead to further Rydberg excitation, when a coupling beam is present. (b) An experimentally measured spectrum. The theoretical excitation spectrum is given by the grey shaded area, while the measured data points (blue circles) and a fit (red line) shows a clear departure. This departure is associated with Rydberg excitation via the trapped probe field.

The following chapter will be dedicated to explaining how the mechanics of such a Rydberg experiment work. Chapter 3 follows the life of an atom through the experimental cycle. From oven, to trap, to excitation, to detection. A discussion of the ground state

imaging techniques employed and how optically thick samples are treated is reserved for the end of the chapter.

With the effects of optical depth apparent at the end of Chapter 3, it is perhaps unsurprising that these effects form a key plank of Chapter 4, where the results of various experimental investigations are presented. While many-body interactions were the motivation for this work, it is the study of photon trapping within the atomic sample that is the key achievement of this work, with Rydberg atoms providing unlikely yet unique insight into the spectrum of the imprisoned photons. The key result of this thesis is summarised in Figure 1.2, in which an experimental summary is presented alongside a measured spectrum.

Alongside the identification of the trapped field, investigations into the spatial distribution of the Rydberg atoms were carried out. These investigations were consistent with the trapped photon field hypothesis. An investigation into the time dynamics of the Rydberg excitation was performed and hints of the many-body interaction observed.

Finally this thesis will conclude, consolidating the understanding gained in the course of this work, before outlining possible future directions for the Durham strontium experiment.

Chapter 2

Rydberg Atoms

As discussed in the previous chapter, the experimental production of cold Rydberg samples is the cornerstone of this work. This chapter will motivate the use of Rydberg atoms and outline the interesting effects arising from their strong inter-atomic interactions. After a brief outline of the coherent excitation scheme used in this work, it will then go on to explore two methods of theoretically modelling the excitation dynamics of such ensembles. The first of these a full optical-Bloch treatment, and then with a reduced rate equation Monte Carlo method.

2.1 Divalent Rydberg Atoms

While much of the Rydberg field focuses on one electron Rydberg atoms utilising atomic rubidium, this work focuses on strontium and two-electron Rydberg atoms. As discussed previously this additional valance electron allows for novel detection techniques, such as autoionisation [17], and the possibility of creating doubly excited states [18]. In both one-electron and two-electron neutral atoms, an understanding of the energy level structure and transition dipole matrix-elements of the states is required before the interactions between Rydberg atoms can be considered.

2.1.1 Rydberg Wavefunctions

If one restricts the problem to a single Rydberg excitation, then it is possible to treat one and two-electron Rydberg atoms in a similar way. By considering the Schrödinger

equation for a free electron moving within a potential, one can define a wavefunction. Applying the dipole operator to the wavefunction of the initial and final atomic states then yields the dipole matrix-elements.

The calculation of these wavefunctions is discussed extensively in [19] where they are calculated via the introduction of a model potential. Here one uses experimentally measured energy levels to extract the quantum defect δ via

$$E = \frac{R_{\mathrm{Sr}}}{(n-\delta)^2}, \tag{2.1}$$

where E is the energy of the atomic state, R_{Sr} is the strontium Rydberg constant, and n is the principal quantum number. Intuitively, if we view the atom as an electron bound to a core consisting of the nucleus shielded by the remaining electrons, this quantum defect is the increase in binding energy associated with the penetration of the Rydberg electron into this core.

As the variation of the quantum defect is slow and smooth, one can use the Rydberg-Ritz formula [20] to fit experimentally determined quantum defects and extrapolate over that entire Rydberg series. Then, to calculate the wavefunction, one has to define a potential that reproduces these quantum defects and numerically solve the Schrödinger equation for this potential to yield the wavefunctions. This method is only valid for large principle quantum numbers $n > 20$. If one wishes to consider lower states, or doubly excited states, then multi-channel quantum defect theory can be employed. Such calculations have been performed in Durham [21, 22] but are beyond the scope of this thesis.

2.1.2 Rydberg-Rydberg Interactions

Armed with Rydberg transition dipole matrix elements, it is now possible to predict the interaction between two Rydberg atoms. Considering two atoms separated by R, in the same initial state $|n_i l_i n_i l_i\rangle$, then the interaction Hamiltonian is given by

$$\mathscr{H} = \mathscr{H}_A + \mathscr{H}_{\mathrm{int}}(R), \tag{2.2}$$

where $\mathscr{H}_A$ is the Hamiltonian of the pair at infinite separation i.e with no interaction, and $\mathscr{H}_{int}(R)$ is the separation dependent interaction energy. As long as the separation

of the two atoms is great enough that the charge clouds do not spatially overlap [23], then it is sufficient to treat the system perturbatively, expanding the interaction as a series of multipoles [24]. The point at which the charge clouds overlap is known as the LeRoy radius [25], at this point molecular bound states begin to appear and the multipole expansion breaks down.

Grouping the powers of R following this multipole expansion leads to an expression for the interaction energy shift:

$$\Delta E = \sum_N \frac{C_N}{R^N}. \tag{2.3}$$

The first term in the expansion is C_3, which represents the first order dipole-dipole resonant interaction, but does not couple states of the same l and is therefore zero. Of the remaining terms the largest is the C_6 second order dipole-dipole interaction, the van der Waals interaction. Over the separations of interest within this work, the vdW interaction is dominant.

To calculate the interaction energy associated with the vdW interaction, the C_6 coefficient must be calculated. This term represents the coupling between the initial state of the two atoms and all possible final states, given by:

$$C_6 = -\sum_{\substack{n_{f1},l_{f1}\\ n_{f2},l_{f2}}} \frac{\langle n_{i1}l_{i1}n_{i2}l_{i2}|\hat{r}_1\hat{r}_2|n_{f1}l_{f1}n_{f2}l_{f2}\rangle\langle n_{f1}l_{f1}n_{f2}l_{f2}|\hat{r}_1\hat{r}_2|n_{i1}l_{i1}n_{i2}l_{i2}\rangle}{\Delta_{n_{i1}l_{i1}n_{i2}l_{i2}n_{f1}l_{f1}n_{f2}l_{f2}}}\,, \tag{2.4}$$

where the initial states of the atom pair are $n_{i1/2}$ and $l_{i1/2}$ and $n_{f1/2}$ and $l_{f1/2}$ are the final states. $\hat{r}_k$ represents the dipole operator, calculating the dipole matrix-elements, in atomic units.

So far we have neglected any discussion of atomic m_j states. While the C_6 coefficient sets the maximum interaction strength, $m_j \neq 0$ states cannot be treated as spherically symmetric and the interaction energy of the pair state therefore becomes angle dependent. This angle dependent modification can be reduced to a multiplicative factor, D_Θ, that is bounded between 0 and 1. For each set of initial magnetic sub-levels there will be a different D_Θ, the analytic expression for this parameter can be found in [26].

As this work focuses on the spherically symmetric S states we will not use D_Θ. But looking back at Equation 2.4 we see that each term in the sum is inversely proportional to its associated energy defect (Δ). The pair state that is closest to the initial pair

state in energy is therefore the term that dominates the interaction, setting its sign. In strontium the $5sns\,^1S_0$ states are calculated to exhibit attractive interactions, while the $5snd\,^1D_2$ series has repulsive interactions [22]. This spherically symmetric and attractive S state is utilised in this work and represents a departure from experiments within rubidium, where the spherically symmetric state is repulsive.

2.1.3 Rydberg Blockade

With the interaction between the Rydberg states introduced, it is worth looking at two manifestations of these interactions. The first of these is the 'Rydberg blockade' outlined in the previous chapter, hence forth referred to as blockade, which is a phenomena that arises due to the vdW interaction between two neighbouring Rydberg atoms. As the atoms are brought closer together, the long-range interactions result in an energy shift of the doubly excited Rydberg state $|rr\rangle$. If this shift exceeds the bandwidth of the excitation, given by the largest broadening mechanism relevant to the excitation, then the doubly excited state is suppressed as one of the atoms is shifted out of resonance with the driving field [2, 27]. This effect is shown in Figure 2.1. The minimum separation between two neighbouring atoms in this regime is called the 'blockade radius' and is given by

$$R_B = \left(\frac{D_\Theta C_6}{\gamma_b}\right)^{\frac{1}{6}}, \tag{2.5}$$

where D_Θ is the angular dependence of the C_6 coefficient. This angular dependence can be neglected in the case of a spherically symmetric interaction, like that associated with the strontium $5sns\,^1S_0$ states. The bandwidth is given by γ_b and is normally set by the Rabi frequency of the driving field, although in the case of this work it is found to be the linewidth of the driving lasers.

As well as manifesting as density dependent suppression of excitation, the blockade can be linked to the appearance of collective Rabi oscillations. By definition, once the mean inter-atomic spacing of an ensemble drops below the blockade radius, the number of neutral atoms per 'blockade sphere' must exceed unity. In this case, the N atoms that lie within the blockade sphere can be thought of as sharing the single Rydberg excitation and forming a collective state $\frac{1}{\sqrt{N}}\sum_{n=1}^{N}|g_1,...,r_n,...,g_N\rangle$. This encapsulates the *superatom* model of Rydberg excitation and a key experimental signature of this

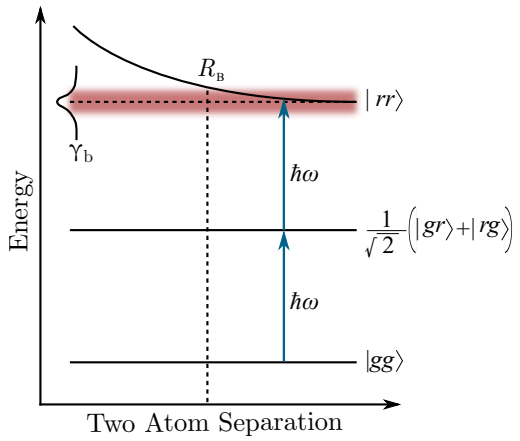

FIGURE 2.1: A diagram illustrating how the interaction shift leads to an excitation blockade. The solid black lines show the configuration energies as a function of two atom separation, while the horizontal dashed line shows the unperturbed energy of the $|rr\rangle$ state. The red shaded region shows the excitation bandwidth. The blockade radius, R_B is shown as the point whereby the interaction shift exceeds the excitation bandwidth.

collective state is an enhanced Rabi frequency given by $\sqrt{N}\Omega$ [27], where Ω is the single atom Rabi frequency.

2.2 Three-level Excitation

Rydberg excitation in this work uses the two-photon, three-level excitation scheme in a ladder configuration introduced in Figure 1.1. The relevant energy levels have been extracted and are shown in Figure 2.2, alongside a generalised ladder scheme. The use of a two-photon excitation scheme confers two main benefits. Firstly, it allows for a simpler experimental setup. The corresponding single photon transition straight to a Rydberg state would require laser radiation at 218 nm. While recent improvements in second harmonic generation capabilities and the new found affordability of Ti:Sapphire lasers make this feasible, the two stages of frequency doubling required quickly add expense and complexity. The second benefit is an increase in dipole allowed transitions. The two-photon scheme puts both S and D angular states within reach.

The first step is an excitation from the ground $5s^2\,{}^1S_0$ state $|g\rangle$ to the intermediate $5s5p\,{}^1P_1$ state $|e\rangle$ via 461 nm radiation, this driving laser will be referred to as the probe beam in the context of Rydberg excitation. A second photon at 413 nm is used to excite from the intermediate state to the final Rydberg $5sns\,{}^1S_0$ state $|r\rangle$, this second driving laser is referred to as the coupling beam. The strength of coupling between the

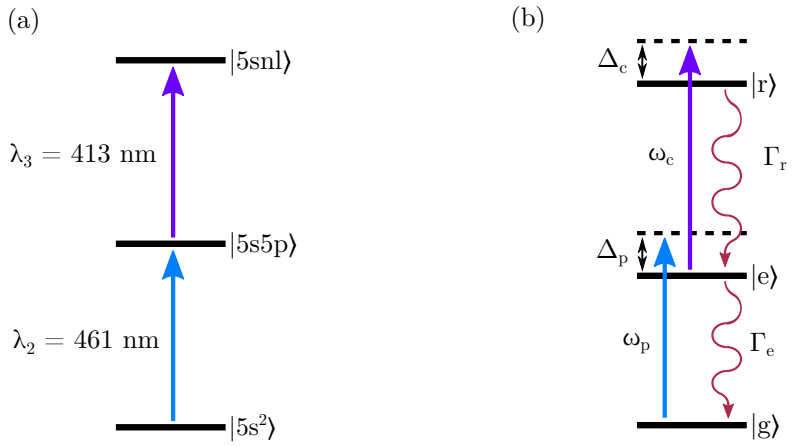

FIGURE 2.2: (a) Shows the actual states used in singlet excitation in our experiment and their approximate wavelengths. (b) Shows the driven three-level ladder system represented by the optical Bloch equation model presented later in the chapter. $|g\rangle$ is the ground state, $|e\rangle$ is the intermediate state, and $|r\rangle$ is the Rydberg state. The laser field ω_p, the probe laser, addresses the $|g\rangle \rightarrow |e\rangle$ transition and is detuned from resonance by Δ_p. A second laser field ω_c, the coupling laser, addresses the $|e\rangle \rightarrow |r\rangle$ transition and is detuned by Δ_p. The intermediate and Rydberg states decay naturally at the rates of Γ_e and Γ_r and the decay is assumed to be back to the originating state.

laser driven states is given by the Rabi frequency, defined as

$$\Omega_{ij} = \frac{eE_0}{\hbar}\langle i|\hat{r}|j\rangle \,, \tag{2.6}$$

where $\langle i|\hat{r}|j\rangle$ is the transition dipole matrix-element between the two states and E_0 is the magnitude of the maximum electric field due to the laser beam.

By writing the three states as $|g\rangle = (1,0,0)$, $|e\rangle = (0,1,0)$, $|r\rangle = (0,0,1)$ and coupling these states by the respective excitation laser Rabi frequencies $\Omega_{p,c}$, one can define the Hamiltonian as:

$$\mathscr{H} = \hbar \begin{pmatrix} 0 & \frac{\Omega_p}{2} & 0 \\ \frac{\Omega_p}{2} & -\Delta_p & \frac{\Omega_c}{2} \\ 0 & \frac{\Omega_c}{2} & -\Delta_p - \Delta_c \end{pmatrix}, \tag{2.7}$$

where $\Delta_{p,c}$ denotes the driving field detuning from the unperturbed state transition frequency, as shown in Figure 2.2. The Hamiltonian has been simplified by employing the rotating wave approximation, where one assumes that terms oscillating faster than the laser field average away and can be neglected [28].

This Hamiltonian only represents the coupling between the states due to the driving fields, if one is to model the excitation dynamics the spontaneous decay must also be

included, as must the finite spectral width of the driving fields themselves. To do this one must move to a density matrix formalism where:

$$\rho = \begin{pmatrix} \rho_{gg} & \rho_{ge} & \rho_{gr} \\ \rho_{eg} & \rho_{ee} & \rho_{er} \\ \rho_{rg} & \rho_{re} & \rho_{rr} \end{pmatrix}, \tag{2.8}$$

Here the diagonal terms are the state populations, ρ_{rr} being the population fraction in the Rydberg state, and the off-diagonal terms represent the absorption. With the Hamiltonian and density matrices defined one can then build a master equation using Lindblad operators to define the system dynamics:

$$\dot{\rho} = \frac{i}{\hbar}[\rho, \mathscr{H}] - \mathscr{L}(p) - \mathscr{L}_d(\rho), \tag{2.9}$$

where $\mathscr{L}$ are the Lindblad super-operators in the system. The first $\mathscr{L}$ accounts for spontaneous emission and has the form:

$$\mathscr{L}(p) = \begin{pmatrix} -\Gamma_e\rho_{ee} & \frac{1}{2}\Gamma_e\rho_{ge} & \frac{1}{2}\Gamma_{rg}\rho_{gr} \\ \frac{1}{2}\Gamma_e\rho_{eg} & \Gamma_e\rho_{ee} - \Gamma_r\rho_{rr} & \frac{1}{2}(\Gamma_e + \Gamma_r)\rho_{er} \\ \frac{1}{2}\Gamma_{rg}\rho_{rg} & \frac{1}{2}(\Gamma_e + \Gamma_r)\rho_{re} & \Gamma_r\rho_{rr} \end{pmatrix}. \tag{2.10}$$

The diagonal terms again redistribute population between the states and the off diagonal terms modify the coherences of the system. One can see that the inclusion of spontaneous emission from the intermediate state Γ_e, will quickly kill a coherence term if the state is driven strongly. It should also be noted that the coupling between the ground and Rydberg states is dipole forbidden such that Γ_{rg} is zero. Our second Lindblad super-operator encodes the finite linewidth of the driving laser fields and while this is of a phenomenological nature, the approach has been validated [29]. This operator is defined as:

$$\mathscr{L}_d(p) = \begin{pmatrix} 0 & \gamma_p\rho_{ge} & (\gamma_p + \gamma_c)\rho_{gr} \\ \gamma_p\rho_{eg} & 0 & \gamma_c\rho_{er} \\ (\gamma_p + \gamma_c)\rho_{rg} & \gamma_c\rho_{re} & 0 \end{pmatrix}, \tag{2.11}$$

where γ_i represent the respective finite laser linewidths, based upon the assumption that the laser spectral distribution is Lorentzian [30]. Here we should note that $\mathscr{L}_{d_{31/13}}$ become the sum of the driving laser linewidths as the result of convolving the two Lorentzian distributions and are now non-zero, as such they do lead to decoherence of the ground and Rydberg states. We have assumed in the model that the noise on $\gamma_{p/c}$ is uncorrelated. This is true on the short timescales relevant here but they are correlated on long time scales by the laser locking electronics.

2.2.1 Optical Bloch Equations

The set of equations containing Equation 2.7, 2.8, 2.9, 2.10, and 2.11 are collectively known as the optical Bloch equations (OBE). These equations can be solved numerically, in this case by using an adaptive time step ordinary differential equation solver, written in Fortran, and originally developed by John Pritchard [31]. This approach allows the population fractions to be calculated as a function of time for various system parameters and is used later in this work to both model and fit experimental data.

Several assumptions are made in the use of this treatment and the key ones are as follows:

- That the decay of the Rydberg state is only back to the intermediate state. While this is the most likely outcome, population can transfer to a wide range of dipole coupled singlet P or F states. Decay back to the intermediate state is dominant due to the ω^3 term appearing in the radiative decay rate favouring higher energy transitions.

- That the intermediate state decays only to the ground state. While there is a decay path to the $5s5d\,^1D_2$, this pathway has a branching ratio of $\sim 1:50,000$ and does not play a significant role in the dynamics.

- That there is no interaction term in the Hamiltonian. As previously mentioned, Rydberg atom ensembles exhibit strong, long-range interactions. Therefore, this treatment is only valid in the dilute excitation regime, such that the number of ground state atoms per blockade sphere $N \leq 1$.

While these assumptions hold, the model is a good fit to experimental data obtained, as is shown in Section 4.1.1. Unfortunately, in high density samples, the non-interacting assumption breaks down and this must be included if the model is to remain applicable to the samples explored within this thesis.

This model has been extended to the case of two interacting atoms. Interactions are incorporated through the addition of a position dependent interaction shift of the $|rr\rangle$ pair state, this interaction shift is characterised by the C_6. In this way one can calculate the probability of exciting the $|rr\rangle$ for any given separation and explore the associated excitation dynamics. Unfortunately, the basis set over which this model has to be solved does not scale favourably with the number of atoms N, with the size of the Hamiltonian scaling as 3^N. This makes the calculation computationally infeasible for large ensembles and other methods must be investigated if the system cannot be treated as non-interacting.

2.2.2 Rate Equation Treatment

One way of simplifying the computational task is to employ the rate equation methods described in the work [32]. The treatment sees the optical Bloch equations reduced from a series of coupled differential equations to a single rate equation describing the population of the Rydberg state. This treatment is only applicable under certain excitation conditions, namely that $\Omega_p \gg \Omega_c$ and $(\Gamma_p \gg \Omega_c)$. These conditions describe what is known as the 'dissipative regime', where spontaneous decay drives the rapid damping of the system's coherences, without these coherences, the elements of the OBE can be decoupled. This regime is true of almost all of this work due to the large difference in transition dipole moments between the Rydberg and intermediate state.

In this regime one can identify two distinct timescales. The first a fast evolution of the dynamics between the $|g\rangle$ and $|e\rangle$ states, and the second, the slow evolution of the $|e\rangle$ and $|r\rangle$ state dynamics. Under these conditions the populations are governed by the rate limiting coupling transition, with the fast probe transition able to follow adiabatically.

Also key to this approach is that the decay of the intermediate state is fast compared to the driving of the Rydberg state. Physically this means that in one lifetime of the

intermediate state the Rydberg population will not have evolved significantly, hence coherences within the system will damp on a much faster timescale than the excitation of population to the Rydberg state. If these conditions are met, then the coherences can be eliminated and the Rydberg state population reduced to a single rate equation.

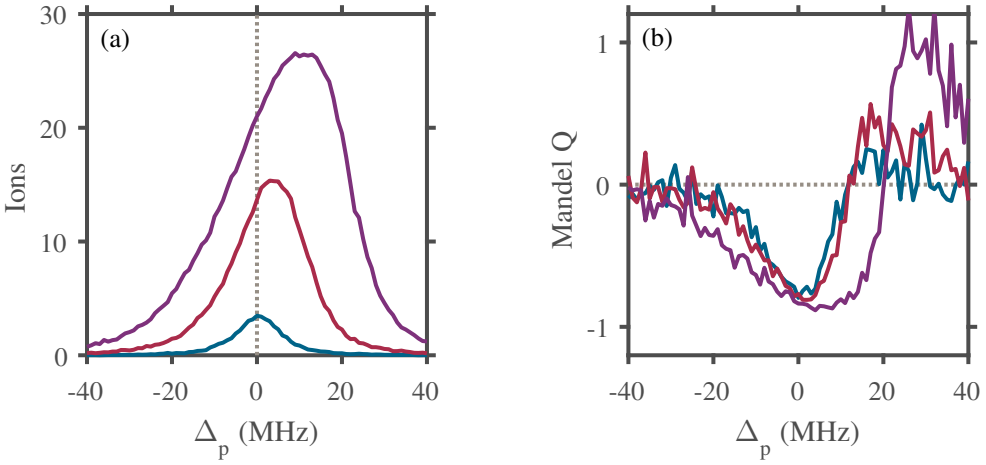

FIGURE 2.3: A set of sample simulations performed for experimental parameters achievable within the Durham strontium apparatus. (a) The predicted ion signal as a function of probe laser detuning Δ_p. (b) The predicted Mandel Q parameter of the excitation as a function of probe laser detuning Δ_p. The following ground state densities are plotted: $0.1 \times 10^{11}\,\mathrm{cm}^{-3}$ (blue lines), $1.0 \times 10^{11}\,\mathrm{cm}^{-3}$ (red lines), and $5.0 \times 10^{11}\,\mathrm{cm}^{-3}$ (purple lines).

Using this treatment the system can then be modelled using a standard classical Monte-Carlo method [32–35]. With the excitation dynamics computationally simplified, and the interactions included by summing the pair-wise interaction shift over all Rydberg atoms at the time of sampling, ensembles of many thousands of atoms can be modelled. The results of such a simulation are shown in Figure 2.3, and was performed in collaboration with Beatriz Olmos [36]. This simulation was carried out using experimentally realistic parameters and shows a number of interesting features that can be realised in the Durham apparatus.

The asymmetric line broadening seen in Figure 2.3(a) is associated with the anti-blockade mechanism [35]. This phenomenon occurs when the laser detuning matches the mean vdW shift. When this condition is met Rydberg excitation off-resonance is facilitated. On resonance the excitation is still suppressed and both effects can be seen in the Mandel Q parameter, Figure 2.3(b). The Mandel Q parameter, defined as

$$Q = \frac{\langle N^2 \rangle - \langle N \rangle^2}{\langle N \rangle} - 1, \tag{2.12}$$

provides a measure of the signal's deviation from Poissonian. A signal exhibiting the sub-Poissonian statistics associated with Blockade would have $-1 \leq Q < 0$. A signal exhibiting $Q > 0$ is associated with super-Poissonian statistics, as might arise from experimental noise. The Mandel Q parameter is a useful tool used in characterising interacting ensembles, and a key indicator that a sample has entered the strongly interacting regimes required in the works described in Chapter 1.

Summary

Both the rate equation and optical-Bloch simulations provide a glimpse into the types of physics that can be realised using the system and comprehensively treat the excitation dynamics and Rydberg-Rydberg interactions within the system. These techniques can and have been used to model the behaviour of the quantum systems outlined in Chapter 1 but one key assumption of both models is that the excitation laser Rabi frequency is constant; or stated another way, that the optical depth of the atom sample is negligible. We will see in Section 3.5, while examining ground state imaging, that this assumption does not hold for the samples under investigation. In Chapter 4 we will go on to explore how the experimental results differ from the predictions of the models as a result of these optical depth effects, and what steps can be taken to redress these issues.

Chapter 3

Experimental Methods

In the previous chapter, several theoretical models of Rydberg excitation were detailed and their relative regimes explored. This chapter will detail the experimental methods used to generate Rydberg ensembles and explore the regimes relevant to the discussed theoretical approaches.

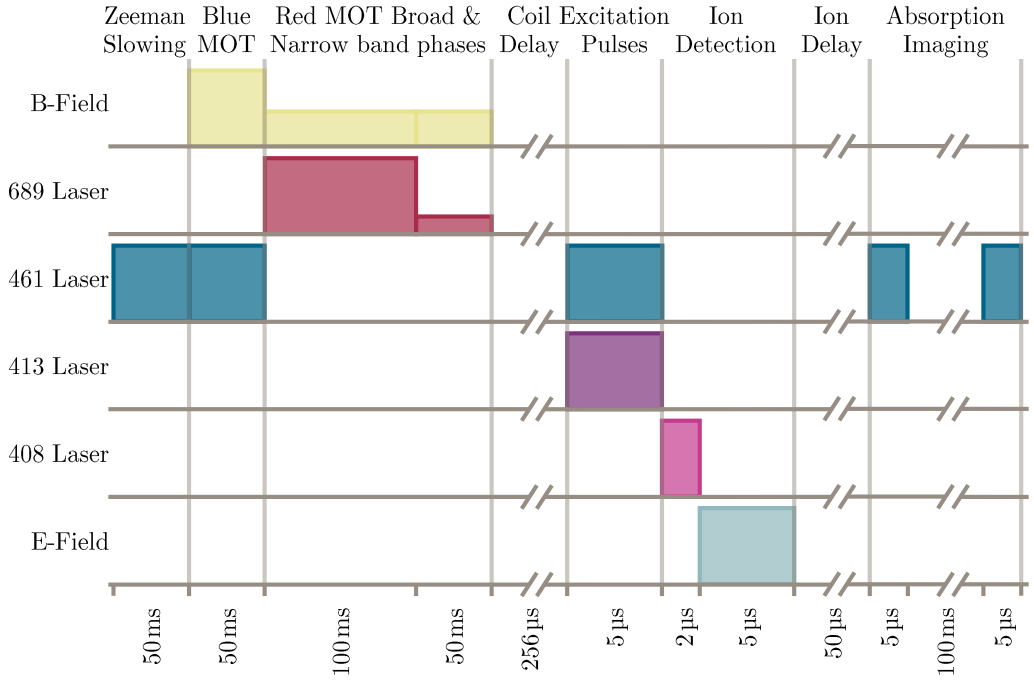

FIGURE 3.1: This timing diagram shows all key phases of a standard Rydberg excitation sequence as used in this work and where there are deviations from this sequence they will be explicitly mentioned. A change in the height of a timing block corresponds to a change in the relative magnitude of the laser intensity or field gradient in question.

Firstly ground state atoms are Zeeman slowed, cooled, and trapped in a magneto-optical trap (MOT) operating on the $5s^2\,{}^1S_0 \rightarrow 5s5p\,{}^1P_1$ transition (Section 3.3.1 and

Section 3.3.2). For further cooling the atoms are then transferred to a MOT operating on the $5s^2\,{}^1S_0 \rightarrow 5s5p\,{}^3P_1$ transition (Section 3.3.3), where they reach temperatures as low as $10\,\mu$K.

Once the sample is prepared the Rydberg atoms are created using the previously discussed three-level excitation scheme (Section 3.4), before being detected using a novel, autoionisation based detection technique (Section 3.4.3). Finally, with the Rydberg atoms detected, the sample is characterised using absorption imaging (Section 3.5).

3.1 Apparatus

Before exploring the experimental cycle, the experimental apparatus will be discussed with the following section outlining the vacuum chamber and laser systems used in the course of this thesis. The apparatus has been functioning for over seven years now and its build, characterisation, and evolution can be found in [19, 37, 38]. Where changes and improvements to the apparatus have been made during the course of this work these are commented upon explicitly.

3.1.1 Vacuum System

A computer aided design (CAD) overview of the whole vacuum system is presented in Figure 3.2 for reference. This system was developed during the thesis of J. Millen and further details can be found in [19]. A recent chamber upgrade replaced the viewports not used by MOT beams with ones containing uncoated, high optical quality, fused silica windows. This replacement increased the versatility of the chamber, as previously the broadband visible anti-reflection coating limited the use of short wavelength excitation lasers and long wavelength dipole traps. The replacement also served to improve the performance of the extra-vacuum focusing and imaging systems [9] as the previous windows were brazed and measured to have an optical flatness of 8λ while the new windows are bonded and are quoted to have a flatness of $\lambda/4$.

The chamber itself consists of two sections, the science chamber and the oven. The oven is formed from a resistively heated DN16 vacuum piece, sealed with nickel gaskets, containing 5g of 99.9% pure dendritic strontium pieces. With the addition of fibreglass

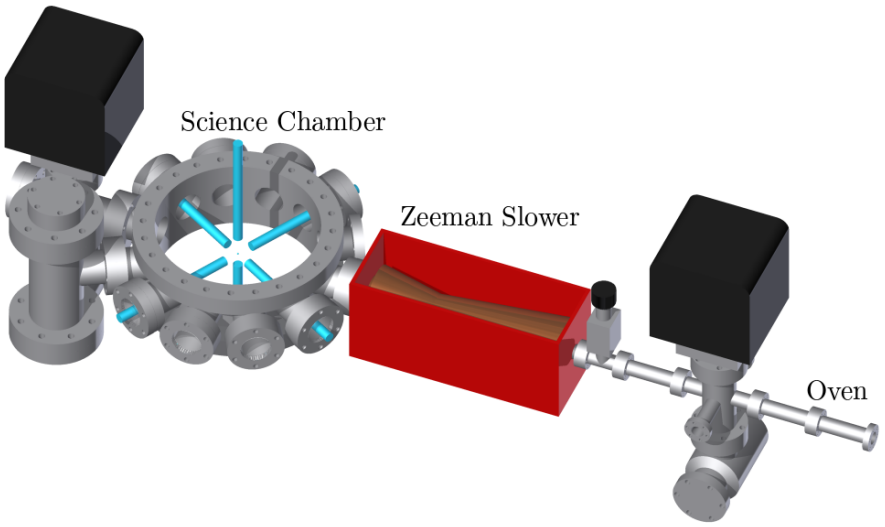

FIGURE 3.2: This is a CAD illustration of the vacuum system. Ion pumps can be seen in black at either end of the apparatus. The Zeeman slower can be seen surrounded by its mild steel yolk in red. MOT beams have been added to the science chamber for reference.

insulation, this set-up reaches the 700 K required to generate appreciable strontium vapour pressure. The output is collimated using 169 stainless steel capillaries of diameter 170 μm and 8 mm length. This design is based upon the work of [39]. It should be noted that strontium vapour is highly corrosive to copper, hence the use of nickel gaskets. Unfortunately, at high vapour pressures and long runtimes, nickel is also susceptible to strontium degradation. Oven failure has been observed in a similar system, after six years runtime, prior to the depletion of the strontium reservoir.

To aid refuelling and gasket replacement, the oven and science sections of the vacuum system are separated by a gate-value. This gate-value was utilised in a recent vacuum break and both sections have been shown to maintain vacuum independently. It should also be noted that the gate-value is manual and cannot be used to shutter the thermal beam in-sequence, as such the thermal beam is present at all times. The presence of this beam does not noticeably degrade the vacuum performance of the science chamber, with typical pressures of $\approx 3 \times 10^{-11}$ Torr observed under standard running conditions, as measured by the corresponding chamber ion pump.

The oven connects to the science chamber via a long DN16 connector that acts as a form of differential pumping. The Zeeman slower, discussed in a later section, is built around this connector. The science chamber itself contains a pair of in-vacuum copper coils, used to generate the field gradients required for the MOTs. These coils are not

actively cooled and their former serves as the mount for the split ring electrode pair described in Section 3.4.3.1. The oven and science chamber both have a 20 l/s ion pump, and the science chamber is further pumped by a 200 l/s NEG (non-evaporable getter) pump. These, and the two electrical feed through ports, can all be seen in Figure 3.2.

3.2 Laser Systems

To generate the wavelengths required to address the relevant strontium transitions, a mixture of home built and commercial diode laser systems are used. The following section outlines how each of the key laser wavelengths is generated, and subsequently stabilised, prior to being used in an experiment.

3.2.1 Primary Cooling Transition

The primary cooling transition in strontium is the $2\pi \times 30.2\,\text{MHz}$ wide $5s^2\,{}^1S_0 \rightarrow 5s5p\,{}^1P_1$ transition. The laser is a Toptica TA-SHG 110, which is a commercial frequency doubled system. This consists of a 922 nm master oscillator, amplified via a 2 W TA chip, and finally frequency doubled using a potassium niobiate crystal inside a bow-tie cavity. Typically this laser produces 250 mW of usable light in the second harmonic. This is then immediately coupled into a single-mode polarisation maintaining fibre from Schäfter Kirchhoff to reduce pointing fluctuations arising from thermal effects within the laser doubling cavity.

3.2.1.1 Modulation Transfer Spectroscopy

To stabilise this laser system, modulation transfer spectroscopy (MTS) is now used while previous works used sub-Doppler frequency modulation (SDFM) spectroscopy. MTS provides several advantages over the SDFM technique but the main gain is that MTS provides a Doppler background free locking signal. This Doppler free signal provides a more stable locking reference and greatly reduces the long term drifts that could negatively affect Rydberg excitation. To our knowledge this is the first time the technique has been demonstrated in strontium.

The MTS technique uses a strong, frequency modulated pump beam and an unmodulated probe beam. The sidebands of the pump beam are transferred to the probe beam via the non-linear susceptibility (χ_3) of the atomic medium. The non-linearity arises from the strong saturation of the pump beam and the process can be thought of as a four-wave mixing process [40]. Once transferred to the probe, the sidebands can then be detected on a high bandwidth photodiode and the resulting signal used for laser locking [41].

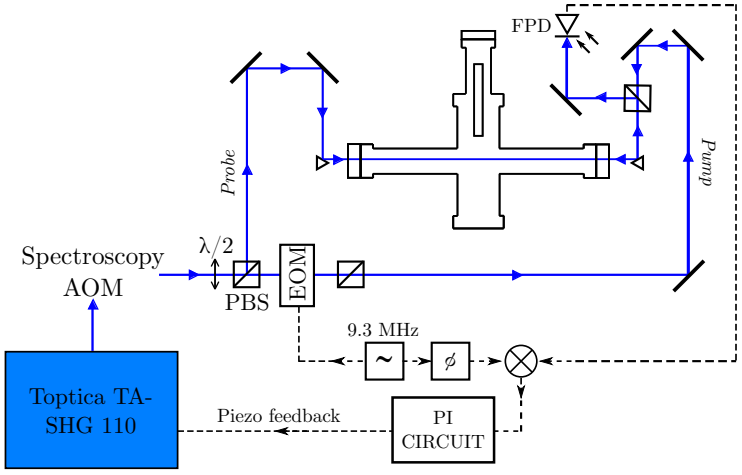

FIGURE 3.3: Schematic of the modulation transfer spectroscopy setup used to stabilise the 461 nm laser frequency. The beam paths (blue) and optics are shown along side the electronic signal path (dashed black) and the home made strontium beam cell.

Unlike many spectroscopic techniques, MTS produces a sub-Doppler error signal free of the Doppler background. This makes the signal more robust against changes in the signal amplitude arising from polarisation drifts, power fluctuations, variations in atomic flux, and changes in magnetic field. One caveat of the technique is that the signal is reduced if the transition is not closed. Fortunately, the leak out of the $5s5p\,{}^1P_1$ state is sufficiently slow for the technique to still be effective.

The set-up used to achieve this is shown in Figure 3.3. To modulate the pump beam an electro-optical modulator (EOM) is used (Photonics Technologies EOM-01-10-U), driven at 9.3 MHz by a tunable frequency generator (TTi TG120). As the modulation frequency is less than the HWHM of the transition being probed, the in-phase signal is proportional to the first derivative of the absorption, as can be seen in Figure 3.4. To obtain the DC signal, the newly acquired probe sidebands beat with the carrier on a home-made high bandwidth, fast photodiode (FPD). The subsequent demodulation is done on a level 7 double-balanced mixer (Mini Circuits ZLW-1-1). Due to the reactivity

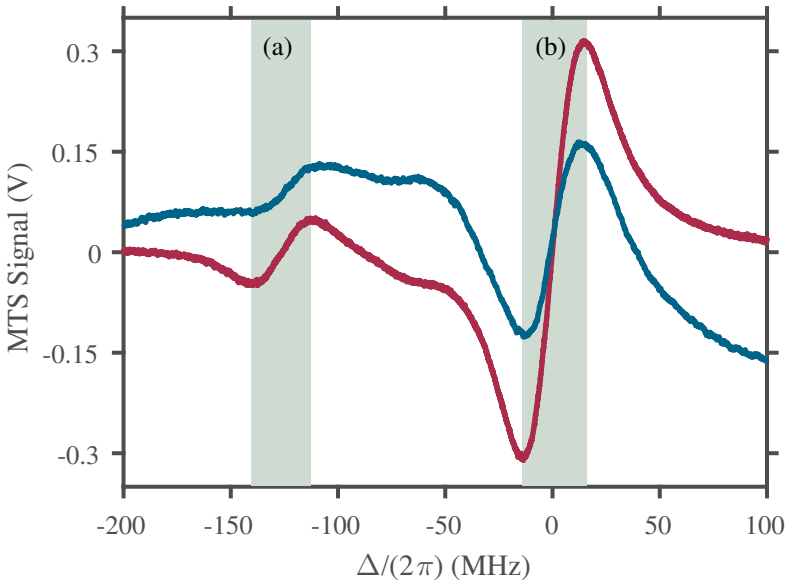

FIGURE 3.4: An example MTS signal (red line), post optimisation highlighting, the abundant bosonic isotopes. This is plotted alongside an optimised SDFM spectroscopy signal (blue line), reproduced from [37], for comparison. (a) Shaded region highlights the ^{86}Sr isotope. (b) Shaded region highlights the ^{88}Sr isotope feature used to lock to.

of strontium, a custom vapour cell utilising an Alvatec dispenser is used [42]. An example of the generated error signal is shown in Figure 3.4.

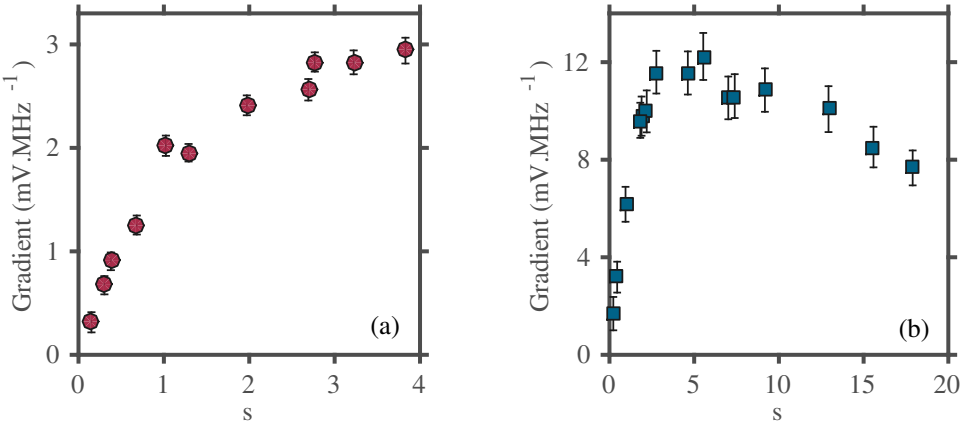

FIGURE 3.5: Optimising the MTS signal gradient. (a) Red circles show the variation of the ^{88}Sr MTS feature gradient as a function of the probe beam intensity. (b) Blue squares show the variation as a function of the pump beam intensity. Error bars represent the uncertainty in a fit to the error signal.

The gradient of the ^{88}Sr isotope signal as a function of the probe intensity and pump intensity is shown in Figure 3.5. The gradient as a function of the probe power shows a saturation type behaviour consistent with the saturation intensity ($40.2\,\mathrm{mW.cm^{-2}}$). The pump beam on the other hand shows the expected saturation behaviour but then

noticeably rolls over. This roll over is a result of the amplitude of the signal saturating and then power broadening reducing the gradient.

The gradient as a function of optical depth was also investigated and shown in Figure 3.6. The optical depth is set using the drive current for the strontium dispenser and finding the optimum conditions prolongs the lifetime of the vapour cell. Here it was found that an optical depth of 0.75 is optimum. Initially an increase in optical depth (b) increases the signal strength as there are a greater number of atoms undergoing the non-linear process. As the optical depth rises then so too does the attenuation of the probe and pump beams, resulting in a drop in signal as more and more of the probe light is scattered out of the beam.

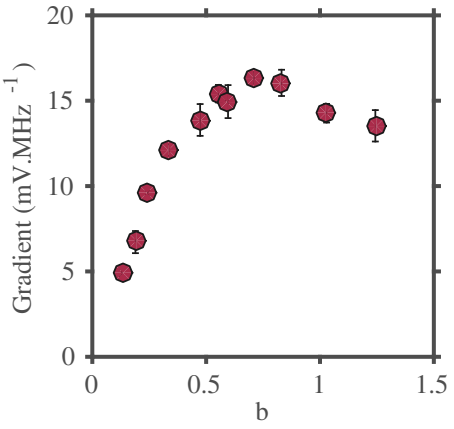

FIGURE 3.6: The variation of the ^{88}Sr MTS signal gradient as a function of the dispenser cell optical depth (b) is shown by the red circles. Error bars derived from uncertainty of the fit used to obtain the gradient.

With the described optimisations, MTS was implemented as a replacement to our previous SDFM locking scheme. This decision was taken primarily to reduce the frequency drifts associated with a technique that does not remove the Doppler background.

3.2.2 Rydberg Transition

Similar to the 461 nm laser system, 413 nm light for Rydberg excitation is produced using a Toptica TA-SHG 110 laser system. This system produces 60 mW at peak output but unlike the 461 nm system, this is not directly fibre coupled. Under normal conditions, 50 mW of this output is dedicated to laser stabilisation and 10 mW is available for laser excitation, which is fibre coupled for delivery to the experiment chamber. The laser is stabilised using an EIT locking technique[43]. This setup and the technique is

described in the thesis of G. Lochead [37], with the only significant changes being an increase in available laser power following a significant optimisation of the laser system, and that the laser is now locked on-resonance in the vapour cell.

3.2.3 Intercombination Line

For a detailed description of this system, including the short and long term locking solutions, refer to the thesis of D. Boddy [38]. Summarised, the 689 nm laser system is a home built master-slave arrangement. The master system is a simple, homebuilt extended cavity diode laser (ECDL) that is stabilised to eliminate long term drifts and short term frequency fluctuations. The short term fluctuations are suppressed by locking the ECDL to a homebuilt high-finesse optical reference cavity using a commercial fast feedback circuit (Vescent D2-125 Laser Servo). We also utilise a Vescent D2-105 Laser Controller to drive the master diode due to its superior noise characteristics. Using this combination of cavity and servo we estimate we obtain laser linewidths of the order of 10 kHz, although the exact determination of this linewidth is difficult without a second narrow laser system. This estimate comes from an analysis of the laser noise spectrum while locked and our knowledge of the locking cavity mode width.

Long-term frequency drifts are suppressed by stabilising the length of the optical reference cavity, using a pair of in-vacuum piezos [44]. This stabilisation is achieved through the saturated fluorescence spectroscopy locking of the narrowed laser to a Lamb dip feature in a thermal strontium beam. By beating the laser output against a GPS referenced Optical Frequency Comb, the stability of this laser has been measured to be $\approx 15\,\text{kHz}$ for measurement times between $10^{-3}\,\text{s}$ and $\gtrsim 10^{3}\,\text{s}$ [45].

To provide the necessary optical power, light from the stabilised master diode is used to injection lock a slave laser. Using a higher power diode in the slave laser system allows us to obtain 35 mW of stabilised and narrowed 689 nm laser power. This light is then modulated as required using an Acousto-Optical Modulator (AOM) before being delivered to the experiment via single-mode polarisation maintaining fibre.

3.2.4 Autoionisation Transition

The 408 nm laser system addresses the Rydberg autoionising transition and is a home-built ECDL using a wavelength selected diode (Sanyo DL-7146-101S). This system produces 50 mW of laser power, which is delivered to the experiment using a single-mode polarisation maintaining fibre. The only stabilisation requirement placed upon this laser system is that the laser does not mode hop; as such this system is normally left free-running. If more rigorous stabilisation is required, there is the capability to lock this laser to a HighFinesse WS7 wavemeter using a custom LabView code.

3.3 Sample Preparation

The start of any strontium Rydberg experiment involves preparing an initial atom sample. Here that involves taking atoms from the previously discussed hot atomic beam and Zeeman slowing them such that they can be captured in a MOT. Once this has happened the atoms are cooled in this first MOT and subsequently transferred to a second MOT operating on a narrow intercombination line. This three step process allows the production of samples with a large range of densities, temperatures, and geometries and is detailed in the following section.

3.3.1 Zeeman Slowing

The collimated atomic beam is first slowed using a compact, 'spin flip' Zeeman slower [46], operating on the $5s^2\,{}^1S_0 \rightarrow 5s5p\,{}^1P_1$ transition. This device was designed by Dr M.P.A Jones based upon work in [47] with specific details contained within [19]. Notable features include:

- a small table footprint arising from the large deceleration ($\approx 1.85 \times 10^6\,\mathrm{m.s^{-2}}$) afforded by the 5 ns lifetime of the $5s^2\,{}^1S_0 \rightarrow 5s5p\,{}^1P_1$ transition;
- a mild steel yoke which acts to enhance the slowing field and increase the field extinction outside the slower;
- a lack of water cooling.

The slowing beam itself is red detuned by $\approx 16\,\Gamma$ and is focused onto the atomic beam aperture, within the oven, to help compensate the divergence of the atoms. It is estimated that this focusing increases the captured flux by a factor of three [47].

Typically this set-up requires $\approx 40\,\text{mW}$ of 461 nm laser light, which compares favourably with other methods of capture [48, 49] where laser power is a constraint. It should be noted that atoms not slowed by the Zeeman slower are deposited upon the Zeeman beam entry window and strontium does chemically bond to glass. While this deposition has been observed, the rate is extremely slow, with the system still operating after 8 years of runtime. This window is replaced any time chamber maintenance is carried out that requires a vacuum break and is treated as disposable. Methods of avoiding this using heated sapphire windows and internal mirrors have been proposed [50] but have proved unnecessary.

3.3.2 1st Stage Magneto-optical Trap

The Zeeman slowed fraction of the thermal beam are then cooled and trapped within a standard six beam magneto-optical trap operating on the same $5s^2\,{}^1S_0 \rightarrow 5s5p\,{}^1P_1$ transition as the Zeeman slower. The 461 nm MOT light is derived from a single fibre-coupled beam. This beam is collimated to a $1/e^2$ waist of 5 mm before being split into the three separate MOT paths, each of which forms one of the retro-reflected trapping pairs. It should be noted that the vertical MOT beam is 3° off axis to allow the Rydberg excitation laser to also occupy this axis; no adverse effect on MOT performance is observed. The light is detuned from resonance by 1.2Γ and under normal conditions requires a total of $\approx 10\,\text{mW}$ of laser power. This MOT will be referred to as the 'blue MOT' in the text from this point onwards.

The quadrupole field used to create MOTs is generated by an in-vacuum pair of anti-Helmholtz coils, consisting of Kapton coated copper wire around a copper former [37]. The axial gradient used for the blue MOT was $25\,\text{G.cm}^{-1}$, which is limited primarily by the in-vacuum power dissipation of the coils themselves. Higher gradients can be achieved but at this level the coils can be operated continually without fear of overheating. The coils can also be rapidly switched during an experimental cycle, with typical rise times of around $400\,\mu\text{s}$.

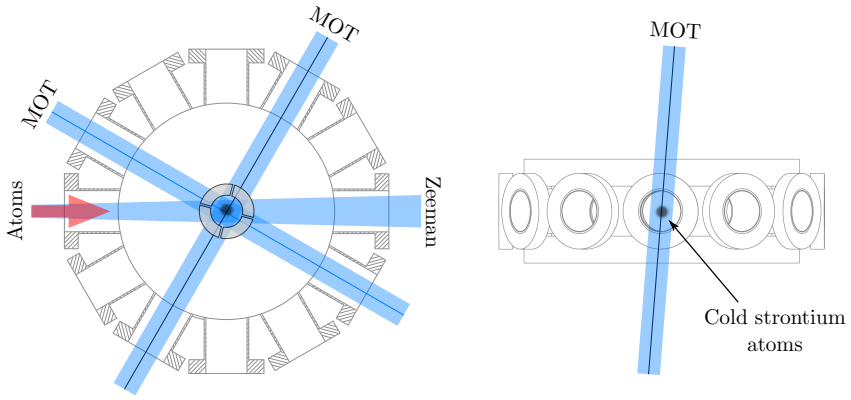

FIGURE 3.7: This diagram shows the chamber layout of the three retro-reflected blue MOT beam pairs in both the horizontal and vertical planes. The Zeeman slowing beam and hot atomic beams are also shown. During the first trapping stage all of these beams are engaged.

With the above parameters a typical atom number achieved in this sample is 2×10^7 atoms loaded within 50 ms and densities of around $2 \times 10^9\,\mathrm{cm}^{-3}$. This MOT operates in the density limited regime, where photon scattering processes within the MOT become dominant [51]. This represents an order of magnitude increase in atom number from [19], mainly arising from the implementation of fibre launched, larger MOT beams. The final performance of this trap is limited by the $5s^2\,{}^1S_0 \rightarrow 5s5p\,{}^1P_1$ transition not being completely closed (a branching ratio of $\approx 1:50,000$) [52] and the system can be improved with the addition of repump lasers. While two diode laser repumping lasers addressing the 679 nm and 707 nm transitions have been built and tested, repumping is not used in this work as the sample is already sufficiently large. For a detailed description and characterisation of this MOT system, refer to the work within [19, 37].

While the blue MOT stage provides a robust method of capturing atoms from the Zeeman slowed beam, the unique ground state prevents sub-Doppler cooling for the bosonic isotopes. Without these additional cooling mechanisms the trap can only cool to the Doppler temperature $T_D = 725\,\mu\mathrm{K}$, indeed even this is never reached. Due to other heating mechanisms, not accounted for in Doppler theory [53], this trap cools to around 5 mK. While this is hot compared to the primary cooling stage of, for instance, rubidium, it is sufficiently cold to allow the atoms to be transferred to a 2nd stage of cooling on the $5s^2\,{}^1S_0 \rightarrow 5s5p\,{}^3P_1$ intercombination line [54]. As the only atoms that can be captured by the 2nd stage MOT are those that have been first pre-cooled in the blue MOT, varying the loading time of this trapping stage is a robust and simple

way of varying the final sample atom number and density. This control is key for many subsequent experiments.

3.3.3 2nd Stage Magneto-optical Trap

The $5s^2\,{}^1S_0 \rightarrow 5s5p\,{}^3P_1$ transition in strontium has a natural linewidth of $2\pi \times 7.4\,\mathrm{kHz}$, nearly four orders of magnitude lower than that of strontium's primary cooling transition. This narrow linewidth provides a Doppler temperature of 179 nK, colder than the photon recoil temperature of 458 nK. It was for this incredibly low achievable temperature that the transition was originally investigated as a route to achieving Bose-Einstein condensation [54]. While it was found that light assisted collisions limit the phase-space density, it has since been shown that one can achieve an all-optical BEC using this transition through the engineering of a dark spot [50]. Crucial to all techniques utilising this transition is that the trapping laser is narrowed to a linewidth of the order of the natural linewidth [38]. This section gives an overview of the cooling dynamics and then discusses the experimental realisation of this technique.

3.3.3.1 Cooling Dynamics

The dynamics of cooling on narrow transitions can be split into three distinct regimes which are parametrised by the following: the power broadened linewidth Γ', the detuning δ, and the magnetic field gradient. In the first regime, the limit of large laser detuning and high saturation intensity, the spatially varying Zeeman shift induced by the MOT coils is key. This Zeeman shift acts to tune the MOT beams closer to resonance, hence for a red detuned MOT beam, there will be a certain magnetic field magnitude that is sufficient to bring the beam onto resonance, given by:

$$\delta = m_j g_j \mu_B B, \tag{3.1}$$

where $g_j = 1.5$ is the Landé g-factor for the $5s5p\,{}^3P_1$ state.

This condition leads to the formation of an ellipsoidal shell on which cooling can occur and where the thickness of this shell is governed by the power-broadened linewidth [54]. Atoms within this shell feel no force unless they are near the boundary; atoms outside the shell are lost from the system. Gravity is also key to the dynamics, as with no light

force to move the atoms to the centre of the trap, atoms instead 'pool' at the bottom of the shell as seen in Figure 3.8(c). Incidentally, the sensitivity of this process to the magnetic field environment also makes the sample position extremely dependent upon stray fields.

This second regime is characterised by a high saturation intensity and a detuning of the order of the power broadened linewidth. In this regime we regain the characteristics of a typical strong transition MOT, where the scattering force gives rise to the characteristic dispersion shape. Here the temperature of the ensemble is governed by the power broadened linewidth, through an effective Doppler temperature, and the geometry of the sample is set by the detuning.

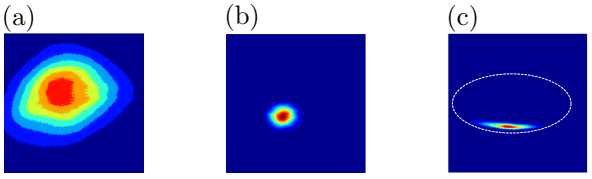

FIGURE 3.8: A set of false colour images at various states in the sample preparation process, the images all share the same field of view and atom density scale. The images (a) The blue MOT just prior to loading into the Broadband Red MOT. (b) The sample after the Broadband MOT phase. (c) A Narrowband MOT prepared using a detuning of 100 kHz and the superimposed boundary of the ellipsoidal cooling shell, as calculated from 3.1 (white dashed line).

The final regime is that where the saturation parameter tends to unity. In this regime the cooling dynamics are governed by photon recoils and the sample can achieve final temperatures of order half the recoil temperature[55]. This regime is not utilised in this work as the low temperatures confer little benefit and the transfer efficiency drops as the trap is weakened. For a full discussion of the trapping dynamics associated with cooling on intercombination lines refer to [38, 56]. The following section will outline the steps taken to experimentally realise cooling in this way.

3.3.3.2 Broadband and Narrowband Cooling

As discussed previously, the interaction between the laser detuning and Zeeman shift leads to the formation of a shell, on which cooling can occur. If we consider the $25\,\mathrm{G.cm^{-1}}$ axial field gradient that is persistent at the end of the blue MOT stage, we can calculate the impact of this ellipsoidal boundary. As any atoms outside of this boundary are not trapped, matching this to the Gaussian width of the sample at the

end of the blue MOT stage is necessary to achieve a viable transfer efficiency. The $1/e^2$ waist of the blue MOT is 500 μm and this necessitates a detuning, according to equation 3.1, of 2.65 MHz or 355Γ.

Additionally, the width of this shell for a narrowed trapping laser of $s = 1$ will be $\approx 2\,\mu$m. Atoms exiting the blue MOT have a velocity in the region of $1\,\mu\text{m}.\mu\text{s}^{-1}$ and will traverse this shell in a time that is much lower than their radiative lifetime. This limits their maximum number of scattering events to 1 and guarantees that they escape the trap before being cooled. To mitigate loss in this way there are two main approaches. The first is to increase the saturation intensity and thus the width of the shell. The second is to modulate the frequency of the trapping light, creating many concentric trapping shells and ensuring that an atom is always able to interact with trapping light throughout the sample volume. This second method is the one employed in this work and is referred to at the 'Broadband' phase.

Once atoms have been pre-cooled in this trap, the sidebands can be removed and the trap shifted to a single laser frequency. This 'Narrowband' phase allows the low temperatures previously discussed to be obtained and allows for greater compression of the sample, achieving higher density's as the trap detuning is lowered. As the geometry of the Narrowband MOT is strongly detuning dependent, this work can utilise both Broadband and Narrowband samples to explore a large range of sample geometries and densities.

3.3.3.3 Experimental Considerations

The implementation of these two further stages of cooling uses light derived from the slave laser previously discussed. This provides around 15 mW of power at the science chamber. For ease of alignment, the light used for Red MOT beams is spatially overlapped with the blue MOT trapping light on a dichronic mirror immediately after the fibre output. Figure 3.9 shows the beam positions in the science chamber. The Red MOT beams have a $1/e^2$ waist of 5 mm and are split into the three separate MOT paths on the same bi-chromatic polarisation optics as are used in the blue MOT beams. Again, to preserve optical access on the vertical axis, the MOT beams are 3° off axis. This weakens the trapping force against gravity but no adverse effects are seen on trap performance in either the Broadband or Narrowband phases.

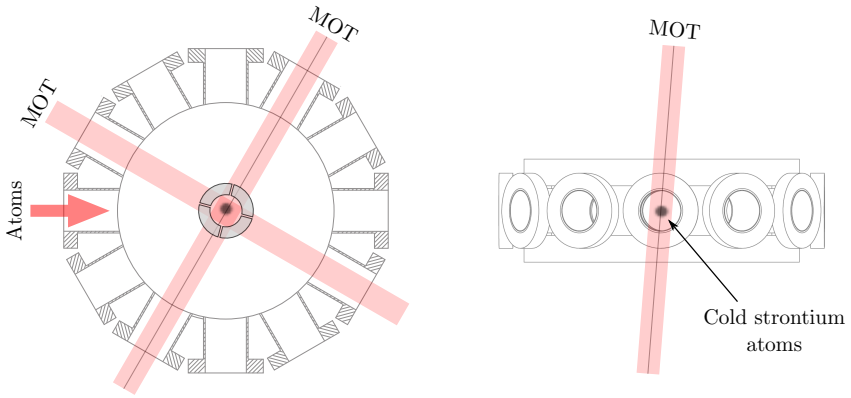

FIGURE 3.9: This diagram shows the chamber during the second MOT phase. Red trapping beams are overlapped with the blue trapping beams, which have been extinguished along with all other 461 nm light. Still present is hot atomic beam which cannot be shuttered.

In the Broadband phase the laser is artificially broadened through the addition of sidebands. This is experimentally realised by frequency modulating the RF drive field supplied to the AOM that shutters the trapping light. The modulation applied is a sine form with a modulation depth of 2 MHz and a modulation frequency of 50 kHz. This yields a fan ≈ 125 sidebands spanning 4 MHz, red detuned such that the nearest sideband is held 200 kHz from resonance. In this stage of cooling the full 15 mW of 689 nm laser power is used to power-broaden the sidebands as much as possible, each sideband having a saturation parameter of $\approx 10,000 I/I_{\text{sat}}$. During this phase the magnetic field gradient is lowered to 9 G.cm^{-1} and lasts for 100 ms. Transfer efficiencies of $> 50\%$ can be achieved from the blue MOT to the Broadband Red MOT.

To transfer the atoms into the Narrowband MOT, the modulation to the AOM is switched off and simultaneously the drive amplitude is reduced and the detuning changed. Some groups do this shift from Broadband to Narrowband phase gradually, one trap evolving into the next, which greatly improves the transfer efficiencies. In this work, that gradual change has not been implemented and instead there is a 'shock' transfer to the next phase limiting the transfer efficiency to around 20%. The power in this Narrowband phase is reduced to 1 mW, the detuning set to 100 kHz and the magnetic field gradient held at 9 G.cm^{-1}. This phase lasts for a further 50 ms. For a detailed description of the Red MOT setup and optimisation processes, refer to the work of D. Boddy [38].

3.3.4 MOT Summary Table

The following table summarises the properties of the three MOT stages. The range of achievable sample densities and waists are of particular note.

TABLE 3.1: A comparison of the various MOT stages. The width refers to the Gaussian $1/e^2$ radius of the atom sample in the gravity direction.

Property	Blue MOT	Broadband Red MOT	Narrowband Red MOT
Atom Number	2×10^7	1×10^7	2×10^6
Peak Density	$5 \times 10^9\,\mathrm{cm}^{-3}$	$1 \times 10^{11}\,\mathrm{cm}^{-3}$	$2 \times 10^{12}\,\mathrm{cm}^{-3}$
Width	$500\,\mu\mathrm{m}$	$200\,\mu\mathrm{m}$	$40\,\mu\mathrm{m}$
Optical Depth	1	12	14
Temperature	$5\,\mathrm{mK}$	$30\,\mu\mathrm{K}$	$10\,\mu\mathrm{K}$

3.4 Rydberg Excitation and Detection

Once the atom sample is prepared, the next step is to excite a fraction of the atoms to a Rydberg state and then detect them. The excitation is done via a two-photon ladder scheme. Detection of the subsequent excitations is achieved through first ionising them in a process known as autoionisation, and then using a shaped electric field to guide the ions onto a Micro Channel Plate (MCP). The following section expands on these processes.

3.4.1 Coherent Excitation

As discussed previously, excitation to Rydberg state is achieved through an on-resonance ladder type excitation, depicted in Figure 3.11. The beam layout for the excitation lasers is shown in Figure 3.10. Previous experiments required the excitation beams (probe and coupling) to be counter propagating in order to reduce the residual Doppler broadening. With the sample now three orders of magnitude colder there is no longer this constraint.

To simplify the experimental set-up the probe beam (λ_1) now also doubles as the absorption-imaging beam. This beam is fibre launched, has a Gaussian $1/e^2$ waist of $(2.5 \pm 0.1)\,\mathrm{mm}$, and is centred on the atom sample using steering mirrors and detected using the camera. This large beam waist does limit the accessible Rabi frequency to a

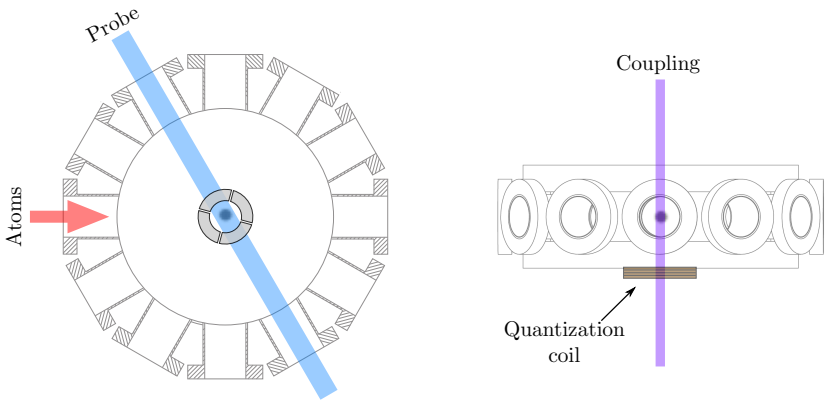

FIGURE 3.10: This diagram shows the chamber during a coherent Rydberg excitation. All trapping light is extinguished and the sample is excited using a two-photon ladder type excitation. The extra-vacuum quantisation coil is shown relative to the sample and the relative excitation beam sizes are highlighted.

maximum of $2\pi \times 15\,\text{MHz}$ but also ensures that the intensity is approximately uniform across the sample. The coupling beam (λ_2) is aligned along the vertical axis of the experiment and is also fibre launched with a waist of $(400 \pm 20)\,\mu\text{m}$. While there is the capability to focus this beam and only illuminate a subsection of the sample, in this work the whole sample is illuminated to reduce intensity averaging effects.

Typically these excitations last for $5\,\mu s$, although the exact time depends upon the rate of spontaneous ionisation, which will be discussed in the next section. During this excitation time the MOT coils are normally switched off and a second coil switched on to provide a quantisation axis. This separate quantisation coil sits outside the chamber, below the DN160 underside window, and can generate fields of up to 10 Gauss at the atoms. While only a single coil, the field is capable of being switched in $< 100\,\mu\text{s}$, allowing excitation to take place with minimal ballistic expansion of the cloud and with a defined quantisation axis. In this work the probe beam was horizontally polarised with respect to the quantisation axis and the coupling beam was circularly polarised to drive a σ_+ transition. While the horizontal polarisation of the probing beam does render half of the light unavailable for excitation, obtaining the required σ transition is not possible due to the beam geometry.

One additional control available during the excitation pulse is control over the electric field in the region of the sample. This is achieved through a pair of split ring electrodes mounted atop the MOT coil former. These electrodes allow complete control of the atom electric field environment and while not used for that purpose in this work, were successfully employed in [9, 37] to produce Stark maps.

3.4.2 Ionisation

Once the Rydberg sample has been formed, the next step is to ionise the ensemble prior to detecting the resulting ions on an MCP. While the chamber electrodes do allow for the field ionisation of the sample [19], which is the preferred ionisation method of most alkali Rydberg groups [57], our experiments utilise an autoionisation technique. This technique is possible due to strontium's two valence electrons allowing for a doubly excited state with more energy than the first ionisation threshold, see Figure 3.11.

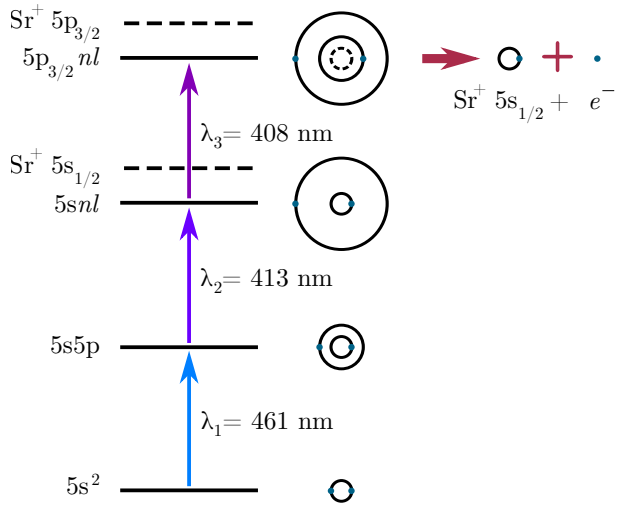

FIGURE 3.11: Depiction of the specific isolated core electron level scheme used in the autoionisation method, an extension of the ladder scheme shown in Chapter 2.

Following the excitation of the first electron to a Rydberg state, the second electron can be optically excited in a manner similar to that of a singly ionised strontium atom. This process of exciting the core electron is called 'isolated core excitation' (ICE) [58]. The transitions in the core are similar to D1 and D2 lines in the bare Sr^+ ion, but the presence of the Rydberg electron perturbs the line position and transition widths. This strength of the perturbation is related to the overlap of the two electron wave-functions and, as a result, becomes less significant as the Rydberg state increases in either n or l [2]. For low angular momentum states ($l < 3$) the overlap is sufficiently large that the atom quickly ionises ($\approx 10\,\text{ps}$) with very high probability. This process of rapid ionisation is known as 'autoionisation' and can be used to obtain temporal, spatial, and atomic state information from an ensemble [9, 59].

The spatial detection component of this technique comes from tightly focusing the autoionisation beam and placing it on a motorised stage, in doing so one can build up the Rydberg distribution as a function of position over repeated experiments. The

autoionisation beam is focused to a waist of $(6 \pm 1)\,\mu$m onto the sample. This beam is then pulsed on for $2\,\mu$s to ionise the atoms within the illuminated volume. At the $5s48s\,{}^1S_1$ state the autoionising resonance is $> 20\,$GHz wide and this ionisation has been shown to be unaffected by day-to-day frequency fluctuations in the 408 nm laser frequency. Recent work [60] has demonstrated that by exciting the ensemble to a high angular momentum state ($l > 9$), it is possible to directly image Rydberg atoms via non-destructive, resonant scattering on the 408 nm line. This is possible as the wave-function overlap between the Rydberg state and excited core election is sufficiently low to suppress the autoionisation effect for high angular momentum Rydberg states.

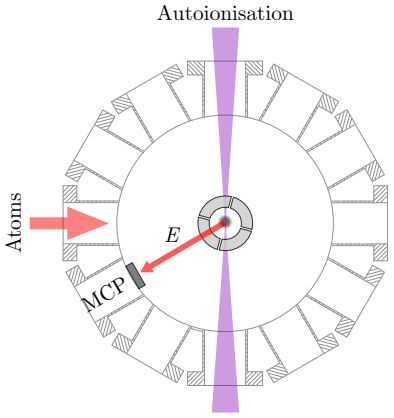

FIGURE 3.12: This diagram shows the location of the MCP within the chamber and the focused autoionisation beam. The alignment of the split-ring electrodes is crucial to ensuring that the produced ions are propelled successfully towards the MCP. The direction of the guiding electric field is shown.

In competition with this autoionisation process is the spontaneous ionisation of the sample. As the Rydberg atoms are close in energy to the ionisation threshold, they only require a small perturbation to fully ionise. We refer to this uncontrolled ionisation of the sample due to external factors as 'spontaneous ionisation'. This can arise for a number of reasons and include but are not limited to: Penning ionisation as attractively interacting Rydberg atoms accelerate towards each other [61]; direct ionisation or re-distribution via blackbody radiation [62]; or collisions between Rydberg atoms and hot atoms from the thermal beam [63, 64]. If the spontaneous ionisation rate is sufficiently high then the sample can undergo avalanche ionisation and form an ultracold plasma [19, 59, 65–67]. Careful tuning of the excitation time and driving Rabi frequencies can ensure that autoionisation remains the dominant mechanism and Figure 3.13 shows their relative contributions to an example signal.

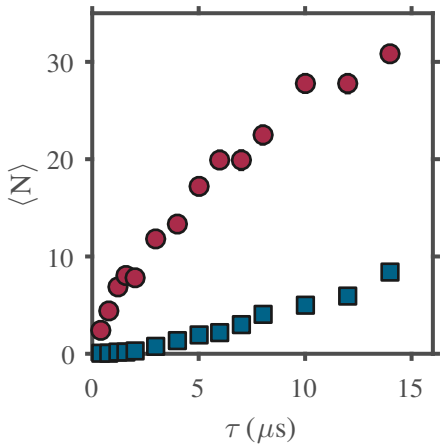

FIGURE 3.13: The number of ion counts as a function of excitation time for the $5s48s\ ^1S_0$ state under standard experimental conditions. Red circles represent the total ion count following an autoionisation pulse. Blue squares represent the ion signal without an autoionisation pulse, assumed to be the spontaneous background signal.

Once the sample has been ionised the electric field plates are then used to guide the atoms towards the MCP.

3.4.3 Detection

The electrode rings are aligned such that one pair can be used to shunt the ions towards the detector. The MCP front plate is held at −100 V and the back plate is held at 2 kV, behind which is the anode which is grounded through the detection circuitry. All of this is shielded by a charged grid which helps to reduce the stray field generated by the MCP. This grid is held at −20 V to provide additional guiding for the ions. It should also be mentioned that this grid is only 40% transmissive, a major contributing factor to the overall detection efficiency of the system.

On arrival at the MCP each ion generates a 5 ns wide voltage spike, demonstrated in Figure 3.14. To record these events a high-bandwidth oscilloscope (*Tektronix DPO 4054*) is used. Events detected on the instrument are identified using a threshold approach and the total number of counts is read out at the end of the experimental sequence. As each ion also has an associated ring, where an impedance mismatch within the MCP setup leads to a second, reflected signal, the detection threshold has to be set to filter these second counts. The ion signal amplitude is not uniform and so some counts will be missed by this thresholding method. The ions arrive in a packet spread over approximately 2 μs approximately 27 μs post ionisation and so one has to

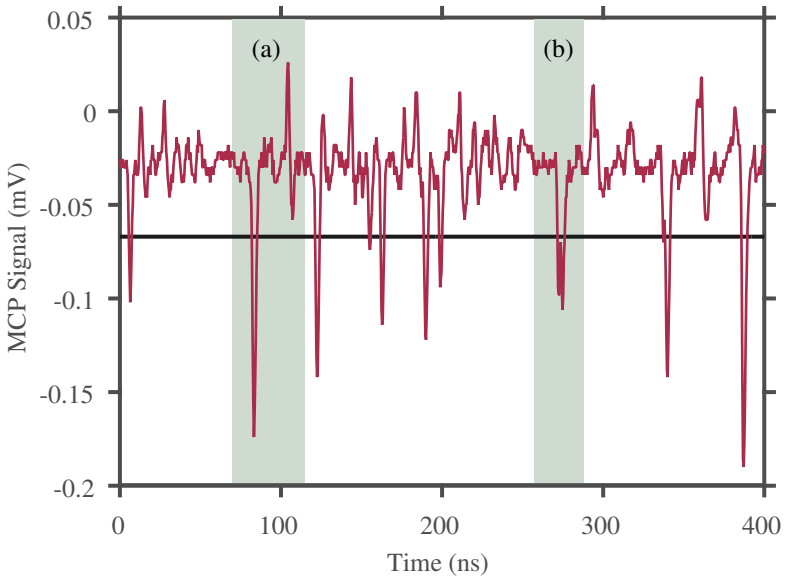

FIGURE 3.14: MCP signal voltage as a function of time is given by the red trace. The black line shows the voltage threshold level at which an ion event is recorded. (a) Shaded region highlights an individual ion event followed by the associated ring event. (b) Shaded region highlights a double arrival event where only a single ion is recorded.

be careful to avoid saturating the detector, which happens at around 60 counts. This saturation is well described by a simple computer simulation where finite width events are drawn from a random distribution and checked for collisions. To test the linearity the simulation was run for a range of simulated ion events and the simulated ion signal thresholded in the same way as the experimental data, see Figure 3.15. The simulation confirmed the 60 count saturation threshold that was established experimentally.

One has to be careful when analysing the ion counting statistics. Should the threshold be incorrectly set, missed counts will cause the counting distribution to tend towards Poissonian. Conversely, a saturating detector will cause the distribution to tend towards sub-Poissonian. To eliminate these effects the threshold was optimised to minimise both missed and double counts. To keep the number of ion events from saturating it is possible to reduce the pushing field that delivers the ions to the MCP. This has the double effect of increasing the ion arrival time spread and also reducing the number of ions reaching the detector but also reduces the minimum measurable sub-Poissonian Mandel-Q parameter.

As well as saturation effects, the alignment of the ion beam with the MCP was found to be an issue and a more sophisticated guiding field than in previous work proved necessary. This suggests that the internal electric field environment of the science

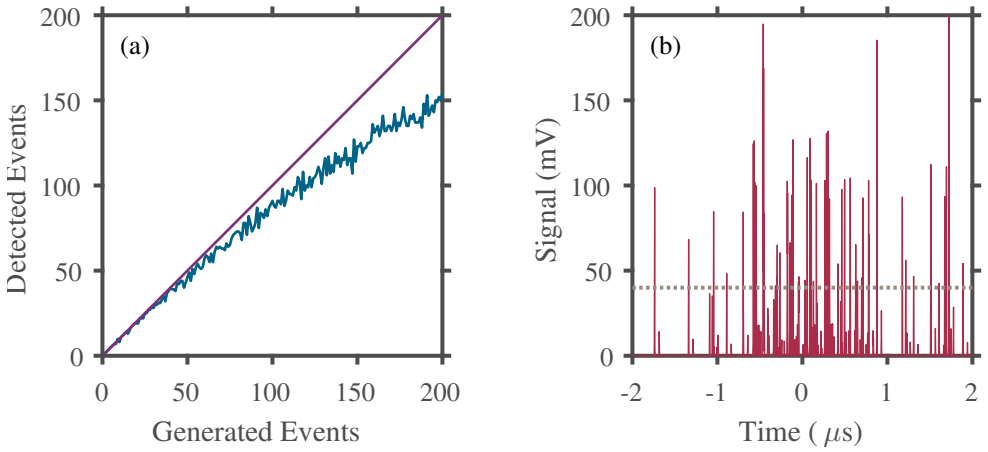

FIGURE 3.15: Shown is the output of a simple detector saturation model that reproduces the saturation behaviour of the MCP observed within the experiment. (a) The number of events generated plotted against the number detected using a threshold method (blue line) demonstrates the departure from detector linearity (purple line) with increasing numbers of ions. (b) A simulated ion trace (red line) showing the normal distribution of arrival time and signal height, along the threshold voltage level used in ion detection (grey dashed line).

chamber appeared to have substantively changed as previously it was found that the vast majority of generated ions were detected at the MCP [37].

3.4.3.1 Ion Guiding

During the course of this work it became necessary to open the vacuum chamber. This operation, while vital, led to a modification of the chamber internal electric field environment which had serious repercussions for the experimental detection efficiency.

The original opening of the chamber was to install the optically flat ($\frac{\lambda}{8}$) uncoated fused silica viewports described in the previous section. Upon baking the chamber following this the epoxy resin fixing the split ring electrodes to the MOT coil former failed, likely as a result of improper curing and heat cycling of materials with differing thermal expansion coefficients, see figure Figure 3.16. This damage necessitated the reopening of the chamber and the former assembly stripping down and rebuilding. While rebuilding, several electrical shorts in the electrodes and MOT coils, noted in [19, 37] were repaired.

Following these repairs it was noted that the recorded ion signals were significantly weaker than previously observed. Diagnostics on the MCP itself and on the Rydberg generation process were carried out. It was confirmed that Rydberg atoms were indeed

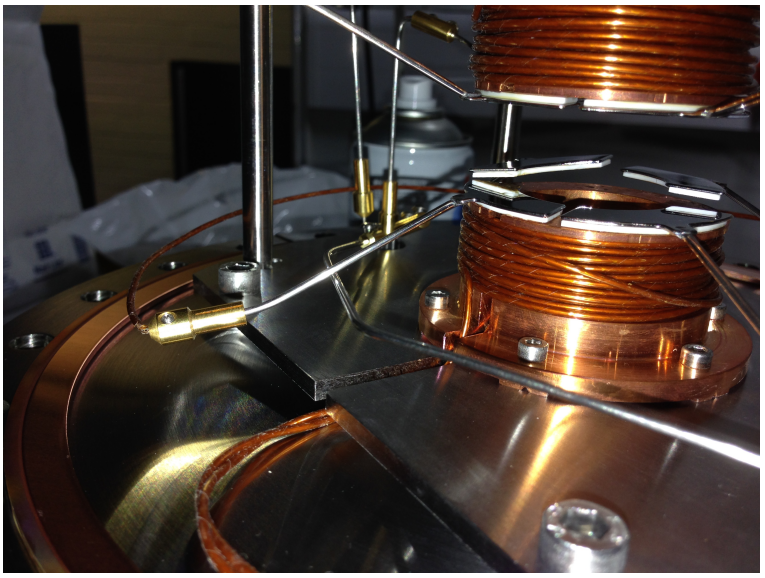

FIGURE 3.16: This is an image of the chamber MOT coil assembly and split ring electrode array. The detached electrodes can be clearly seen.

still being created and that the electrical characteristics of the MCP had not changed, subsequently it was concluded that the created ions were therefore not reaching the MCP. To test this hypothesis the split ring electrodes were used to apply shaped guiding pulses in the hope of recovering the ion signal. The results of these experiments are shown in Figure 3.17.

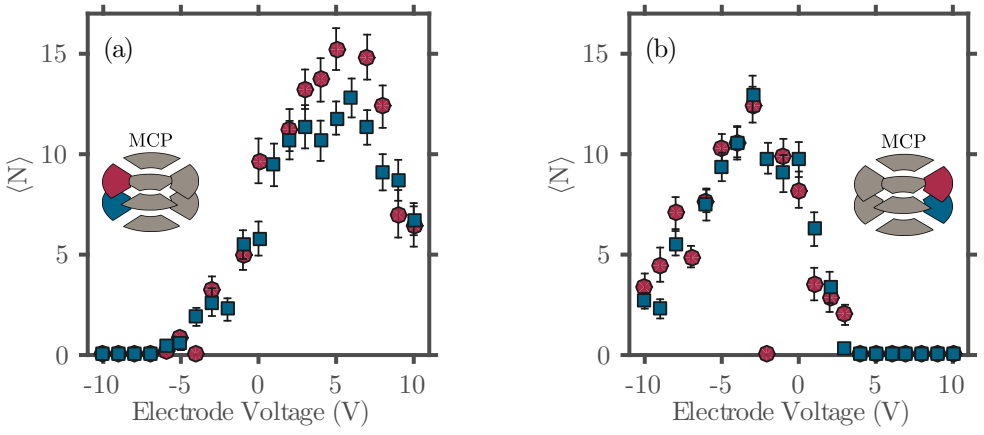

FIGURE 3.17: The total ion count as a function of the various lateral electrode voltages. (a) The left-hand electrode pair, scanned individually, where the colours correspond to the electrodes indicated in electrode schematic. (b) The right-hand electrode pair. All uncertainties correspond to the standard error on 100 repeat measurements.

Scanning the electrodes in the plane of the MCP maximized the ion signal when a potential of 5 V was applied to the left-hand electrodes. A slightly lower potential of −4 V was required for the right-hand electrodes. This shows two things: firstly that the ion beam is indeed misaligned with the MCP, and secondly that the ions have a

significant spread once they reach the MCP. While the reasons behind this misalignment are unclear, as care was taken to align the axis of the pushing electrode pair with the axis of the MCP, it is likely the result of a component becoming charged during the course of the chamber repair.

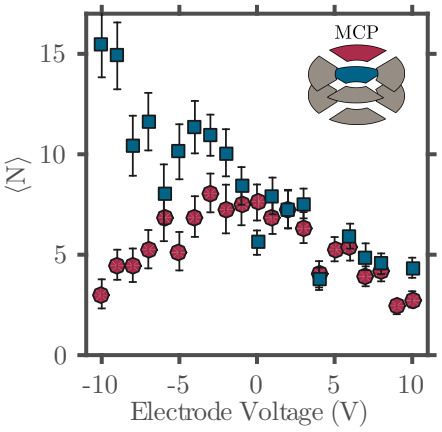

FIGURE 3.18: The total ion count as a function of the forward electrode pair voltages, scanned individually. The colours correspond to the electrodes indicated in electrode schematic and all uncertainties correspond to the standard error on 100 repeat measurements.

Once the misalignment of the ion beam in the horizontal plane was corrected, an investigation of the alignment in the vertical direction was also performed and the results of which are shown in Figure 3.18. These tests again showed a misalignment. The parabolic shape of the upper electrode scan and the linear increase of the lower electrode indicate the beam is aligned too high. The shape of the upper electrode scan when $V < 0\,\mathrm{V}$ is caused by ions being attracted upwards and worsening the misalignment. The shape at $V > 0\,\mathrm{V}$ is caused by the now positive electrode repelling the ion beam. The shape of the curve for the lower electrode follows similar reasoning. It is possible that further gains could be made by exploring voltages $> -10\,\mathrm{V}$ but the pulse generator used could not do this. Additionally, as described earlier, problems with detector saturation were observed and confident that the beam was now aligned with the detector, further optimisation was not carried out.

In addition to the signal being weaker than previously recorded, the signal also gained a non-linear density dependence. At low MOT densities the ion signal was completely suppressed, whereas at higher densities the signal would increase and then saturate. Prior to the discovery of the misalignment, it was thought that this 'turn on' behaviour could be the result of 'Rydberg facilitated growth' [33], a signature of the anti-blockade. This occurs when the Rydberg excitation lasers are blue detuned from the two photon

resonance and an increasing interaction shift with density leads to the atoms being tuned back onto resonance. Extensive studies of the excitation spectra led to this hypothesis being rejected as the cause.

Instead, it is now thought that what is being observed is the density dependent Coulomb expansion of the generated ions. In low density samples the ions created by autoionisation are well separated and feel neighbouring ions only weakly. As the density increases and the inter-ion separation decreases however Coulombic repulsion becomes progressively more important and the ion cloud undergoes a 'Coulomb explosion'. The physically larger ion cloud that results from the Coulomb expansion now overlaps spatially with the MCP when projected onto the detector and a signal is detected. This Coulomb explosion could form the basis of a further study but is out of the scope of this work.

In summary, while a change in the internal electric field configuration of the science chamber has been observed, this has been compensated for by shaping the ion guiding electric field. With this compensation in place we obtain comparable detection efficiencies to those previously measured, for signals of up to 60 ions, while maintaining full counting statistics.

3.5 Ground State Imaging

Previously published work from the Durham group [59] has involved probing the ground state distribution of the sample using an off-resonance fluorescence imaging technique. This utilises the same beams as the first stage $5s^2\,{}^1S_0 \rightarrow 5s5p\,{}^1P_1$ MOT, which are detuned by -1.5Γ, to cause the ground state atoms to fluoresce. This fluorescence signal is then collected by a 1:1 telescope and imaged onto a PixelFly QE CCD. While this camera has a poor dark count and noise specification, it has a high quantum efficiency for radiation at 461 nm. The spatially resolved images produced by this CCD can then be used to calculate the population, location, and distribution of the sample.

To extract the ground state population one can assume the sample is a collection of N two-level scatterers. Using the equation for the scattering rate of a two-level atom,

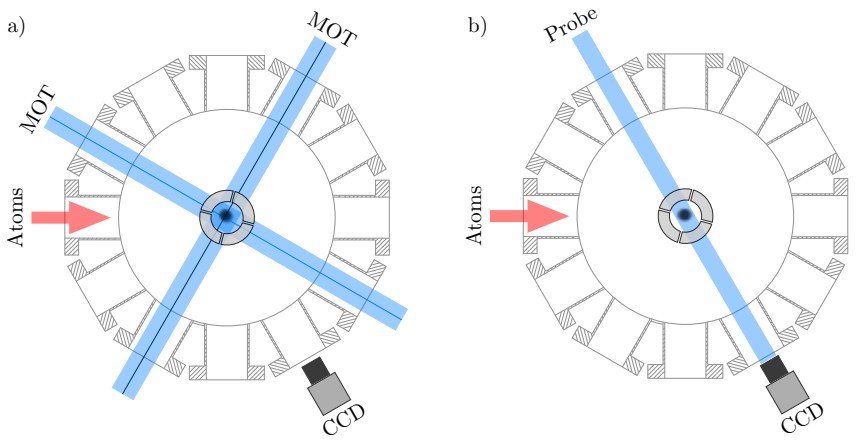

FIGURE 3.19: These schematic diagrams show the beam geometries and camera placements used in fluorescence imaging (a) and in absorption imaging (b).

$$R_{sc} = \frac{\Gamma}{2}\left(\frac{s}{1+s+4(\Delta/\Gamma)^2}\right), \tag{3.2}$$

where Γ is the natural linewidth of the $5s^2\,{}^1S_0 \rightarrow 5s5p\,{}^1P_1$ transition and s is the saturation parameter given by I/I_{sat}, one can calculate the number of photons each atom should scatter and use the total detected photons to infer N. For dilute samples this technique is robust as long as one accurately knows the detuning and power of the probing beams.

The imaging time required to accumulate sufficient signal is dependent on the scattering rate and N but generally this is in the region of a few hundred microseconds. For low atom numbers this can lead to a significant blurring of the image as the cloud is heated by the MOT beams while a sufficiently high SNR is built up. To increase the speed of the imaging process one can instead use absorption imaging.

Unlike fluorescence imaging, where one detects the photons scattered out of the probing beams, absorption imaging measures the probing beam directly, removing a source of uncertainty from the measurement and speeding up the process. To derive an atom number using this technique one considers the transmission of light through the sample to be described by Beers Law, where the exponent is the optical depth and can be written in terms of the column density, $n(x, y)$, and the absorption cross section, σ, to give:

$$I = I_0 e^{-n(x,y)\sigma} \tag{3.3}$$

The absorption cross section of a two-level atom in a weak, resonant probing beam is given by:

$$\sigma_0 = \frac{3\lambda^2}{2\pi}. \tag{3.4}$$

If the probing beam has a non negligible detuning or intensity then the cross section becomes:

$$\sigma = \frac{\sigma_0}{1 + s + 4(\Delta/\Gamma)^2}. \tag{3.5}$$

To extract the sample population using this technique one must measure the optical depth of the sample to extract the column density. When considering dense samples however, care must be taken when implementing both fluorescence imaging and absorption imaging. If the mean free path of a scattered photon is less than the width of the sample then the simple scattering picture used to extract the population within fluorescence imaging breaks down. Similarly, if the optical depth of the sample becomes too great while absorption imaging, then the SNR of the transmitted probe field becomes unfavourable. In the case of the dense red MOT discussed previously, these optical depths can reach as high as 30 and the photon mean free path can drop to micrometers, far below the sample size.

In principle, all one has to do to apply these techniques to dense samples is to reduce the absorption cross-section of the scatterers. In fluorescence imaging two handles are available to achieve this goal, namely, the detuning and the saturation parameter. Unfortunately the strontium $5s^2\,{}^1S_0 \rightarrow 5s5p\,{}^1P_1$ transition proves unfavourable in this regard. The large natural linewidth of $2\pi \times 30.2\,\mathrm{MHz}$ means achieving an appreciable detuning is technically challenging using an acousto-optical modulator. Additionally, to reduce the optical depth by increasing the probing intensity is also difficult due to the transitions high saturation intensity of $40.2\,\mathrm{mW.cm^{-2}}$ and the difficulty in generating blue laser light. This unfavourable saturation intensity prohibits the use of the high intensity technique described in [68].

The $5s^2\,{}^1S_0 \rightarrow 5s5p\,{}^3P_1$ transition in strontium could in principle be ideal for imaging dense clouds due its linewidth and saturation intensity being 5 orders of magnitude

lower than that of the $5s^2\,{}^1S_0 \rightarrow 5s5p\,{}^1P_1$ transition. Unfortunately here the weak scattering rate makes fluorescence imaging challenging without an amplified CCD and the low saturation intensity necessitates the use of a weak probing beam, which again would prove challenging to detect with the current camera. Taking all of the above into consideration, the ground state imaging technique used throughout this thesis is absorption imaging, where the saturation of the camera is accounted for through fitting the resulting image.

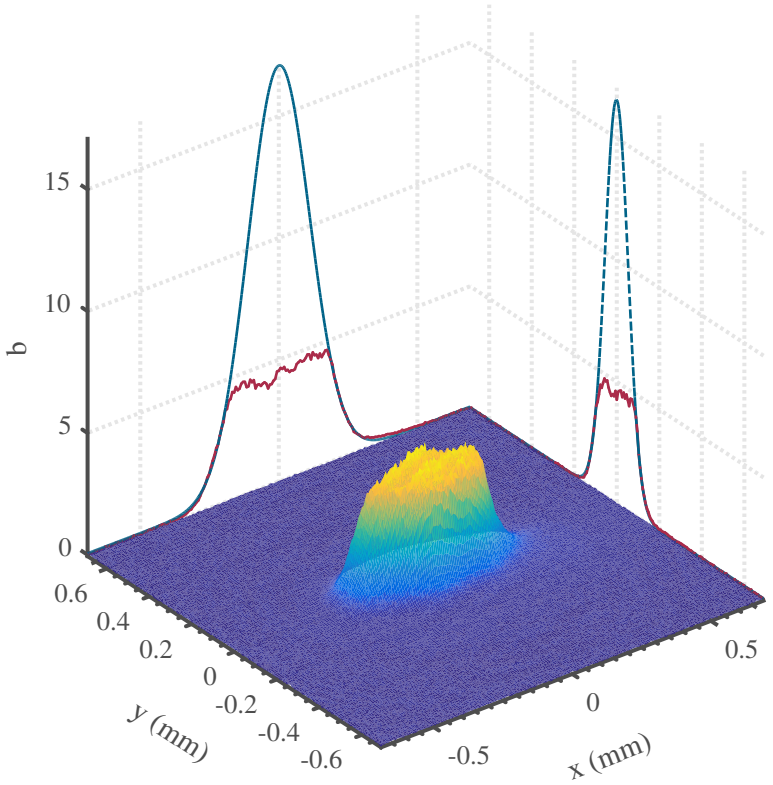

FIGURE 3.20: A false colour image of an atom cloud captured by the PixelFly CCD. The optical depth of the could (b) is shown on the z-axis of the plot. The red solid lines show cross sections taken through the centre of the distribution while the blue dashed lines show the Gaussian fits to the wings of these cross sections.

3.5.1 Ground State Fitting

If one takes a standard absorption image of an optically thick cloud then the resulting image looks like that shown in Figure 3.20, where the characteristic flat top is seen. This flat top is given by the noise floor of the camera, the lower the camera dark noise, the higher the optical depth at which this profile would flatten off. For our setup and camera the maximum directly measurable optical depth is 4, as can be seen in the

figure. While one cannot extract the atom number directly from this image, there is still significant information contained within the wings of the cloud, where the SNR is still favourable. By making a series of assumptions it is possible to estimate the original profile and therefore the true atom number.

To reconstruct the image, it must first be assumed that the density profile of the cloud is Gaussian, previous imaging of less dense clouds confirms this to be a good approximation. By assuming a Gaussian geometry one can extract the wings of cloud and use these to constrain a fit.

The second assumption is that the atom cloud is radially symmetric. This allows the fitting problem to be reduced from fitting a 2D Gaussian to fitting two 1D Gaussians. To obtain these fits the centre of the cloud is located and then a 1D slice is taken along the x and y axis of the image; these slices are also shown on Figure 3.20. These slices are thresholded, such that all information corresponding to the flat top is removed. The remaining wings are then what is fitted, yielding two Gaussian waists for the cloud, a centre position, and the peak optical depth as predicted by the fits. These values can be used to reconstruct the 2D image, and the integrated column density recovered to obtain an atom number.

To obtain a density, one must know all three cloud waists but as we only have a single camera on the experiment, there is always one waist that is unseen. To account for the unseen waist of the cloud a third assumption is required; that the sample is radially symmetric around the MOT coil axis. This assumption allows the fitted widths to be used to obtain a MOT volume by setting the unseen waist equal to the one already measured, allowing a volume and thus a density to be obtained. The error in this method can be estimated using the fit uncertainties and suggests atom number uncertainties of $\approx 10\%$ for higher optical depth ($b > 10$) samples.

By allowing the cloud to undergo ballistic expansion one can lower the density sufficiently to measure the ground state population using standard absorption imaging techniques and test the validity of the fitting approach. The atom numbers derived from this expansion can then be compared to the atom numbers derived from the fitting method outlined above. This comparison is shown in Figure 3.21 and supports the techniques validity for optically thick clouds, extending our imaging capability by a further two orders of magnitude in sample density.

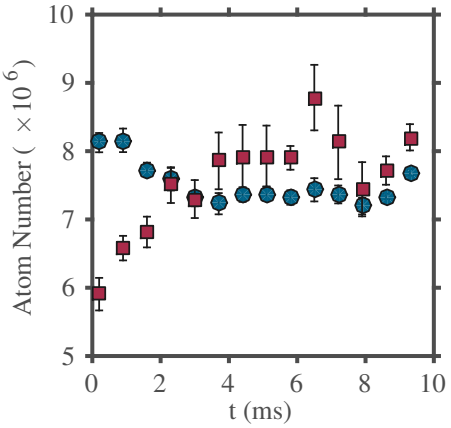

FIGURE 3.21: The variation of measured atom number as a function of ballistic expansion wait time for the standard absorption imaging method of integrating counts (red squares) and for the fitting method (blue circles). Data was taken in a Broadband MOT with a peak optical depth of $b = 10$.

Figure 3.21 also clearly demonstrates that, without the fitting correction, the standard technique underestimates the ground state population. The true population is only recovered after 4 ms of free expansion and this atom number inaccuracy would become increasingly acute with increasing optical depth. Inaccuracies in the densities calculated would be further enhanced by the poor Gaussian waist resulting from the fit to a flat topped profile.

Summary

This chapter has outlined the key experimental techniques employed within this thesis and specific attention has been paid to areas of the apparatus that have been developed during this work. Those being the transition to MTS locking of the 461 nm laser, the experimental chamber window replacement, and the correction of the electron guiding electrodes. The creation of these denser atom samples has required the implementation of a new imaging technique due to the optical depth effects that will be further explored in the following chapter.

Chapter 4

Rydberg Excitation in an Optically Thick Cloud

In the previous chapter the apparatus and techniques used to create an ultracold gas of strontium atoms, excite that gas to Rydberg states, and then detect those excited atoms were detailed. It was also noted that improper alignment of the electric fields used in the detection of these excitations could result in non-linear detector behaviour. Upon correcting this alignment, several previously undetected effects became manifest.

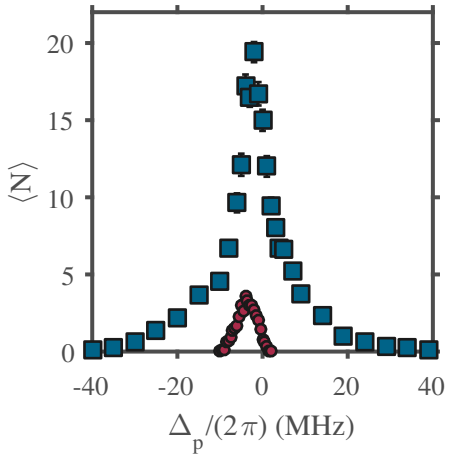

FIGURE 4.1: The average ion signal $\langle N \rangle$ as a function of the probe laser detuning Δ_p in the case where the guiding electrodes have not been optimised (red circles). The same signal taken with optimised guiding electrodes is also plotted (blue squares). All data points are an average of 100 experimental runs.

This step change in detector behaviour is illustrated in Figure 4.1. This shows that ion signals below a certain threshold were completely suppressed, in the miss-aligned system, drastically altering the shape and magnitude of the ion signal. It can be

seen that where the unoptimised signal is both symmetric and Gaussian, the signal taken with optimised electrodes exhibits a completely different form, looking both more asymmetric and Lorentzian.

This chapter constitutes an investigation into the $5s48s\,^1S_0$ state under the new experimental conditions and will:

- Investigate the density dependence of the $5s48s\,^1S_0$ spectral feature in Section 4.1
- Interpret the spectra using a multiple scattering framework in Section 4.2
- Describe work done to simulate direct laser excitation of the optically thick sample in Section 4.3
- Present an investigation of the time dynamics of the Rydberg excitation in Section 4.4
- Explore the spatial profile of the excited Rydberg ensemble in Section 4.5.

4.1 Spectra

In order to understand the broad spectrum observed in Figure 4.1, following the correction of the ion guiding field, the density dependence of the spectrum was investigated. As mentioned previously, an asymmetric broadening of the Rydberg spectrum is a well understood signature of a vdW many-body interaction [69, 70]. This arises due to the interaction shift, felt by atoms neighbouring an excitation, compensating the laser detuning. This tunes the transition back into resonance with a laser and is the the previously discussed anti-blockade effect. One would expect the emergence of this broadening to exhibit a density dependence due to the sensitivity of the $1/r^6$ interaction to the inter-particle spacing.

To measure the excitation spectrum of the $5s48s\,^1S_1$ Rydberg state, the procedure discussed in Chapter 3 was followed. The autoionisation laser was focused to try and reduce the effect of density averaging and the excitation time was fixed at $5\,\mu$s. The probe laser detuning was then scanned across the resonance while the coupling laser was locked on resonance, their respective Rabi frequencies being $\Omega_p = 2\pi \times 10\,$MHz and $\Omega_c = 2\pi \times 0.54\,$MHz. Each data point is the average of 100 shots taken with a

2 μs autoionisation pulse. A further 50 shots with no autoionisation pulse were taken for each detuning to characterise the spontaneous background signal. Data points were split into 6 × 25 shot blocks and the block order randomised. A ground state image was taken after each 25 shot block. This gives 6 absorption images in total for each value of the probe detuning. These images are then individually analysed and averaged to extract the ground state distribution. Finally the spectra were repeated at varying ground state densities by varying the loading time of the blue MOT from 20 ms up to 80 ms. The results are shown in Figure 4.2 for 4 such densities.

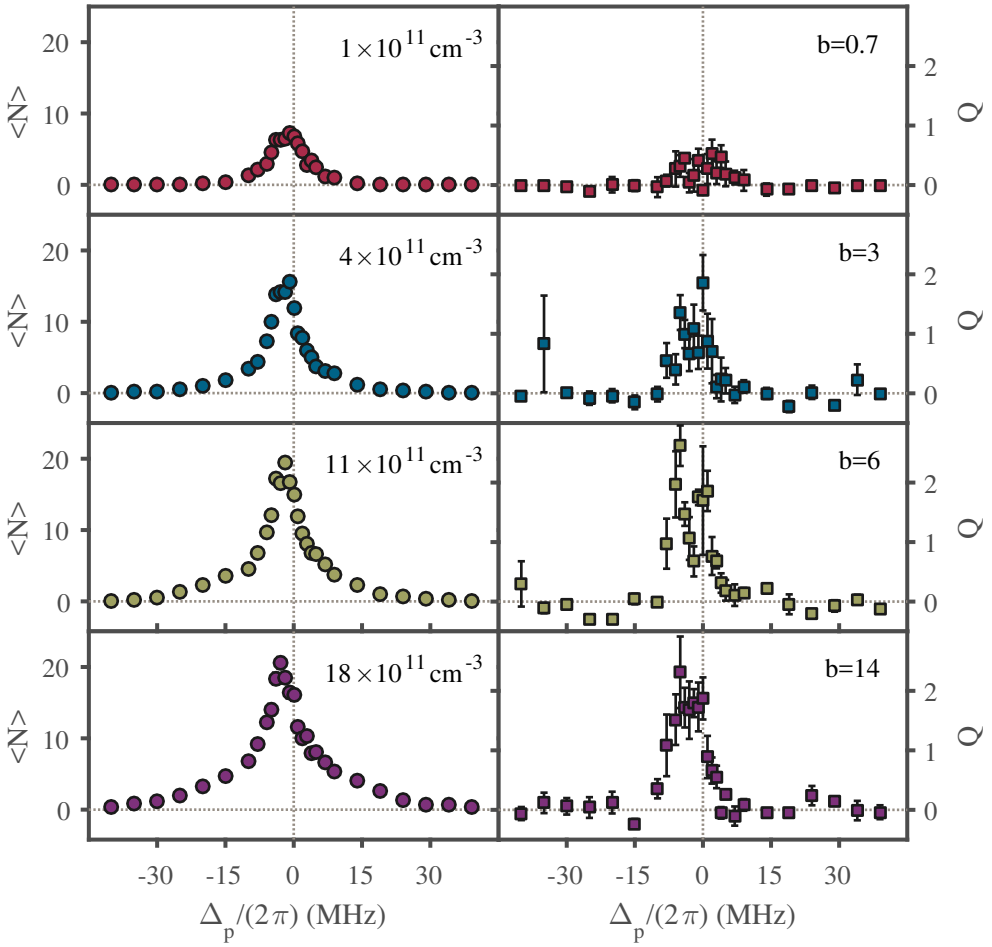

FIGURE 4.2: Experimental spectra as a function of the peak ground state density. The left hand panels show the mean ion count as a function of the probe laser detuning Δ_p and the right hand shows the Mandel Q parameter for each mean count. The left hand panels are labelled with the peak density and the right hand panels are labelled with the corresponding peak optical depth b.

The spectra clearly broaden as a function of density but, unlike the expected broadening due to the Rydberg blockade, we observe a symmetric broadening. The expected behaviour is illustrated in Figure 2.3. Consulting the corresponding Mandel Q plots

one would expect that for a blockaded sample, the Mandel Q parameter of the resulting ion signal would be suppressed on resonance. This behaviour has previously been observed [71]. In Figure 4.2 we observe that the centre of the spectrum demonstrates super-Poissonian noise. The super-Poissonian statistics observed in the centre of the spectra have been seen in previous experiments carried out within the Durham group [9]. The behaviour is the result of shot to shot variations in atom number, driving laser frequency, and laser intensity. These effects have been simulated and the super-Poissonian behaviour of the Mandel Q parameter reproduced [9]. Surprisingly though, the noise in the wings of the spectra appears to be close to Poissonian. This indicates that the signal in the wings of the spectra is some how fundamentally different from the signal at the centre.

4.1.1 Spectra Fitting

In order to extract parameters from the spectra measured in Figure 4.2 one must attempt to fit the data. Several functional forms of the fit function can be imagined. In previous studies of dilute samples [9] the OBE model of the system, described in Section 2.2.1, has proved to be useful. To fit the spectra in the first panel of Figure 4.2 we turned again to this OBE model. As the spectrum was clearly not centred around zero probe detuning, the detuning of the coupling laser was left as a fit parameter. Additional to this, the linewidths of the two excitation lasers and a scaling factor were all left as free parameters. The fit to the low density spectrum can be seen in Figure 4.3.

As the figure shows, the fit and the experimentally measured spectrum are in good agreement, with a reduced chi-squared value of $\chi_r^2 = 2.7$. It should be noted that χ_r^2 should only reduce to one in the case of Poissonian errors [72], we know *a prioiri* from the Mandel Q analysis that this will not be the case as the data has super-Poissonian errors. It should also be noted that the fitting routine found a minimum by allowing the probe laser linewidth to take a negative value. This is at odds with previous fits in lower density samples and is non physical. Indeed, as the figure inset shows that the error surface around this parameter is both smooth and steep, with the effectiveness of this fit severely reduced if the probe linewidth is fixed to a realistic 1.2 MHz. This is likely a result of the way in which the laser linewidth is implemented within the OBE model. Currently, frequency fluctuations are added as an additional decoherence term,

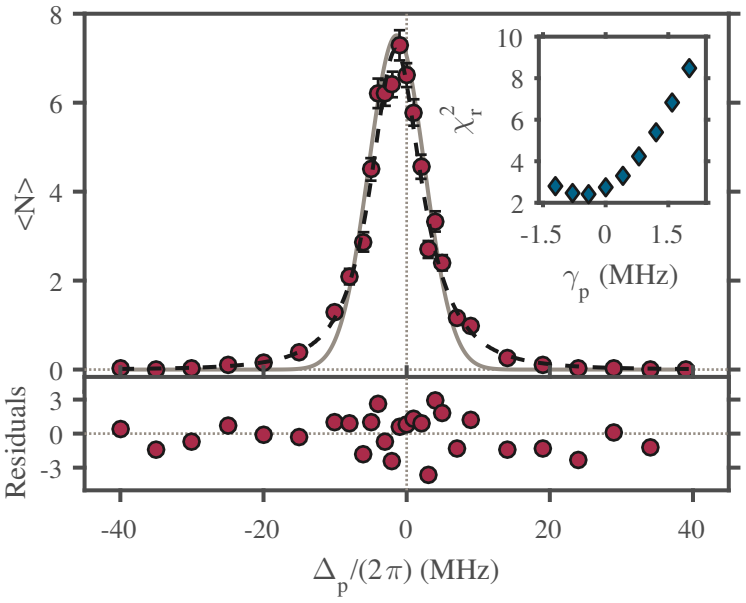

FIGURE 4.3: Lowest density spectrum from Figure 4.2 ($\rho = 8.1 \times 10^{10}\,\mathrm{cm}^{-3}$), the black dashed line is a fit to the data using the previously discussed OBE model. The solid grey line is a Lorentzian fit to the data. The residuals are normalised using the experimental error. Inset: Variation of the fit χ_r^2 for different fixed values of the probe laser linewidth.

assuming that the fluctuations are fast on the time scale of the experiment and always centred around zero detuning. Due to the low bandwidth of this laser lock, a more accurate description would be to see the laser noise as a fluctuating detuning in the two photon resonance and include the noise as an inhomogeneous broadening, rather than a homogeneous one. This implementation, while a more complete description, was not realised in this work, although could be a more effective model of the lineshape and noise character of the spectrum.

While the OBE model reproduces the data at low density it does not effectively describe the lineshapes at high density. In order to extract information from the spectra and to investigate the emergence of the spectral broadening, the remaining spectra from Figure 4.2 were fitted phenomenologically. Several fitting functions were investigated based upon both physical intuition and quality of fit.

Firstly, based upon the OBE fitting at low density, shown in Figure 4.3, the single lineshape that most closely matches the low density result is a Lorentzian and this forms one of our fitting choices. The other fits are based upon the hypothesis that there are actually two spectral components present. This hypothesis stems from the clear difference in error character between the wings and peak of the spectra demonstrated

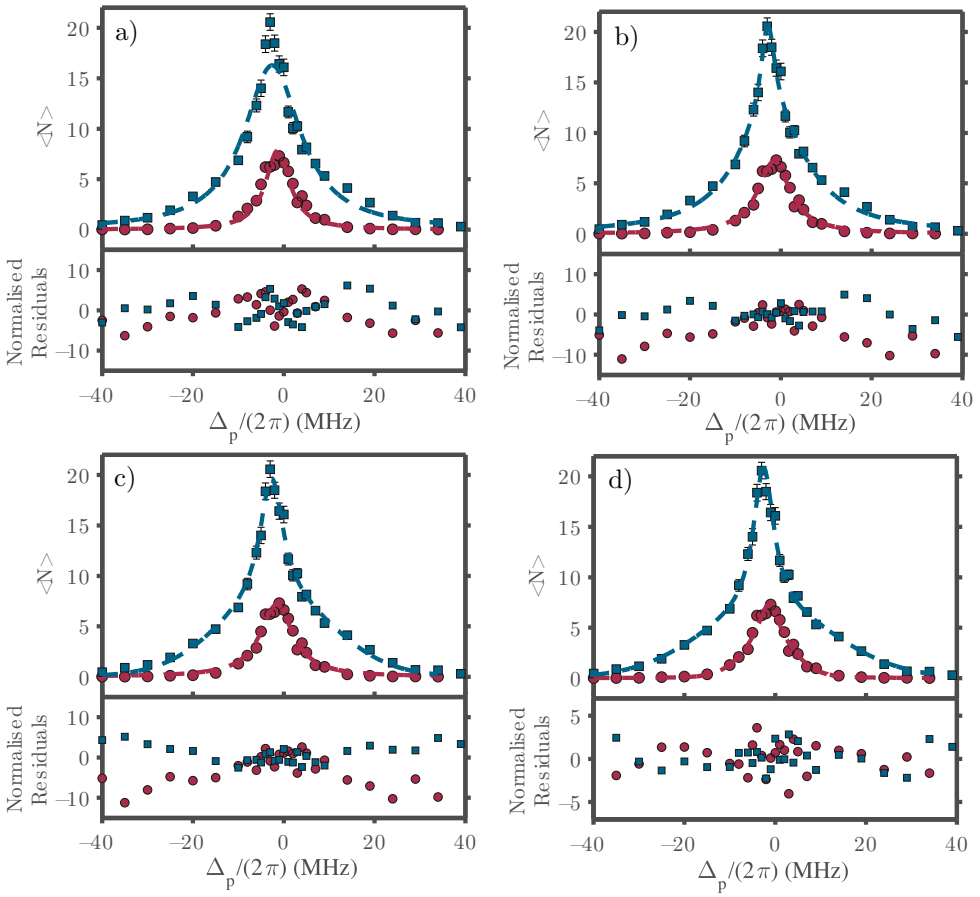

FIGURE 4.4: Spectra at two different densities with varying fit functional forms. Blue squares represent $\rho = 1.8 \times 10^{12}\,\mathrm{cm}^{-3}$ and red circles represent $\rho = 8.1 \times 10^{10}\,\mathrm{cm}^{-3}$. Subfigure a) is fitted with a Lorentzian, b) is a double Lorentzian fit, c) is a narrow unconstrained Lorentzian and a Gaussian with a width of 30.2 MHz, and d) is a narrow Lorentzian with a width of 2.8 MHz and an unconstrained Gaussian. All fits show the corresponding normalised residuals.

in the Mandel Q parameter, supporting a narrow component stemming from direct laser excitation with super-Poissonian statistics and a second broader component emanating from a separate excitation mechanism exhibiting a Poissonian character. To capture this behaviour two component fits based upon two Lorentzians and a combination of broad Gaussian and narrow Lorentzian are shown in Figure 4.4.

Figure 4.4(a) shows that the purely Lorentzian fit has clear structure in its residuals, simultaneously over-estimating the wings at low density and underestimating the peak at high density. Based upon it's poor χ_r^2 and structure in the residuals, this fit was deemed inappropriate lending credence to the two separate spectral features hypothesis. Figure 4.4(b) shows the outcome of a double Lorentzian fit. The χ_r^2 of this fit is better but the residuals again have structure in the wings. Figure 4.4(c) was fitted assuming that the broader feature has some connection to the intermediate state. As such, the

width of the second feature was constrained to 30.2 MHz. This analysis indicates that while the wings are over represented by the fit at low density, they are under-represented at higher density, implying that the width of this second feature is not constant. Finally Figure 4.4(d) shows a fit where the peak is represented by a fixed with Lorentzian and a variable width second Gaussian component. This fit has the least structure in its residuals and the best χ_r^2 value and, as a result, was implemented throughout the rest of this work.

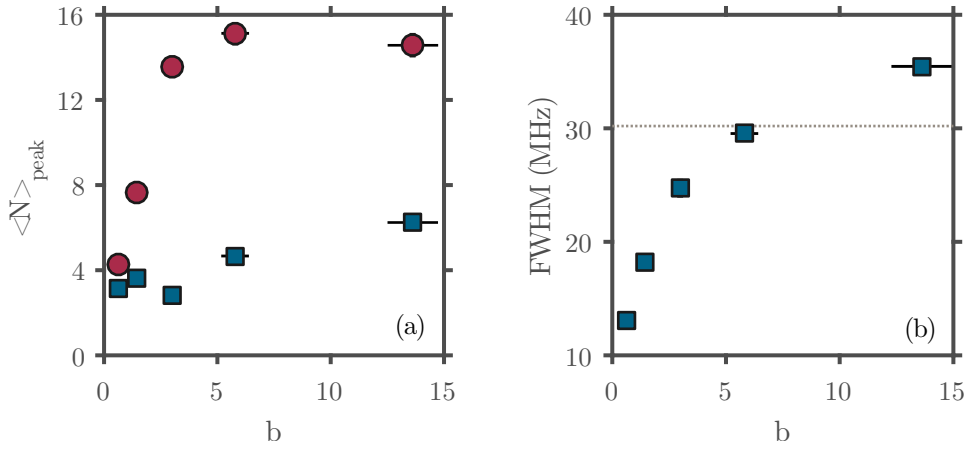

FIGURE 4.5: (a) Amplitude of the narrow Lorentzian component (red circles) and of the broad Pedestal component (blue squares) as a function of sample optical depth b. (b) FWHM of the broad Pedestal component (blue squares) as a function of optical depth b.

From the results of the fitting we extract information on the growth of the two identified components. These two components will be referred to for the rest of the work as the Pedestal and Narrow components for clarity. Relevant parameters of the fits are shown in Figure 4.5, where they are plotted against the optical depth of the sample. This measure was chosen as it is the parameter measured in the absorption images and allows for simple comparisons between different sample geometries.

Figure 4.5(a) clearly shows that the amplitude of Narrow spectral component rapidly saturates with optical depth and therefore density (as b is linearly related to peak density). This could be indicative of the Rydberg blockade mechanism and will be discussed further in Section 4.3, with discussion now focusing on the Pedestal component. Interestingly, Figure 4.5(b) shows that the width of this Pedestal is of the same order as the intermediate state linewidth and evolves with optical depth.

The figure also shows that the two-component fit invokes a non-zero Pedestal amplitude in the case of low optical depth. As the data are well fitted by the OBE in the regime,

which does not predict this component, this is likely an artefact of the analysis and lack of data to constrain the behaviour of this feature at lower density. To reduce the number of free parameters and better constrain the behaviour of the Pedestal at the lower optical depths, we can independently fit the Pedestal. First the Mandel Q parameter is used to to identify regions that are purely Pedestal signal, with data exhibiting Poissonian errors characterised as Pedestal.

Analysis of the Mandel Q indicates that data points more than 10 MHz from resonance can be characterised as Pedestal. This is consistent with the decay of a central Lorentzian feature of 2.8 MHz width, with the total signal contribution being approximately 1/64th the peak value at a detuning of 10 MHz. With the data that is almost purely Pedestal extracted, this can be fitted independently and the results used to validate the two component model. The fitting function that was found to be most appropriate to this extracted wing data was a Gaussian and the fit results are shown Figure 4.6. The Pedestal amplitudes extracted in this way are consistent with the high density two component fits.

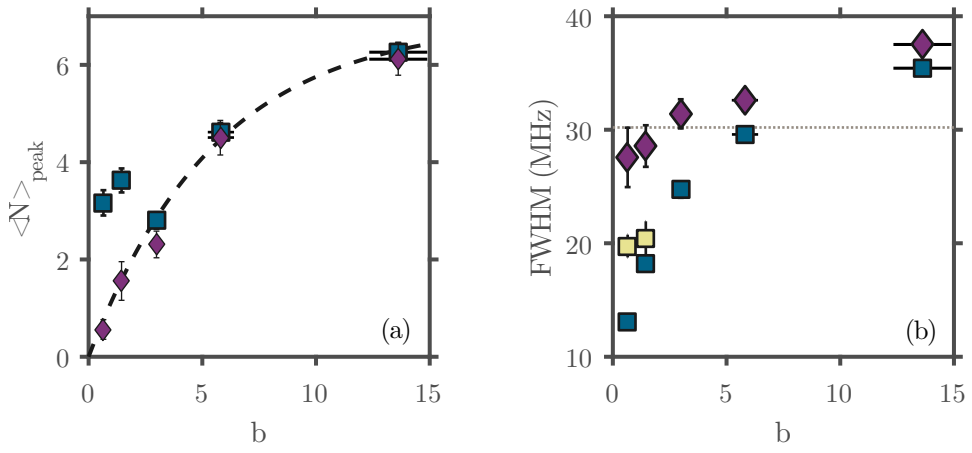

FIGURE 4.6: (a) The amplitude of the Pedestal component as a function of sample optical depth b as extracted from the two component fits (blue squares) alongside the amplitudes extracted from a Gaussian fit to just the wings of the spectra (purple diamonds). Also plotted is the saturation fit, described in the text, to the three points with highest optical depth (dashed black line). (b) The FWHM of the feature as a function of sample optical depth b as extracted from the two component fits (blue squares) alongside the FWHM extracted from the Gaussian wing fit (purple diamonds). The width, as given by constraining the Pedestal height as discussed in the text, is shown (yellow squares). Finally, the grey dotted line is set at 30.2 MHz, the intermediate state linewidth.

A second method of constraining the fit is to use the two-component Pedestal fits at high density, where signal is abundant, to constrain the points at lower density. It has

been experimentally verified that in the absence of atoms ($\rho = 0\,\mathrm{cm}^{-3}$) then $\langle N \rangle = 0$, which can be used as an additional constraint. Using the three highest density spectra it is found that a saturation fit of the form $\langle N_{peak} \rangle = A/(1 + (B/b))$, where A is the peak signal and B the optical depth at saturation, is appropriate. This fit has a low χ_r^2 and is presented in Figure 4.6(a). The saturation fit also shows good agreement with the widths obtained when the Pedestal feature is fitted in isolation using the method previously discussed. Using this fit, the amplitude of the Pedestal component within the two-component fit can be fixed and the data refitted to extract a new Pedestal width for completeness, shown in Figure 4.6(b). Following this procedure, a robust measure of the Narrow feature height for all densities is obtained. Additional to this, the width and height of the Pedestal feature at high density is well characterised and can be inferred with some confidence at lower densities.

It is clear from Figure 4.6(a) that the Pedestal amplitude is strongly dependent on the optical depth of the sample and therefore so must be the driving field that is exciting this signal. This driving field appears to be proportional to density and, as the probe laser is increasingly extinguished with optical depth, this suggests that what is actually being measured is a trapped population of photons that have been scattered from the probe laser. Based upon this two component nature of the spectra the following sections will examine the Pedestal and Narrow features in isolation.

4.2 Multiple Scattering

The origin of the Pedestal component has so far not been discussed but there are several pieces of information around which we can form a hypothesis. What is clear from Figure 4.6 is that the the behaviour of the Pedestal feature is sensitive to the optical depth of the sample and at the lowest optical depths, the amplitude of the Pedestal is negligible compared to the amplitude of the Narrow feature. The second thing of note is that the Pedestal width is of the order of the intermediate state lifetime. This is at odds with what is expected from a laser driven coherent excitation, where the feature linewidth is typically an order of magnitude lower than Γ_e. The final piece of the puzzle is that the error character of this feature is distinct and Poissonian, something we do not expect due to detuning fluctuations on the excitation lasers. This shows a second and distinct population of Rydberg atoms that are not excited by the probe laser. This

would have to be excited by photons that have a spectral width much greater than that of the probing laser. This large width would broaden the spectral feature and reduce the Rydberg excitation's sensitivity to frequency fluctuations, lowering the technical noise and thus allowing the Mandel Q parameter to tend toward Poissonian.

This second population of photons only appears to be significant for optical depths of $b \geq 1$. Our hypothesis is that the origin of the Pedestal is multiple photon scattering. This is when probe photons that are scattered from the beam are reabsorbed and can, in conjunction with the coupling laser, excite atoms to Rydberg states. This concept of photon trapping within atomic samples has been known for many years and has direct implications for MOTs, where trapped cooling photons limit the achievable phase space density [73, 74]. This is the previously discussed density limited regime. Direct trapping of photons from a probing beam has also been observed [75] and previously investigated [76].

As a rule of thumb to check the feasibility of trapping, one can consider the likely number of scattering events per incident photon [77] $N_{scat} \approx b^2$, where N_{scat} is the number of individual scattering events per photon. This relationship comes from the random walk nature of the process and the definition of $b = 1$. The relationship tells us that the number of scattering events in the densest sample of Figure 4.2 is likely to be on the order of $N_{scat} = 200$, discounting any additional geometric factors. This high a number of potential scattering events indicates that the scattered light field cannot be neglected safely and needs to be considered in greater detail. Additionally, each scattering event impacts the spectrum of the emitted photon. If the photon is scattered elastically, the spectrum will evolve due to the introduction of successive Doppler shifts. However, if the photon is scattered inelastically then the dominant influence on the spectrum will be the homogeneous linewidth of the intermediate state rather than the Doppler effect.

While these frequency redistribution mechanisms allow the rescattered field to have a different spectrum to that of the probe laser, only elastic scattering allows photons to have a linewidth lower than that of the intermediate state. The total intensity scattered by an atom consists of both an elastically scattered component and an inelastically scattered component. Working within a two-level approximation [78] the fractional

intensity of the elastically scattered component is given by

$$\frac{I_{scat}^{el}}{I_s} = \frac{1}{1+s}, \tag{4.1}$$

where $s = 0.4$ in our experiments and represents the saturation parameter of the probing laser. In this regime the principal contribution should be from elastic scattering and will be considered in the next section to see if the width of the spectra can be predicted.

4.2.1 Doppler Broadening

For atoms at rest, the elastically scattered component shares the same spectral properties as the incident light, apart from a small recoil redshift. However, it has long been known that this is not true for atoms at finite temperature [79].

Upon scattering from a finite temperature atom, the incident photon will acquire a Doppler shift of order $k\bar{v}$, where $\bar{v}$ is the average atomic velocity and k is the incoming photon wavevector. It follows then that this effect can be safely neglected as long as the following criterion holds,

$$k\bar{v} \ll \Gamma_e. \tag{4.2}$$

In this limit, the frequency of the photon is not significantly perturbed and coherent scattering effects can still be observed [80]. This is only valid in the case of a single scattering event and for large optical depths many scattering events may occur per photon, as previously discussed. It follows that even if the single event is small enough to be neglected, the total shift acquired over many chained events has no such limit.

For a typical photon within a dense sample, its trajectory through the cloud can be viewed as a random walk where each step is typically given by the photon's mean free path. This path length is given by

$$\ell = \frac{L}{b}, \tag{4.3}$$

where L is the length of the medium. This random walk behaviour gives rise to the requirement of a photon requiring b^2 scattering events to traverse the medium and escape. If the successive scattering events can be treated as independent then it follows that the photon will perform a random walk in frequency space with each step being $k\bar{v}$. Therefore the total acquired Doppler shift is approximated by $\sqrt{N}k\bar{v}$ or $bk\bar{v}$. This

allows us to rewrite equation 4.2 for a multiply scattered photon as:

$$bk\bar{v} \ll \Gamma. \tag{4.4}$$

When considering this broadening, one must however bear in mind that the chance of re-absorption has a Lorentzian form and so the above is only true if the initial photons are resonant. If the probing beam is not initially resonant then the medium applies a selection pressure, whereby photons diffusing away from resonance are less trapped by the media and thus more likely to be lost. Meanwhile, photons defusing towards resonance will be more strongly trapped. The consequence of this is that over time the trapped photon population will diffuse towards resonance and redistribute around $\Delta = 0$. This effect has been modelled and is discussed in reference [81].

Under the standard experimental conditions described in this thesis (where the initial sample temperatures are around $10\,\mu$K) the residual Doppler shift should be in the region of 65 kHz. Even at our highest achieved optical depth of $b = 26$, the total accumulated redistribution should be of order 2 MHz and significantly lower than the 30.2 MHz intermediate state linewidth. Key to this argument is that the back action on the atomic ensemble can be neglected, which is only true for small numbers of events. Additionally, all previous treatments of this problem have imposed the limit of low input light intensity such that equation 4.1 tends to purely elastic, which in the case of the experiments in this thesis is not true. In addition to elastic scattering, there will also be an inelastically scattered component to the re-scattered field.

4.2.2 Inelastic Scattering

As the atom is driven harder, the population of the excited state becomes significant and spontaneous emission plays a larger role. This changes the spectrum of the scattered light. This inelastic scattering does not share its spectral characteristics with the laser and forms a completely distinct photon population. For a simple two-level atom driven by monochromatic radiation, the fluorescence spectrum gives rise to the Mollow triplet [82] due to the dressing of the energy levels by the driving field. The net result is a set of sidebands separated from the central emission feature by the Rabi frequency Ω of the driving field. The Mollow triplet for multiple driving field saturation parameters is plotted in Figure 4.7.

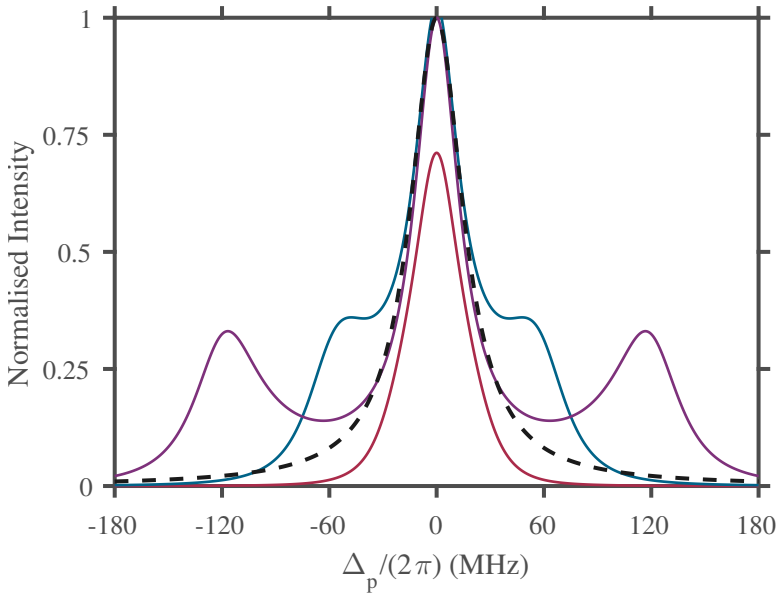

FIGURE 4.7: The normalised fluorescence spectrum of an isolated two-level atom with $\Gamma = 2\pi \times 30.2$MHz for $s = 0.4, 2, 4$ are given by the solid red, blue, and purple lines respectively. These demonstrate the distinctive Mollow triplet. The normalised power-broadened absorption bandwidth of the intermediate state (at $s = 0.4$) is represented by the dashed black line. Simulation performed using code based upon [83].

While the Mollow triplet well describes the inelastic emission spectrum of isolated atoms and has been confirmed experimentally [84], the spectrum of the photons trapped within a cloud of many scatterers will be different. The spectrum of the trapped photons is influenced by both fluorescence and absorption processes, since photons outside of the absorption bandwidth will not persist within the cloud. The power broadened absorption spectrum of the atoms within the two-level approximation is also plotted in Figure 4.7.

The importance of the inelastically scattered component is entirely dependent upon the strength of the driving field. As these scattering events, both elastic and inelastic, should contribute to heating the cloud then in principle one can use this heating to extract the intensity of the trapped photon field. This knowledge can then be used to further understand how the inelastic scattering process shapes the spectrum by predicting the shape of the resulting Mollow triplet.

4.2.3 Sample Heating

Outside of the weak-probe limit, not only will each photon experience multiple scattering events but so, in turn, will each atom within the sample experience multiple scattering events. Each atom that scatters a photon will receive the associated recoil kick and over many scattering events this will lead to direct heating of the sample. As the chance of rescattering is related to the detuning of the probing laser, so should the heating of the sample due to multiple scattering. Previous treatments of multiple scattering have all neglected this back action upon the atomic sample [75, 85, 86] but it is possible to investigate this within the dataset described in Figure 4.2 by looking at the the velocity distribution following excitation. To do this, we would normally measure the cloud size before and after a variable period of ballistic expansion. As we only have a single image for each point on the spectra, we use the cloud side measured post excitation and the cloud size without any excitation to define an effective 'two point' temperature. This is done via the relation

$$\sigma(t)^2 = \sigma(0)^2 + \frac{k_B T}{m} t^2, \tag{4.5}$$

where $\sigma(t)$ is the Gaussian width of the cloud post excitation, $\sigma(0)$ is the Gaussian width measured in the absence of any Rydberg excitation with no ballistic expansion time, m is the atomic mass of strontium, and k_B is the Stefan–Boltzmann constant.

Figure 4.8 demonstrates that there is significant heating during the excitation pulse at high optical depth. This heating results in an appreciable expansion of the cloud between the time of the excitation and the time of the imaging pulse. Before this effect can be linked to multiple scattering, one must first rule out two further mechanisms that could be modifying the cloud's width.

The first is direct heating from the probing laser. Absorption from the probing laser will have two effects. Firstly it will accelerate the atoms in the probing beam direction but, due to the orientation of the camera and probing laser, this effect will not be observable. The second consequence will be heating due to the spontaneous emission. Calculating this on resonance one must first calculate the expected number of scattering events, which with $s = 0.4$, $\Delta_\mathrm{p} = 0$ and working within the two-level approximation, should be around 135 photons for a 5 μs excitation. Then by assuming that the recoils cause

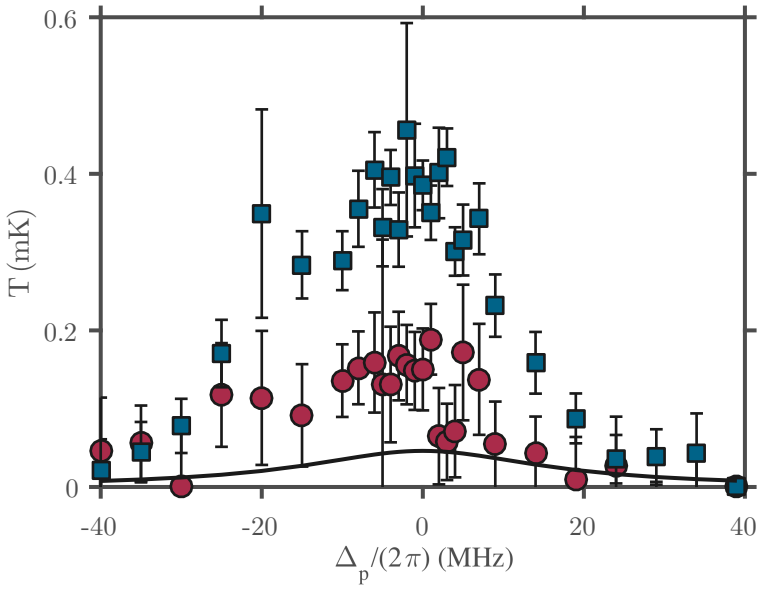

FIGURE 4.8: The two point temperature, post Rydberg excitation, as a function of detuning for a sample of optical depth $b = 14$ (blue squares) and one of optical depth $b = 0.6$ (red circles). The direct heating expected from the excitation beam is shown for reference (black line).

the atom to undergo a random walk in momentum space, one can use equipartition theorem to extract a temperature.

$$\begin{aligned} T &= \frac{N\hbar^2 k^2}{3k_B m} \\ &= 46\,\mu\text{K}, \end{aligned} \tag{4.6}$$

which is significantly less heating than we observe.

The second process that could be responsible for modifying the Gaussian width of the sample is a mechanical effect originating from Rydberg-Rydberg interactions. While we believe that the $5s48s\,^1S_0$ state is attractively interacting, a repulsive force could account for the rapid change in cloud width. To test the Rydberg-driven expansion hypothesis a series of cloud ballistic expansions were taken and are presented in Figure 4.9. These expansions show that with no excitation pulse the cloud expands demonstrating a temperature of $13\,\mu$K but that the addition of probe light, with or without the coupling laser, results in significant heating. Unlike a thermalised sample, the expansion shows that there are distinct velocity classes within the cloud, which is consistent with photon trapping. At long times, we see the expansion of a slower class of atoms that

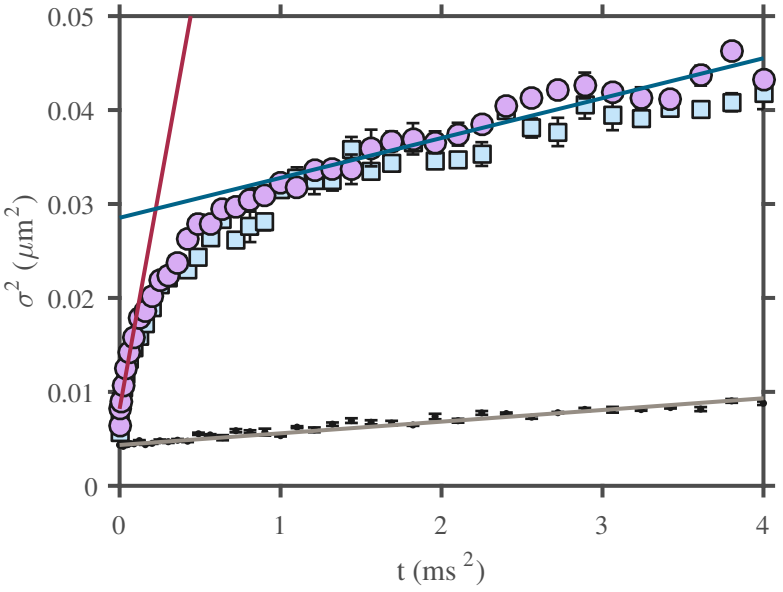

FIGURE 4.9: Ballistic expansion of a Broadband MOT of optical depth $b = 26$. Purple circles represent a MOT post a 5 μs Rydberg excitation pulse. The red line is a linear fit to the initial expansion points and the blue line a fit to the data at later times. These fits yield MOT temperatures of 0.7 mK and 35 μK respectively, which demonstrates that the cloud is not in thermal equilibrium. Blue squares represent a MOT following a 5 μs probe laser only pulse. Finally black dots represent the expansion of an unperturbed sample and the grey line the corresponding fit yielding a temperature of 13 μK.

have a temperature broadly consistent with direct laser heating, still significantly hotter than the case of no excitation light. In contrast, at short times we see the rapid expansion of a hot component which we can attribute to atoms in the high density core of the sample being heated by multiply scattered photons. This short time behaviour is consistent with the two point temperature heating observed in Figure 4.8.

It is clear then that significant additional heating, far beyond what we expect from the probing pulse alone, is occurring and we need to take another look at the two scattering mechanisms. In the case of the elastic scattering, the additional heating allows the amount of redistribution to be re-estimated using the new final temperature of the cloud and the relation in equation 4.4. This predicts the total accumulated redistribution should be of order 20 MHz. This level of broadening is now of order of the intermediate state linewidth and no longer negligible for high density clouds as the effect scales with b^2.

In addition to estimating the width of the elastically scattered component of the field, in principle one can also extract the intensity of the heating field from this data too.

This can be done by considering the number of scattering events required to cause the observed heating, much like how equation 4.6 was used to rule out laser induced heating. To do this we can estimate the number of scattering events by working out the number of velocity kicks required to reach the final observed velocity and assuming the velocity is a random walk process. This gives:

$$\frac{v}{v_{rec}} = \sqrt{2N}, \tag{4.7}$$

where the factor of 2 comes from the fact that the incoming photon direction can be assumed to be random and thus each event generates two recoil kicks. By assuming that the photon trapping time is short compared to the excitation pulse, and that therefore the rescattered field's build-up time is short, one can convert the number of events N_{scat} into an average rate and then equate this to an average saturation intensity via the two-level scattering rate approximation on resonance

$$\frac{v^2}{2\tau v_{rec}^2} = \frac{\Gamma_e}{2}\frac{s}{s+1}. \tag{4.8}$$

This equation can then be rearranged to yield s.

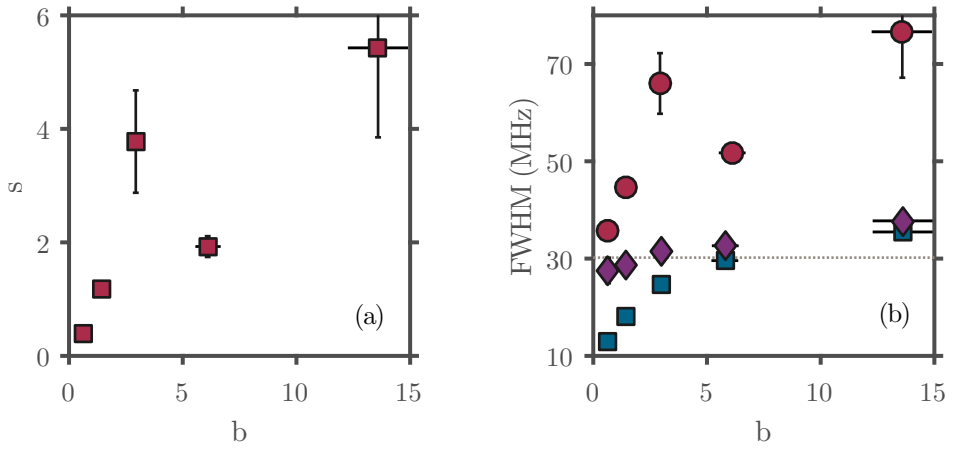

FIGURE 4.10: (a) The trapped intensity as a function of the optical depth as calculated from equation 4.8 (red squares) for the spectra presented in Figure 4.2. (b) The FWHM of the Pedestal as a function of optical depth obtained from the trapped intensity (red circles), wing fits (purple diamonds), and two component fits (blue squares). The linewidth of the intermediate state is shown for convenience (grey dotted line).

Each of the spectra in Figure 4.2 have associated heating information and one can convert this to a trapped intensity using this method, the result of which is plotted in Figure 4.10(a). This analysis seems to indicate that the trapped intensity is significant and becomes more so at higher optical depths. This optical depth dependence is

expected intuitively but the accuracy with which the field can be measured from this dataset is limited.

In principle one can use the field intensity, and the assumption that the dominant effect upon the spectrum is the absorption cross-section, to infer the spectral width of the trapped field. This is done by assuming that the absorption cross-section power broadens as $\Gamma' = \Gamma\sqrt{1+s}$. This width is shown in Figure 4.10(b) for the spectra data. The widths calculated are significantly higher than the widths extracted by other means and are not consistent with the measured spectra. In all of these treatments we have assumed that the photon undergoes a random walk. In the core of the sample this is true as the density gradient is low, this in not true as the distance from the centre increases. This drop in density will create an asymmetry in the photons direction of travel with a net flow of photons out of the dense core. This outflow will create an effective force that accelerates the expansion of the cloud. To further understand the heating, the outflow effect, and their relationship to frequency redistribution, the time dependence of the trapped field was investigated.

4.2.4 Trapped Field Time Dependence

Using the same method by which the density dependence of the spectra was measured, however this time changing the excitation pulse duration, one can map the time evolution of the Pedestal in the case of a optically thick Broadband sample. Investigating the rise time and the spectrum of the trapped field will give additional information regarding the trapping dynamics and how the evolution of this field governs the heating of the sample and broadening of the spectra.

The obtained spectra are plotted in Figure 4.11 along with their corresponding fits. As the figure shows, even at the shortest excitation pulse achievable (limited by the AOM switching time) there is still appreciable excitation that can be attributed to the Pedestal.

The width of the Rydberg spectrum as a function of the excitation time, obtained from the data in Figure 4.11, is plotted in Figure 4.12(a). The rapid saturation of the Pedestal FWHM is consistent with the rescattered field quickly reaching a maximum intensity. One would expect the timescale of this saturation to be related to the lifetime

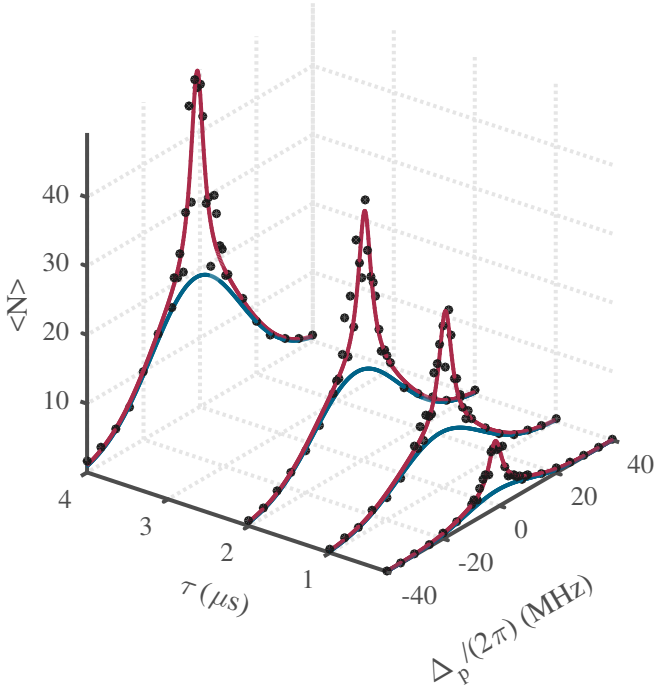

FIGURE 4.11: The Rydberg spectra as a function of excitation time, τ, (black points) along side the Narrow component (red lines) and Pedestal component (blue lines) fit contributions.

of a photon within the cloud. This lifetime τ' is given by

$$\tau' = \frac{3}{\alpha\pi^2}\tau_{nat}b^2, \tag{4.9}$$

where α is a geometric factor (calculated in [76]) that is equal to 5.35 for a spherical Gaussian and $\tau_{nat} = \Gamma_2^{-1}$. This gives a build-up time in our system of the order of 100 ns. Interestingly the FWHM saturates on a timescale not inconsistent with this build-up time.

This apparent rapid evolution into the inelastic regime, shown by the rapidly saturating spectra FWHM, can be explained by considering equation 4.1. For a trapped field of any appreciable intensity, the probability of scattering elastically may not be unity for the first event but there is not just one event. In a sample of optical depth $b = 17$ the number of scattering events ($\sim b^2$) almost guarantees that the photon will enter the inelastically scattered mode.

Turning to the peak Pedestal Rydberg signal, plotted in Figure 4.12(b), N_{peak} does not appear to saturate as quickly as the Pedestal FWHM. This however is effectively a detector response time limitation. The Rydberg excitation, which is being used to

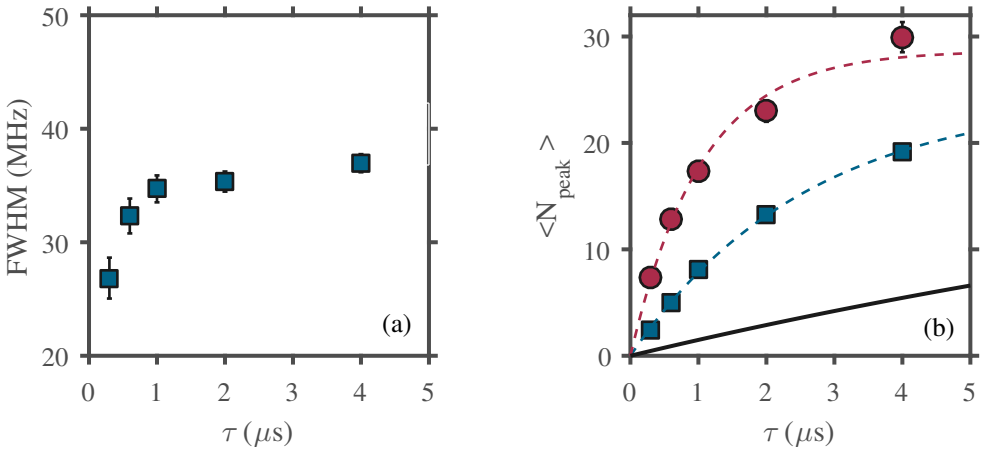

FIGURE 4.12: (a) The FWHM of the Pedestal as a function of excitation time (blue squares). (b) The amplitude of the Narrow component (red circles) and Pedestal component (blue squares) as a function of excitation time alongside their respective saturation fits (dashed lines). Also plotted is the non-interacting OBE simulation result (black line). The saturation fits are of the form $A/(1+\exp(-B/\tau))$ and the OBE result is scaled by the peak signal of the Narrow component.

probe this field, has it's own time dynamics. For a non-interacting laser driven sample this saturation time is predicted by the OBE model to be 15 μs and is also plotted in Figure 4.12(b) for convenience. The fitted saturation times of both the Pedestal and Narrow features are not only significantly faster than that predicted by the OBE model, with fitted saturation times of $(1.0 \pm 0.1)\,\mu$s and $(2.6 \pm 0.2)\,\mu$s respectively, but also different from each other.

This large disparity between predicted and observed time dynamics between the two components could be an indication of coherent processes taking place within the sample, whereby the many-body interaction is giving a speed up of the excitation dynamics. As the blockade radii would differ for Pedestal and Narrow component Rydberg atoms, so too would the degree of speed up, with the Narrow component intuitively saturating faster due to its larger blockade radius. This effect will be be investigated in Section 4.4. What is clear is that if one is to use the spectra to accurately measure the build-up time of the trapped photon field then it is worth considering the timescale imposed by the Rydberg excitation and that a move to a lower n state would be advantageous as it would speed up these dynamics.

In addition to the full spectra, a dataset was acquired in which the probe laser was fixed on resonance and the excitation time varied more finely to measure the temperature increase of the cloud as a function of excitation time. This is presented in Figure 4.13

and shows that the short time cloud width increases linearly with τ. This constant heating rate indicates that the scattering rate is also constant, as equation 4.6 shows that temperature is linear with number of scattered photons.

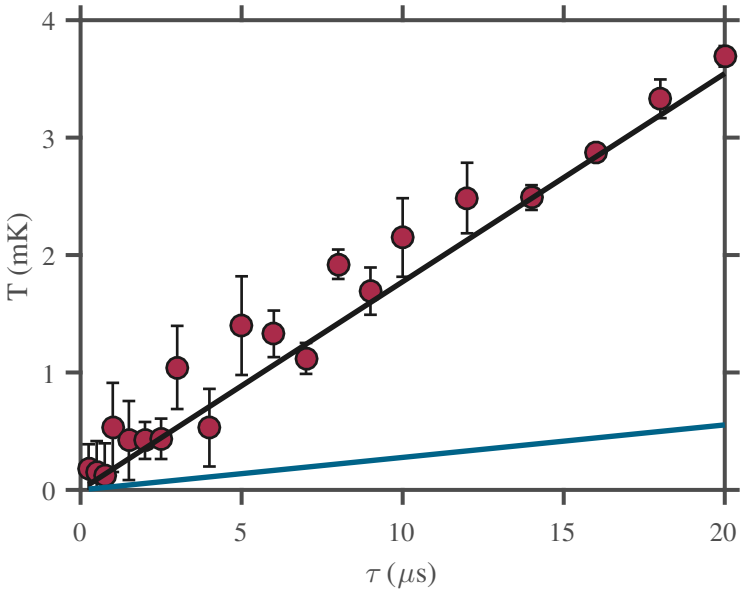

FIGURE 4.13: (a) The temperature of the sample as a function of time as calculated by the two-point method detailed in the text (red circles) and a linear fit to the data (black line). Also plotted is the heating rate associated with the excitation laser (blue line). Sample optical depth was $b = 17$.

When equation 4.8 was again used to convert the expansion of the cloud into a trapped intensity it was found that to produce the observed heating a scatting rate of $> \Gamma_e/2$ was required. As the atoms cannot scatter at the rate calculated, the information that can reliably extracted from the sample heating is limited without further investigation of the cloud's expansion at short timescales post excitation. This would allow the outflow acceleration to be separated from the heating effects and their relative contributions determined. Despite these limitations, we have shown that there are non-trivial and non-Maxwellian heating dynamics within the excited samples that can only be currently explained by invoking a trapped photon population.

4.3 Behaviour of the Narrow Feature

While the previous section considered only the Pedestal feature of the spectrum, working within the assumption that the photon populations are spatially separate, this

section will attempt to explore the coherent feature identified in Figure 4.2 by modelling the propagation of the laser beam through the sample and calling on the OBE model described previously. The key assumption here is that multiple scattering does not contribute to this feature, to go beyond this assumption a more complete model would be required. Nevertheless, optical depth is still key as the attenuation of the probing beam will alter the spatial distribution of the excitations.

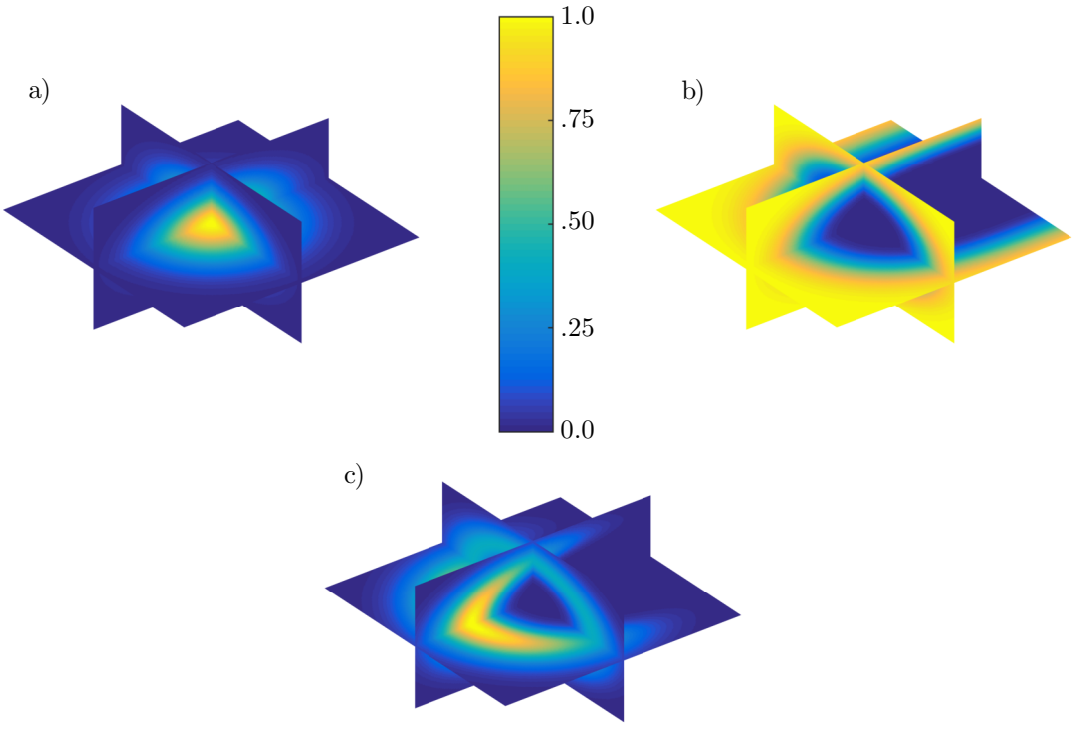

FIGURE 4.14: (a) The spatial distribution of the ground state atoms. (b) The spatial distribution of the probe beam intensity, demonstrating the shadow cast by the atom cloud. (c) The spatial distribution of the Rydberg atoms in the case of an optically thick sample. All panels are normalised, share the same colour bar, and were calculated for the same ground state and excitation beam parameters.

Firstly, it is of interest to examine the behaviour of the laser beam itself. Figure 4.14 shows the variation of the laser beam intensity within a model cloud of the same geometry and density as that of the most optically thick sample investigated in Figure 4.2. The propagation simulation clearly shows that the probe beam does not penetrate into the sample, meaning Rydberg excitation in the sample core should be minimal, which is also shown in the figure.

The steps involved in this simulation are as follows:

1. The non-interacting OBE model discussed in Section 2.2.1 is used to calculate the Rydberg excitation fraction and the absorption coefficient for a range of probe

beam intensities (0 - 0.4 I_{sat}). This is used as a lookup table throughout the rest of the simulation.

2. A 3D Gaussian density distribution is defined on a grid. This distribution has a peak density and set of Gaussian widths that match the experimentally measured samples. This element of the simulation is shown in Figure 4.14(a).

3. The probe beam is propagated along a predefined axis through the simulation grid. This is achieved by setting the first simulation plane to the intensity of the probing laser and then using the Beer-Lambert law, in conjunction with the pre-calculated lookup table of absorption coefficients, to calculate the intensity within the cells of the next plane. In this way the intensity profile of the probing beam is calculated within every cell in the simulation grid. The propagation of the beam includes both the saturation behaviour of the intermediate state and the coherent EIT [87, 88] effect that would facilitate the propagation of the laser further into the cloud while the coupling beam is present. This element of the simulation is shown in Figure 4.14(b).

4. The Rydberg population is then calculated using the probe beam intensity within every grid cell. This is done by using the grid cell intensity to interpolate a pre-calculated Rydberg excitation fraction ρ_{33} and then multiplying by the grid cell ground state density to give a Rydberg excitation density. Finally this density is converted to a population by multiplying through by the volume of each grid cell. This element of the simulation is shown in Figure 4.14(c).

5. The Rydberg population is integrated to give a simulated N_{peak}. To compare the simulation directly to the experiment, the effect of the autoionisation laser interrogation region has to be incorporated. This is done by defining a rectangular volume through the simulated sample and integrating only within this volume. The shape and volume of this region is matched to that of the 408 nm autoionisation laser beam.

The simulation confirms that excitation takes place only in the wings of the sample, even with EIT effects included, as the probe beam is rapidly attenuated in the wings of the cloud. By adding a detuning dimension to the simulation lookup table, it can also be used to estimate the expected number of ions as a function of density for a

given detuning. Using a similar approach to that used in Figure 4.3, the lowest density spectrum in Figure 4.2 is again fitted using the laser linewidths and a scaling factor as free parameters. Unlike the previous fit, this scaling factor now has direct physical significance. If the autoionisation interrogation region is correctly defined then this scaling factor corresponds to a measure of the experimental detection efficiency. While measuring the autoionisation beam waist inside the vacuum chamber is impossible, the waist was measured in free-space to be $(6 \pm 1)\,\mu$m. Using this waist to define the simulation interrogation region, the detector efficiency was calculated to be $\sim 6\%$ from the fit. In Section 3.4.3 it was outlined that the detector efficiency was deliberately lowered in order to prevent the MCP saturating, as a result the current value differs from that in the groups earlier work [9].

Using the parameters obtained from the above fitting, the simulation can then be used to model the data presented in Figure 4.5 with no free parameters. The results of this simulation are shown in Figure 4.15. The clear agreement between the model and the data suggests, at least in the absence of multiple scattering and interactions, we can have confidence in the model.

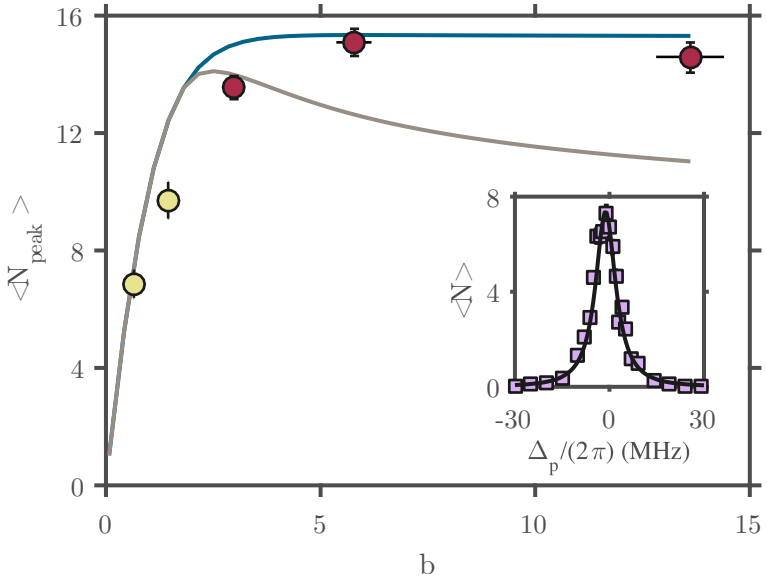

FIGURE 4.15: Plotted are the results of the optical depth simulation described in the text, using fit parameters from the simulation in the inset, for $\rho_b = 4 \times 10^{10}\,\mathrm{cm}^{-3}$ (blue solid line) and $\rho_b = 0.4 \times 10^{10}\,\mathrm{cm}^{-3}$ (grey dashed line). The amplitudes of the laser excited Rydberg component (red circles) and the corrected amplitudes as described in Figure 4.6 (yellow circles) are shown for comparison. Inset: Data previously presented in Figure 4.3 showing the Rydberg signal as a function of detuning for a low density sample (lilac squares) and the corresponding fit using the optical depth model (black line).

Also included within this simulation is an attempt to capture the effect of the Rydberg blockade. To incorporate this effect into the model, the Rydberg density distribution is truncated at a value equal to the blockade density ρ_b, capping the maximum number of excitations within a volume. The blockade density is calculated using the blockade radius obtained using the C_6 coefficient calculated in [22], as there is no conclusive experimental measurement available. The calculated values for the $5s48s\ ^1S_1$ state are: $C_6 = 4.7\,\text{GHz}.\mu\text{m}$, $R_b = 3.6\,\mu\text{m}$, and $\rho_b = 4\times10^9\text{cm}^{-3}$. These values were calculated for an excitation laser bandwidth of 3 MHz. It should be noted that while this mechanism was incorporated into the fit presented, it is not responsible for the saturation and to test this the truncation was removed and the simulation repeated with no significant difference observed. The saturation appears to come purely from optical depth effects.

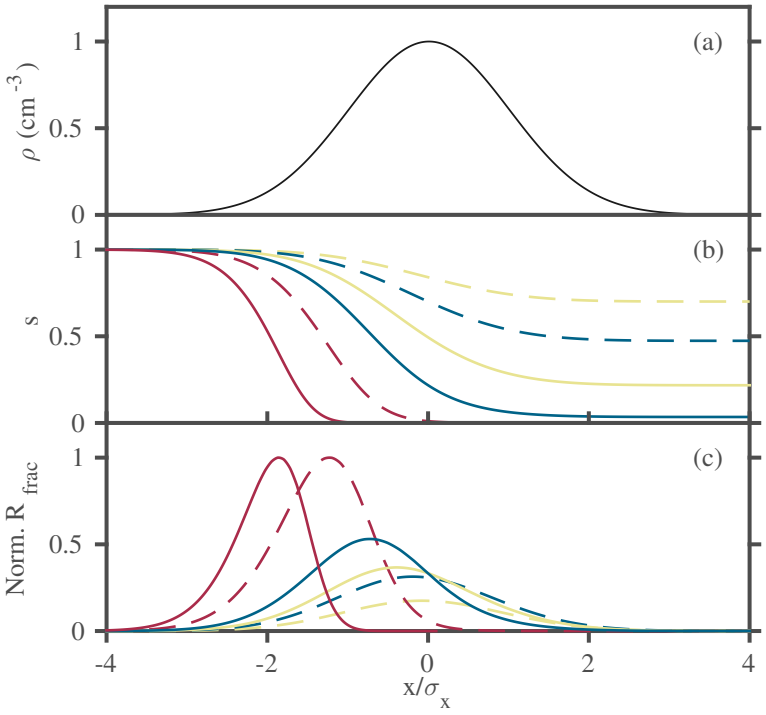

FIGURE 4.16: The variation of a) the ground state density, b) the probing laser intensity, and c) The number of Rydberg excitations, as a function of position. The curves represent optical depths of $b = 25, 5, 1, 0.1$ for red, blue, purple, and yellow respectively. Two geometries for each optical depth are shown, dashed lines are typical Narrowband MOT sample geometries and solid lines are Broadband MOT geometries. To allow the depth of penetration and distributions to be directly compared the position is normalised by the simulated cloud width.

That a saturation of the ion signal similar to that expected from the blockade can occur just due to optical depth effects is an important result. To understand the mechanism behind this saturation Figure 4.16 is instructive. It is clear that due to the beam's

rapid attenuation in high density samples, a point is reached where each photon has been 'used'. This depletion of the probe beam after a well defined optical depth is the origin of the saturation. The illuminated depth (and therefore volume) is inversely proportional to the density, while the number of Rydberg atoms per unit volume is directly proportional to density. These two competing effects mean the total number of Rydberg atoms tends to a constant.

These effects have implications for the blockade too. If the many-body interaction is beginning to limit the excited state population [89], then ground state atoms that lie within R_b of an excitation can continue to scatter photons and deplete the probe beam without yielding an increased Rydberg population. In this way, for increasingly dense samples, one would expect to see the ion signal peak and then begin to drop, allowing observation of both the optical depth saturation mechanism and the many-body mechanism.

4.4 Density Dependent Rydberg Temporal Dynamics

As the optical depth of the cloud yields a saturation in Rydberg signal, it stands to reason that this saturation is a poor indicator of the Rydberg blockade under our conditions. These same conditions that are required to create large ensembles of Rydberg atoms are the same sample characteristics that cause rapid attenuation of the probe beam. This could of course be countered by moving to an off-resonant excitation, where rescattering would be strongly suppressed, or by changing the sample geometry to lower the optical depth while maintaining the peak density. Unfortunately both of these solutions are technically challenging and so other experimental signatures must be investigated. One possibility is to look to observe many-body effects in the excitation dynamics of the ensemble [33]. The following presents a study into these excitation dynamics.

As a starting point, it is worth looking at the rate equation model discussed in 2.2.2. This model was used, with the aid of Dr. Bea Olmos, to investigate the time evolution of the Rydberg population under realistic experimental conditions and the output of these simulations is shown in Figure 4.17. The time dynamics are clearly not independent of density and the Rydberg population in the higher density curves saturates more quickly.

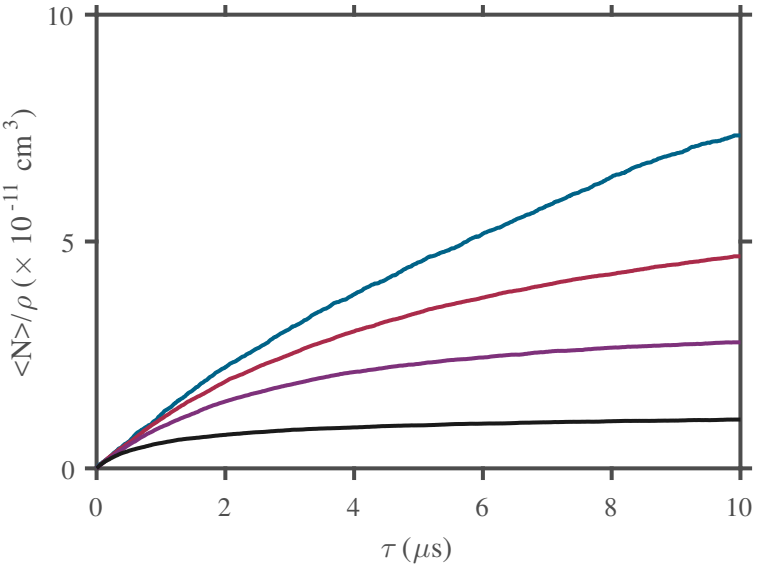

FIGURE 4.17: The time evolution of the Rydberg population as predicted by the rate equation model for a range of densities. The solid blue, red, purple, and black lines correspond to ground state densities of $\rho = (0.05, 0.2, 0.5, 2) \times 10^{11}\,\mathrm{cm}^{-3}$ respectively. The Rydberg populations are scaled by the simulated ground state densities as discussed in the text.

In this dissipative model, the faster onset of saturation at higher densities occurs due to the chance of excitation scaling proportionally with the number of ground state atoms. In Figure 4.17 the Rydberg population has been normalised by the ground state density, thus the initial gradient of all of the curves is the same. The Rydberg populations in the high density curves quickly reach the limit imposed by the Rydberg blockade and saturate. This is the dissipative analogue of the speed up of excitation seen in coherent systems. In such systems the effective increase in Rabi frequency, seen in collective Rabi oscillations, are the cause but these effects are not included in the simulation as the coherences are neglected. In both cases these speed up effects are directly related to the saturation of excitation.

To test this model and measure the dynamics of the excitation to the $5s48s\ ^1S_0$ Rydberg state, we followed the procedure discussed in Section 3.4. The autoionisation laser was again kept focused to try and reduce the effect of density averaging and the excitation pulse length was varied to map out the time dependence of the excitation.

The result of two such experiments are shown in Figure 4.18. Like the data presented in Section 4.2.4, this data was taken in a Broadband sample. The datasets are scaled by their peak densities to make them easily comparable. It is clear that the higher density curve saturates much more quickly and to quantify this the curves are fitted with an

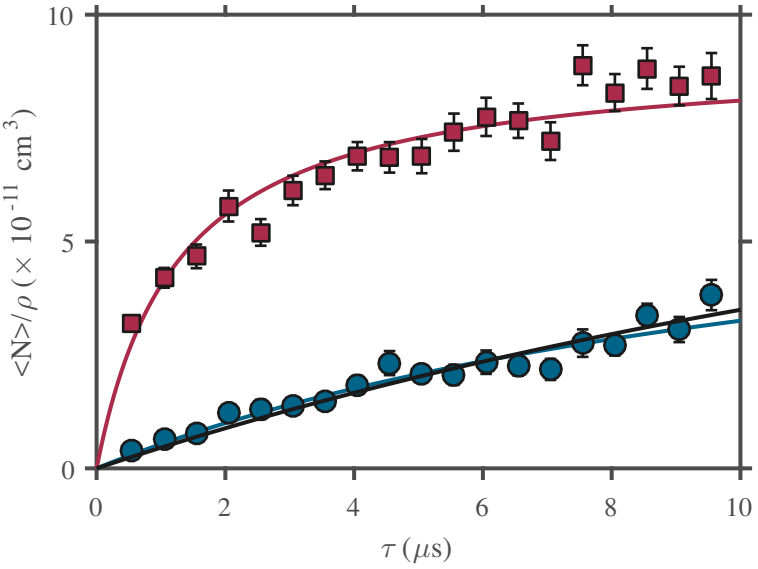

FIGURE 4.18: Average ion signal as a function of excitation time for a sample of density $\rho = 1 \times 10^{11}\,\mathrm{cm}^{-3}$ (red points) and $\rho = 8. \times 10^{11}\,\mathrm{cm}^{-3}$ (blue points). The solid lines represent a saturation fit to the data. Both datasets have been scaled by their ground state densities.

exponential saturation function of the form $A/(1 - \exp(-x/\tau_c))$. This fit function is predicted by the OBE model and from this fit a time constant τ_c can be extracted. Figure 4.19 shows how this time constant varies as a function of peak sample density. The OBE based optical depth model does not contain any evidence of a speed-up, suggesting this is an interaction based effect.

If the sample were blockaded in a non-dissipative ensemble then one would expect the relationship between the number of atoms per blockade sphere N_b and the time required to drive the ensemble to saturation to follow a $\sqrt{N_b}$ [90] dependence. In the dissipative limit this relation is less well defined and depends strongly upon the density averaging taking place within the Rydberg ensemble. Based upon the linear fit to the loglog plot in Figure 4.19 this relationship is actually $N^{-1.3}$, indicating that the speed up is much more pronounced than expected. Additionally, when this experiment is carried out in a Narrowband MOT (where the sample geometry is 3× smaller) no significant density dependence is observed.

The lack of a speed up in the Narrowband experiment is difficult to explain. While density averaging does play a role, this effect is difficult to quantify without performing a full many-body Monte Carlo simulation like that detailed in Section 2.2.2, extended to include optical depth. What should be noted is that the slowest time measured in

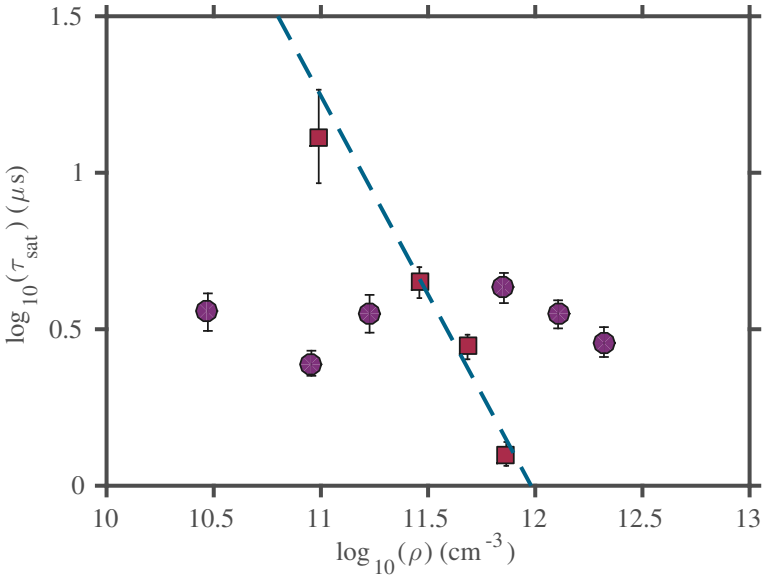

FIGURE 4.19: A log-log plot of the saturation time as a function of density for cloud lengths of 125 μm (red squares) and 38 μm (purple circles). The points for the 125 μm case are fitted with a linear trend line (dashed blue line) which indicates a scaling of $N^{-1.3}$.

the case of the Broadband MOT is consistent with the saturation time predicted by the OBE model. This saturation time is not however consistent with the saturation time of the lowest density Narrowband experiment.

Due to the propagation effects discussed in Section 4.3, the ground state density at which most of the Rydberg excitation occurs is not the peak density but is in fact lower by an amount that depends on the optical thickness. Therefore, while the optical depth code cannot accurately predict the time dynamics once the sample becomes interacting, it can still be used to provide insight into the sample density. Both the simulated weighted average of the density felt by the coherently excited Rydberg ensemble ρ_{avg} and the density at which the peak of the Rydberg distribution sits ρ_{rmax} can be estimated in this way.

The aforementioned analysis was carried out for the experiments shown in Figure 4.19. The results for the lowest density Broadband sample and a Narrowband sample of similar peak density are shown in Table 4.1. These simulations indicate that while the average density experienced by a Rydberg atom in both samples is less than peak density, the difference is similar and thus cannot explain the discrepancy between the observed saturation times.

TABLE 4.1: A comparison of the various density measures obtained from the optical depth simulation. The waist refers to the Gaussian waist of the atom sample in the probe beam propagation direction, ρ is the peak measured density of the ground state distribution, ρ_{avg} is the average density weighted by the simulated Rydberg atom distribution, and finally ρ_{rmax} is the ground state density at the location of the peak of the simulated Rydberg distribution.

Sample	Waist (μm)	ρ ($\times 10^{10}\,\mathrm{cm}^{-3}$)	ρ_{avg} ($\times 10^{10}\,\mathrm{cm}^{-3}$)	ρ_{rmax} ($\times 10^{10}\,\mathrm{cm}^{-3}$)
Narrowband	42.0	9.0	6.4	8.9
Broadband	145.0	9.8	6.5	7.7

As previously discussed but not considered thus far, the densest samples will still have two different Rydberg populations arriving from the multiple scattering process. This could help explain the discrepancy in the Narrowband results although no plausible mechanism is forthcoming. To rule out this effect, and to test whether what we are seeing is actually the laser excitation or Pedestal Rydberg atoms that are giving the speed up signature, an experiment like that presented in Figure 4.12 would have to be performed for a range of densities. This cleaner experiment would allow the two components to be separated via fitting to the spectra and their time dynamics extracted in isolation. While one would expect that the Pedestal Rydberg atoms have a higher blockade density (due to the larger excitation bandwidth) they will exist within the higher density regions of the cloud. The laser excited Rydberg atoms conversely have lower blockade densities but sit at lower density. Indeed Figure 4.12 already demonstrates that the two components have different temporal dynamics. The competition between these two effects means we can not safely neglect either population, making any time-resolved measurement that doesn't also have full spectral information difficult to interpret, but the preliminary data does suggest that the blockade and multiple scattering co-exist within the sample.

4.5 Spatial Experiments

One of the features of working with the $5s48s\,^1S_0$ state is that its interactions are both isotropic and attractive. One would expect that any Rydberg gas of such atoms would rapidly ionise as the atoms collide [91], but from previous data this does not seem to be the case. In all previous experiments the SNR between the autoionised ions and the spontaneous ions has remained favourable (> 10) under all previously

discussed experimental parameters. To test this further the lifetime can be considered, If collisional ionisation is taking place one would expect the measured lifetime to be sensitive to this effect and shortened accordingly.

To measure the lifetime of the $5s48s\,^1S_0$ Rydberg state, the delay between Rydberg creation and autoionisation was varied. The autoionisation laser was kept focused to guarantee ionisation with unit probability and the excitation time was fixed at 5 μs.

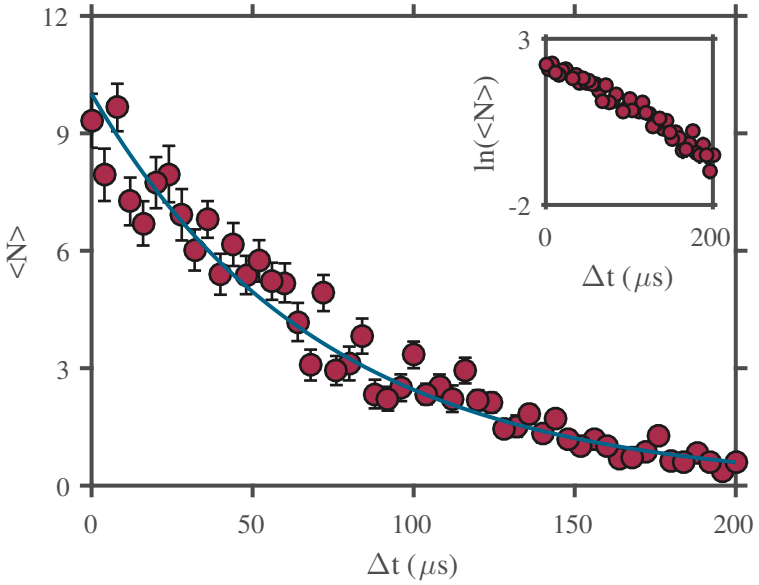

FIGURE 4.20: The Rydberg signal as a function of post excitation wait time Δt (red circles) and an exponential fit to these points (blue line) which yields a lifetime of 71 μs. Inset: The same data as the main panel but on a logarithmic scale to display the multiple exponential components.

The results of the above experiment are shown in Figure 4.20. The theoretical lifetime of this state based upon the work detailed in [21] is 48 μs compared to the experimentally measured lifetime of $(71 \pm 1)\,\mu$s. This discrepancy could be the result of the Rydberg atoms redistributing to other nearby states of higher angular momentum (which are generally longer lived) or poor spectroscopic data limiting the accuracy of the theoretical lifetime. Redistribution has been previously observed [19] and can manifest as a double exponential in the state lifetime which we do not observe.

If the ensemble is stable for the lifetime of the Rydberg state and we believe that there is no appreciable state transfer, then one must explain why the cloud is not collapsing under the attractive interaction. To investigate any possible mechanical effect due to the many-body interaction one can perform an experiment where the autoionisation beam is scanned across the sample to build up a map of the spatial distribution of the

atoms. The spatial distribution of the sample after various free evolution times can then be compared to see if there is indeed any sign of collapse.

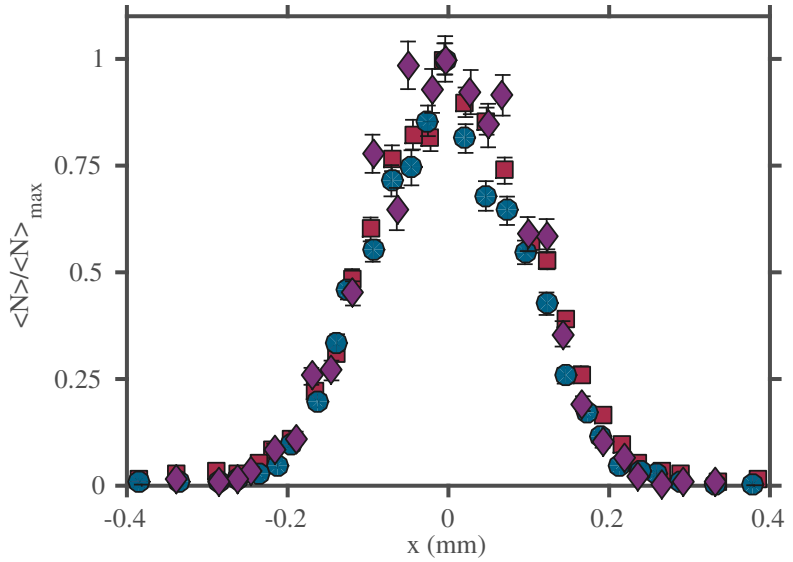

FIGURE 4.21: The Rydberg signal as a function of position for three different post excitation wait times with the data normalised to allow easy width comparison. The wait times are 0 μs, 20 μs, and 60 μs given by the red squares, blue circles and purple diamonds respectively. The density was constant at $\rho = (3 \pm 1) \times 10^{11}\,\mathrm{cm}^{-3}$, it had a width of 70 μm giving an optical depth of $b = 10$.

It is possible to translate the lens system to scan the beam across the sample [9]. This translation is done stepwise, not continuously, with the experiment repeated for each new autoionisation beam location. In this way the spatial profile can be measured with a resolution given by the waist of the scanned beam $(6 \pm 1)\,\mu$m. Unlike previous implementations of the technique, in the following experiments the compensation coils were instead used to shift the magnetic field zero within the chamber. The atom sample is translated linearly with compensation coil current in this way, with its position measured via the absorption image. While less accurate than translating the beam on a precision stage, utilising the compensation fields allows the sample to be easily translated in all three dimensions and drastically increases the experiment sample rate.

The results of the above experiment are presented in Figure 4.21. It is clear from the data that there is no significant change in the cloud profile over the range of free evolution times investigated and there could be several reasons for this. While the many-body interaction is attractive, it is still accompanied by a Rydberg blockade type effect, where a minimum possible separation between neighbouring Rydberg atoms is

established. The prevention of close Rydberg pairs forming will impose some minimum collision time, which if great enough, could effectively stabilise the cloud on the timescale of the Rydberg lifetime. Additionally, the density averaging caused by the optical depth effects will play a role. Interestingly Figure 4.22 shows that the Rydberg atoms do not have the same spatial profile as the ground state atoms, indeed it is wider, an effect that can be explained using the optical depth model.

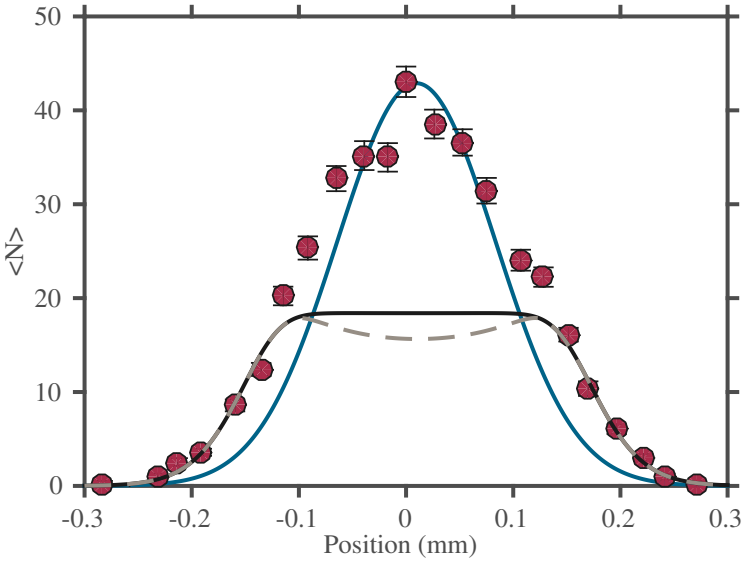

FIGURE 4.22: The Rydberg signal as a function of position for a standard 5 μs excitation (red circles). The result of the optical depth simulation of this sample using the parameters obtained from the low density fit for the blockade radii of $\rho_b = 4\times10^{10}$ cm^{-3} (black solid line) and $\rho_b = 0.4\times10^{10}$ cm^{-3} (grey dashed line). For reference the ground state distribution is also shown (solid blue line).

In addition to allowing us to model the effect of density on the excitation, the optical depth model also contains significant spatial information about the Rydberg distribution. The distribution predicted by the model is shown in Figure 4.22. It should be noted that this simulation again has no free parameters. The simulation reproduces the low density wings of the profile well, as multiple scattering is not the dominant effect. Towards the middle of the distribution we see a departure from the model. Here the laser attenuation limits the total Rydberg number giving us the flat topped profile. The data does not follow this profile as the Pedestal Rydberg atoms are not contained within this model thus the Rydberg population at the sample centre is underestimated. This deviation suggests that the Pedestal Rydberg atoms are indeed located at the centre of the atom sample, in the high density region. Again blockade effects can manifest in this regime but their signature will be obscured by the second Rydberg population.

To fully understand the Pedestal spectral, temporal and spatial characteristics of this system, one would need to build a model that does the following:

- Models the attenuation of the probing laser and the rescattering of the resulting photons.
- Accounts for the geometry of the sample and its effect on the trapping.
- Applies the correct transfer function to obtain the Rydberg population from the intermediate state population.
- Takes into account the heating of the sample in a way that allows redistribution to occur.
- Allows both inelastic and elastic scattering of photons.

This model is unfortunately beyond the scope of this thesis.

Summary

During this chapter the first observations of a trapped photon population leading to Rydberg excitation have been presented. This is evidenced by a symmetric broadening of the excitation spectrum and the clear two component character of the data and the Mandel Q analysis. The spectra were fitted and the two components isolated for individual analysis.

Considering the Narrow component, an OBE based model was benchmarked and then used successfully to model the data in the absence of this multiply scattered Pedestal contribution in the low density limit. This Narrow component was shown to saturate, an effect that can be attributed to the optical depth of the sample rather than the Rydberg blockade.

Analysis of the multiply scattered Pedestal component of the spectra suggest that the second photon population, arising from multiple scattering, consists of photons that have been inelastically scattered and have a linewidth of the order of the natural linewidth of the intermediate state ($2\pi \times 30.2\,\mathrm{MHz}$). It has also been demonstrated

that these Pedestal Rydberg atoms can manifest in the spatial profile of the excitations, logically explaining deviations from modelled spatial profiles.

Finally an excitation speed-up was measured that is not contained within the OBE model and is indicative of a many-body interaction. These results will be published and the article is currently in preparation [36].

Chapter 5

Conclusions and Outlook

To summarise, in this thesis we have demonstrated that multiple scattering may play a role in dense Rydberg gases, and that it can coexist with co-operative effects due to Rydberg-Rydberg interactions. These investigations have been facilitated by improvements in ground state imaging of the atom samples, allowing more reliable imaging of higher density samples, and also by improved control of the chamber electric field environment.

Rydberg population spectra as a function of probe detuning, at a range of optical depths, were measured and new features were seen to arise in the spectra of optical depths of $b > 1$. Subsequent analysis of the spectra using a mixture of OBE modelling and phenomenological fitting allowed the behaviour of this emergent feature to be studied. This behaviour was found to be consistent with frequency redistribution arising from a significant trapped photon field within the atom sample. This trapped field was also observed through the rapid heating of the atom sample during the excitation pulse.

We conclude that observed frequency redistribution of trapped photons is likely to be important for quantum logic gates, Rydberg non-linear optics, and single-photon sources. In these systems, where the probe laser fields are weak, the Rydberg excitations created by multiple scattering could provide additional dephasing mechanism and possibly limit the achievable fidelities. However, for optical transistors, where the aim is to use a single photon to switch a strong classical pulse [7, 8], the effect may well be much more significant. Most importantly though, this work demonstrates for the first time a technique that is capable of probing the spectrum of a trapped photon field.

Previously, only the spectrum of the escaping light has been measurable [92], which has limited investigations into the process.

Using our spatially resolved detection technique, we have shown it becomes possible to map out the distribution of the rescattered field. In this way we identified an anomalous population of Rydberg atoms that can be associated with excitation from the trapped radiation field. Further refinement of the technique would enable the study of such effects as photon bubble formation [93], while transient effects can be studied using long-lived metastable states to prolong the trapped field lifetime.

Finally, we have demonstrated that even in the presence of the trapped radiation field, it is still possible to observe signatures of Rydberg-Rydberg interactions. This was observed as a speed up of the excitation dynamics, exhibiting a higher co-efficient than the $\sqrt{N}$ expected [94].

5.1 Outlook

This thesis has demonstrated an extremely well characterised experimental setup and a comprehensive toolkit for measuring and characterising Rydberg excitation in dense samples. This following section will aim to show how these can be used going forwards, the types of physics that can be investigated, and the progress made towards these aims. Broadly speaking they focus around three key themes: photon trapping, Bose-Einstein condensation, and Rydberg dressing. The outlook for these three strands will now be discussed.

5.1.1 Photon Trapping

As the techniques developed within this work are currently the only way to probe the spectral and spatial profile of photons trapped within a cold atom sample there is a lot of scope for further investigation. There are many follow-up experiments that have been suggested throughout this work and summarised, future directions could include:

Isolated Pedestal spectra Pedestal information has so far been extracted through fitting a gestalt spectrum. One could exploit the photon trapping effect to excite

Rydberg atoms without laser photons present by extinguishing the probe beam prior to carrying out Rydberg excitation. This would allow a cleaner measurement of the trapped field spectrum and spatial profile and is a logical extension of the current technique. To enable this, the AOM switching times and MCP detector efficiency would to be improved. This could be acheived through the optimisation of the current setup and using narrower beam waists within the double pass AOMs.

Spatial dependence of the spectrum The spectrum of the trapped photons is set by the redistribution mechanism. These distribution mechanisms are all density dependent and one would expect to see a variation of the measured spectra as a function of the distance from the sample centre. As photons further from resonance are less well trapped, then one might expect the spectra taken further from the centre of the sample would be broader and thus the Rydberg atoms created in these regions to have smaller blockade radii. An understanding of the importance of such effects could feed into any future modelling of the dephasing created by photon trapping.

Density dependence of the spectrum The trapped field intensity should be self-limiting as saturation of the intermediate state should lower the optical depth. Experimental confirmation of this saturation for various sample geometries would be a useful benchmark for any future photon trapping model and help estimate the significance of the effect in other samples.

Rydberg state n variation In this work the Rydberg blockade radius is of similar length to the mean free path of a photon in the densest clouds. Exploring the extremal regimes in optically thick samples could highlight interesting interplays between coherent and cooperative atomic effects. In high n samples a regime could be entered whereby a single photon is able to scatter from multiple ground state atoms *within* the same superatom. In the low n limit, the quicker Rydberg excitation dynamics might allow the build up of the photon field to be measured as a function of time.

All of these experiments can be performed without significant modification to the current experimental setup. One evolution of the setup that could be envisioned is a move

towards Bose-Einstein condensation and the investigation of Rydberg excitation and photon trapping within such a sample.

5.1.2 Bose-Einstein Condensation

As discussed in Section 1.1, strontium is a prime candidate for condensation due to the performance of narrow line cooling and the convenient scattering properties of ^{84}Sr [95]. It is only the natural abundance of the ^{84}Sr isotope that makes strontium less attractive. The use of a magnetic trap to create a $5s5p\,^3P_2$ metastable reservoir [96] has all but eliminated this constraint and paved the way for the rapid creation of large BECs [97]. A feasibility study has been conducted to measure the lifetime of the magnetic trap formed by the Durham experiment MOT coils. This lifetime is shown in Figure 5.1.

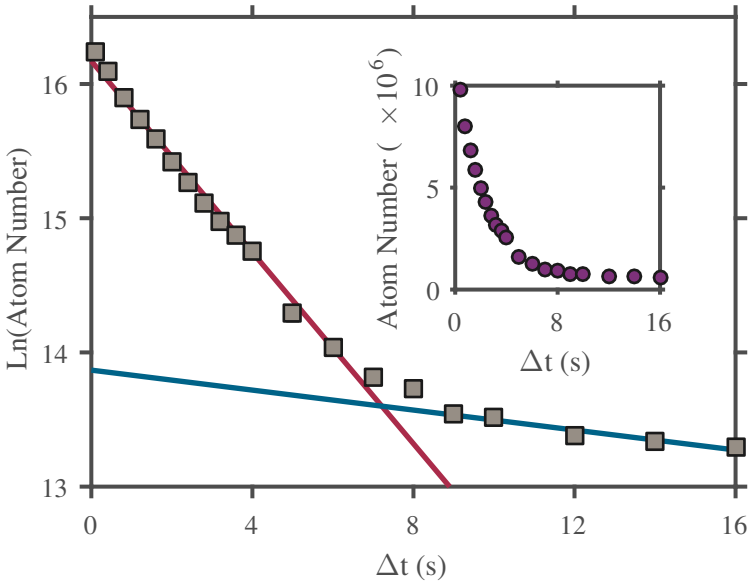

FIGURE 5.1: Log of the magnetic trap population as a function of the magnetic trap hold time Δt. Atoms were loaded into the magnetic trap through the slow decay from the blue MOT via the $5s5d\,^1D_2$ state. Atoms were repumped back to the ground state using the repump lasers after the hold time and then imaged. The two fits yield trap lifetimes of 2.8 s and 27 s for the solid red and solid blue lines respectively. Inset: The raw atom number within the magnetic trap as a function of time.

To measure the lifetime the reservoir was loaded via decay from the $5s5d\,^1D_2$ state. The blue MOT light was then extinguished and the MOT coils left on for a variable hold time. Finally the trap was depopulated by the 689 nm and 707 nm repump lasers and the resulting ground state atoms imaged. The measurements showed a two component exponential decay. At short times the trap lifetime is measured to be 2.8 s and at long

times it is 27 s. The reason for measuring two lifetimes is not clear but it should be noted that the lifetime will be shortened by leaked repump light. Regardless, even at 2.8 s, the lifetime of the trap is sufficient to use as a reservoir. It was found that up to 1×10^6 atoms could be loaded and the trap temperature was measured to be $\sim 300\,\mu$K. The trapped atom number is likely limited by the trapping field gradient. The strontium MOT coils operate at an axial field gradient of $25\,\mathrm{G.cm^{-1}}$, which is lower than most other strontium groups. This is unlikely to prove a limitation as the gradient could be increased at the expense of the coil duty cycle.

If a strontium BEC were to be realised in Durham then this would provide an interesting environment from which to study Rydberg excitation. Such systems have been proposed as a possible route to achieving a supersolid [98] and it demonstrated that a single Rydberg atom can modify its host BECs spatial distribution [99]. It has also been hypothesised that the creation of BECs could be facilitated by Rydberg dressing. By creating a coherent admixture of Rydberg atoms and ground state atoms, one can create a dynamically tunable effective interaction [98, 100] and strontium provides an ideal system within which to study this phenomenon.

5.1.3 Rydberg Dressing

A weak Rydberg excitation can be used to 'dress' the ground state. In this way an admixture of the ground and Rydberg states is created and an effective interaction between ground state atoms is created [100]. Such systems have been experimentally realised [101, 102]. Key to this process is the minimisation of the intermediate state population, scattering from which adds dissipation to the system and destroys the atomic coherences on which dressing relies. To minimise the intermediate state population, while maintaining an appreciable two-photon Rabi frequency, one must detune the probe laser by many times the intermediate state linewidth. This is technically challenging with the $5s5p\,{}^1P_1$ state. The very characteristics that make this system an ideal one in which to study dissipative systems make it unfavourable to study dressed systems. Fortunately strontium has triplet states.

Utilising the $5s5p\,{}^3P_1$ state as the intermediate state in a three-level ladder type scheme one can excite to triplet, rather than singlet, Rydberg states. With the chamber windows replaced this move is now possible and if one were to excite to Rydberg states via

triplet states, then the narrow linewidth makes detuning from the intermediate state trivially achievable with a standard AOM. Minimising the scatter from the intermediate state has a second advantage in that it will minimise photon trapping effects which would otherwise disrupt the dressing process. Unfortunately, the excitation itself is not trivial as access to Rydberg states from this intermediate state requires a UV laser at 319 nm.

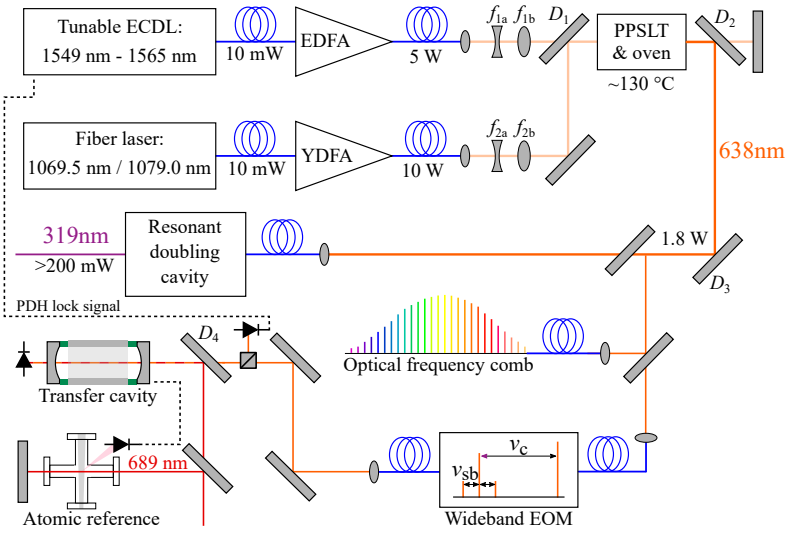

FIGURE 5.2: Schematic diagram of the UV laser system. A PPSLT crystal is used to sum the output of two infra-red lasers at wavelengths of 1549 nm and 1079 nm. The resulting light at 638 nm is frequency doubled to produce > 200 mW at 319 nm. The laser frequency is locked to the same transfer cavity that stabilises the intercombination line laser at 689 nm. A wideband EOM is used to bridge the frequency gap between the cavity mode and the Rydberg transition. The laser frequency is measured on a GPS-referenced optical frequency comb. (EDFA = Er-doped fibre amplifier, YDFA = Yb-doped fibre amplifier. D1-D4 = dichroic mirrors). Figure reproduced from reference [45].

The Durham group has recently finished development of such a laser system, based on telecoms wavelength fibre technology [103]. A schematic of this system is shown in Figure 5.2, which is reproduced from reference [45]. This system has a measured linewidth of ~ 35 kHz. This narrow linewidth, used in conjunction with the narrowed red MOT laser and a frequency comb, allows for precision spectroscopy of the Rydberg states. Work on such spectroscopy is already under way in an effort to characterise the excitation scheme.

Preliminary spectroscopic results have already been published [45] and some of these results are reproduced in Figure 5.3. These results demonstrate the versatility of the developed laser system, capable of taking spectra continuously over large detuning

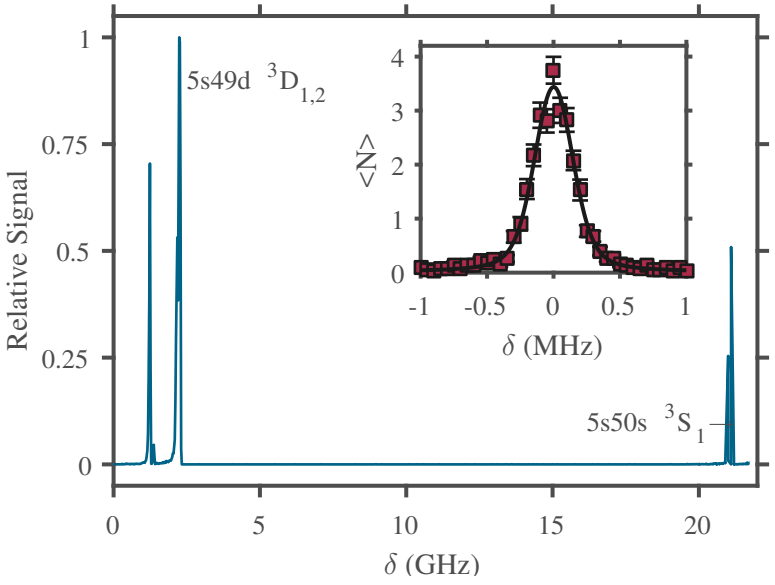

FIGURE 5.3: Ion signal obtained from continuous scans of the UV detuning (measured relative to the start of the scan) in the region around n = 50. The intensities used for the excitation are $\sim 20\,\mathrm{mW.cm^{-2}}$ and $\sim 1\,\mathrm{W.cm^{-2}}$ for the 689 nm and UV beams respectively. Each beam is larger than the size of the atom cloud. The variation in signal height across the scan is largely due to depletion of atoms from the MOT and is not an indication of transition strength. The frequency axis of the scans is calibrated on the High Finesse wavemeter. Inset: High resolution scan of the $5s37s\,^3S_1$ state. The solid black line shows a Voigt profile fit. The intensities used for the excitation are $\sim 0.1\,\mathrm{mW.cm^{-2}}$ and $\sim 250\,\mathrm{mW.cm^{-2}}$ for the 689 nm and UV beams respectively, and each beam is larger than the size of the atom cloud. The central frequency of this feature is at ~ 939.274 THz.

ranges (> 24 GHz), being able to access a wide range of strontium n states (n=35-300), and measuring precision spectra (an order of magnitude narrower than previous spectra). Once characterised, these Rydberg states can be harnessed to explore Rydberg dressing and potentially used to realise spin squeezing in an optical lattice clock [10].

Another exciting investigation that is being considered is to utilise the dressed interaction to engineer the scattering length of atoms in an optical dipole trap [104]. The scattering length of the strontium ^{88}Sr isotope is unfavourable for BEC creation ($-1\,a_0$). One could engineer the scattering length of an ^{88}Sr ensemble such that thermalisation could occur, then this could provide a route to a ^{88}Sr BEC that did not require sympathetic cooling techniques [105]. Based on references [98, 106] a model was developed that uses the Rydberg dressed interaction potential to calculate an effective scattering length and the elastic collision rate for a dressed dipole trapped sample. Results from these simulations are shown in Figure 5.4(a) and demonstrate that, for achievable experimental conditions, a wide range of elastic scattering lengths could be engineered.

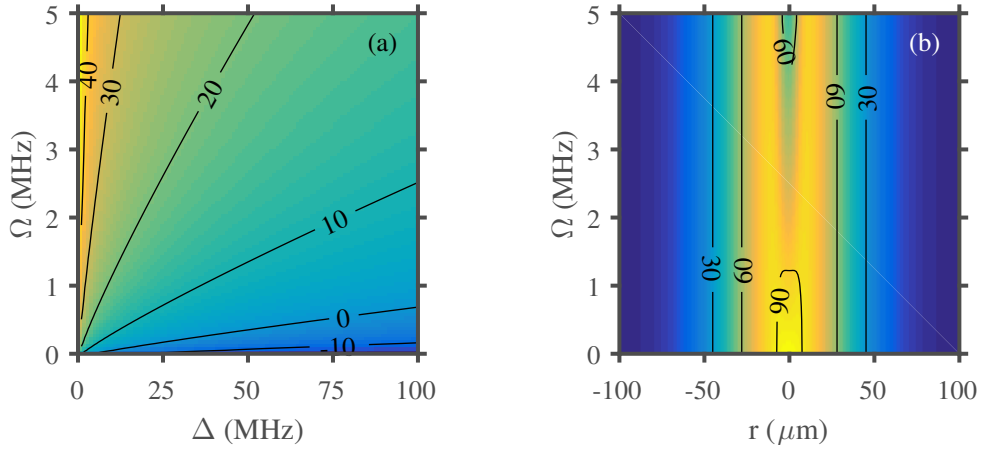

FIGURE 5.4: (a) The variation of the log of the elastic scattering rate as a function of the two-photon Rabi frequency Ω and the detuning from the intermediate state Δ. Calculations performed for the $5s50s\,^3S_1$ state in a 1070 nm dipole trap at 10 W with a waist of 60 μm. The two photon Rabi frequency is varied with the UV laser power alone. The UV beam waist is fixed at 10 μm while the probe beam has a waist of 100 μm and a power of 1 mW. (b) The variation of the dipole trap depth (in μK) as a function of the two-photon Rabi frequency Ω and position r. The parameters for this calculation are the same as in the previous sub-figure.

While modelling various dipole traps during this investigation it was quickly realised that the UV excitation laser is anti-trapping. To model how this would distort the dipole trap a summative approximation was adopted [107] whereby the two trapping potentials are calculated independently and then combined. As can be seen in Figure 5.4(b), there is a significant weakening and distortion of the trap for high UV laser powers. This indicates that strong dressing will be difficult to achieve without perturbing the sample. However, as the combined Figure 5.4 shows, significant elastic collision rates can be achieved without significant perturbation of the trap and it remains an exciting potential future direction.

Bibliography

[1] J. Rydberg, *On the structure of the line-spectra of the chemical elements*, The London, Edinburgh, and Dublin Philosophical Magazine and Journal of Science **29**, 331 (1890).

[2] T. F. Gallagher, *Rydberg Atoms* (Cambridge University Press, 1994), Cambridge Books Online.

[3] I. Friedler, D. Petrosyan, M. Fleischhauer, and G. Kurizki, *Long-range interactions and entanglement of slow single-photon pulses*, Phys. Rev. A **72**, 043803 (2005).

[4] D. Paredes-Barato and C. S. Adams, *All-Optical Quantum Information Processing Using Rydberg Gates*, Phys. Rev. Lett. **112**, 040501 (2014).

[5] A. V. Gorshkov, J. Otterbach, M. Fleischhauer, T. Pohl, and M. D. Lukin, *Photon-Photon Interactions via Rydberg Blockade*, Phys. Rev. Lett. **107**, 133602 (2011).

[6] S. D. Hogan *et al.*, *Driving Rydberg-Rydberg Transitions from a Coplanar Microwave Waveguide*, Phys. Rev. Lett. **108**, 063004 (2012).

[7] D. Tiarks, S. Baur, K. Schneider, S. Dürr, and G. Rempe, *Single-Photon Transistor Using a Förster Resonance*, Phys. Rev. Lett. **113**, 053602 (2014).

[8] H. Gorniaczyk, C. Tresp, J. Schmidt, H. Fedder, and S. Hofferberth, *Single-Photon Transistor Mediated by Interstate Rydberg Interactions*, Phys. Rev. Lett. **113**, 053601 (2014).

[9] G. Lochead, D. Boddy, D. P. Sadler, C. S. Adams, and M. P. A. Jones, *Number-resolved imaging of excited-state atoms using a scanning autoionization microscope*, Phys. Rev. A **87**, 053409 (2013).

[10] L. I. R. Gil, R. Mukherjee, E. M. Bridge, M. P. A. Jones, and T. Pohl, *Spin Squeezing in a Rydberg Lattice Clock*, Phys. Rev. Lett. **112**, 103601 (2014).

[11] S. Blatt *et al.*, *New Limits on Coupling of Fundamental Constants to Gravity Using* ^{87}Sr *Optical Lattice Clocks*, Phys. Rev. Lett. **100**, 140801 (2008).

[12] T. H. Loftus, T. Ido, M. M. Boyd, A. D. Ludlow, and J. Ye, *Narrow line cooling and momentum-space crystals*, Phys. Rev. A **70**, 063413 (2004).

[13] X. Xu *et al.*, *Dynamics in a two-level atom magneto-optical trap*, Phys. Rev. A **66**, 011401 (2002).

[14] S. B. Nagel *et al.*, *Photoassociative Spectroscopy at Long Range in Ultracold Strontium*, Phys. Rev. Lett. **94**, 083004 (2005).

[15] B. J. Bloom *et al.*, *An optical lattice clock with accuracy and stability at the 10-18 level*, Nature **506**, 71 (2014).

[16] A. Derevianko, *Feasibility of Cooling and Trapping Metastable Alkaline-Earth Atoms*, Phys. Rev. Lett. **87**, 023002 (2001).

[17] J. Millen, G. Lochead, G. R. Corbett, R. M. Potvliege, and M. P. A. Jones, *Spectroscopy of a cold strontium Rydberg gas*, J. Phys. B: At., Mol. Opt. Phys. **44**, 184001 (2011).

[18] J. J. Mestayer *et al.*, *Realization of Localized Bohr-Like Wave Packets*, Phys. Rev. Lett. **100**, 243004 (2008).

[19] J. Millen, *A cold strontium Rydberg gas*, PhD thesis, Durham Univeristy, 2011.

[20] B. Bransden and C. Joachain, *Physics of Atoms and Molecules*Pearson Education (Prentice Hall, 2003).

[21] J. V. Christophe, Louis, *Long-Range Interactions in One- and Two-Electron Rydberg Atoms*, PhD thesis, Durham University, 2014.

[22] C. L. Vaillant, M. P. A. Jones, and R. M. Potvliege, *Long-range Rydberg–Rydberg interactions in calcium, strontium and ytterbium*, J. Phys. B: At., Mol. Opt. Phys. **45**, 135004 (2012).

[23] A. Schwettmann, K. R. Overstreet, J. Tallant, and J. P. Shaffer, *Analysis of long-range Cs Rydberg potential wells*, Journal of Modern Optics **54**, 2551 (2007).

[24] A. Dalgarno and W. Davison, *The Calculation of Van Der Waals Interactions*, in ., edited by D. Bates and I. Estermann, volume 2 of *Advances in Atomic and Molecular Physics*, pp. 1 – 32, Academic Press, 1966.

[25] R. J. Leroy and R. B. Bernstein, *Dissociation energies of diatomic moleculles from vibrational spacings of higher levels: application to the halogens**, Chemical Physics Letters **5**, 42 (1970).

[26] T. G. Walker and M. Saffman, *Consequences of Zeeman degeneracy for the van der Waals blockade between Rydberg atoms*, Phys. Rev. A **77**, 032723 (2008).

[27] M. D. Lukin *et al.*, *Dipole Blockade and Quantum Information Processing in Mesoscopic Atomic Ensembles*, Phys. Rev. Lett. **87**, 037901 (2001).

[28] C. Cohen-Tannoudji, J. Dupont-Roc, and G. Grynberg, *Atom-Photon Interactions*, Fourth ed. (Wiley-VCH, 2004).

[29] J. R. Ackerhalt and B. W. Shore, *Rate equations versus Bloch equations in multiphoton ionization*, Phys. Rev. A **16**, 277 (1977).

[30] S. Sultana and M. S. Zubairy, *Effect of finite bandwidth on refractive-index enhancement and lasing without inversion*, Phys. Rev. A **49**, 438 (1994).

[31] J. D. Pritchard, *Cooperative Optical Non-linearity in a blockaded Rydberg Ensemble*, PhD thesis, Durham University, 2011.

[32] C. Ates, T. Pohl, T. Pattard, and J. M. Rost, *Many-body theory of excitation dynamics in an ultracold Rydberg gas*, Phys. Rev. A **76**, 013413 (2007).

[33] B. Olmos, I. Lesanovsky, and J. P. Garrahan, *Out-of-equilibrium evolution of kinetically constrained many-body quantum systems under purely dissipative dynamics*, Phys. Rev. E **90**, 042147 (2014).

[34] M. Marcuzzi, J. Schick, B. Olmos, and I. Lesanovsky, *Effective dynamics of strongly dissipative Rydberg gases*, J. Phys. A: Math. Theor. **47**, 482001 (2014).

[35] C. Ates, T. Pohl, T. Pattard, and J. M. Rost, *Antiblockade in Rydberg Excitation of an Ultracold Lattice Gas*, Phys. Rev. Lett. **98**, 023002 (2007).

[36] D. P. Sadler *et al.*, *Multiple scattering in a dense cold Rydberg gas*, Unpublished.

[37] G. Lochead, *Excited state spatial distributions in a cold strontium gas*, PhD thesis, Durham University, 2012.

[38] D. Boddy, *First observations of Rydberg blockade in a frozen gas of divalent atoms*, PhD thesis, Durham University, 2014.

[39] I. Courtillot *et al.*, *Efficient cooling and trapping of strontium atoms*, Opt. Lett. **28**, 468 (2003).

[40] R. K. Raj, D. Bloch, J. J. Snyder, G. Camy, and M. Ducloy, *High-Frequency Optically Heterodyned Saturation Spectroscopy Via Resonant Degenerate Four-Wave Mixing*, Phys. Rev. Lett. **44**, 1251 (1980).

[41] D. J. McCarron, S. A. King, and S. L. Cornish, *Modulation transfer spectroscopy in atomic rubidium*, Meas. Sci. Technol. **19**, 105601 (2008).

[42] E. M. Bridge, J. Millen, C. S. Adams, and M. P. A. Jones, *A vapor cell based on dispensers for laser spectroscopy*, Rev. Sci. Instrum. **80**, 013101 (2009).

[43] R. P. Abel *et al.*, *Laser frequency stabilization to excited state transitions using electromagnetically induced transparency in a cascade system*, Appl. Phys. Lett. **94** (2009).

[44] Y. Li, T. Ido, T. Eichler, and H. Katori, *Narrow-line diode laser system for laser cooling of strontium atoms on the intercombination transition*, Appl. Phys. B **78**, 315 (2004).

[45] E. M. Bridge *et al.*, *Tunable cw UV laser with ∼35 kHz absolute frequency instability for precision spectroscopy of Sr Rydberg states*, Opt. Express **24**, 2281 (2016).

[46] C. Foot, *Atomic Physics*, First ed. (Oxford University Press, 2005).

[47] C. Dedman *et al.*, *Optimum design and construction of a Zeeman slower for use with a magneto-optic trap*, Rev. Sci. Instrum. **75**, 5136 (2004).

[48] B. O. Kock, *Magneto-optical trapping of strontium for use as a mobile frequency reference*, PhD thesis, University of Birmingham, 2013.

[49] G. Lamporesi, S. Donadello, S. Serafini, and G. Ferrari, *Compact high-flux source of cold sodium atoms*, Rev. Sci. Instrum. **84**, (2013).

[50] S. Stellmer, *Degenerate quantum gases of strontium*, PhD thesis, Innsbruk University, 2013.

[51] C. G. Townsend *et al.*, *Phase-space density in the magneto-optical trap*, Phys. Rev. A **52**, 1423 (1995).

[52] M. Boyd, *High Precision Spectroscopy of Strontium in an Optical Lattice: Towards a New Standard for Frequency and Time*, PhD thesis, Colorado University, 2007.

[53] T. Chanelière, J.-L. Meunier, R. Kaiser, C. Miniatura, and D. Wilkowski, *Extra-heating mechanism in Doppler cooling experiments*, J. Opt. Soc. Am. B **22**, 1819 (2005).

[54] H. Katori, T. Ido, Y. Isoya, and M. Kuwata-Gonokami, *Magneto-Optical Trapping and Cooling of Strontium Atoms down to the Photon Recoil Temperature*, Phys. Rev. Lett. **82**, 1116 (1999).

[55] Y. Castin, H. Wallis, and J. Dalibard, *Limit of Doppler cooling*, J. Opt. Soc. Am. B **6**, 2046 (1989).

[56] A. Ludlow, *The Strontium Optical Lattice Clock: Optical Spectroscopy with Sub-Hertz Accuracy*, PhD thesis, University of Colorado, 2008.

[57] A. Gürtler and W. van der Zande, *l-state selective field ionization of rubidium Rydberg states*, Phys. Lett. A **324**, 315 (2004).

[58] W. E. Cooke, T. F. Gallagher, S. A. Edelstein, and R. M. Hill, *Doubly Excited Autoionizing Rydberg States of Sr*, Phys. Rev. Lett. **40**, 178 (1978).

[59] J. Millen, G. Lochead, and M. P. A. Jones, *Two-Electron Excitation of an Interacting Cold Rydberg Gas*, Phys. Rev. Lett. **105**, 213004 (2010).

[60] P. McQuillen, X. Zhang, T. Strickler, F. B. Dunning, and T. C. Killian, *Imaging the evolution of an ultracold strontium Rydberg gas*, Phys. Rev. A **87**, 013407 (2013).

[61] T. Amthor, M. Reetz-Lamour, S. Westermann, J. Denskat, and M. Weidemüller, *Mechanical Effect of van der Waals Interactions Observed in Real Time in an Ultracold Rydberg Gas*, Phys. Rev. Lett. **98**, 023004 (2007).

[62] T. F. Gallagher and W. E. Cooke, *Interactions of Blackbody Radiation with Atoms*, Phys. Rev. Lett. **42**, 835 (1979).

[63] M. P. Robinson, B. L. Tolra, M. W. Noel, T. F. Gallagher, and P. Pillet, *Spontaneous Evolution of Rydberg Atoms into an Ultracold Plasma*, Phys. Rev. Lett. **85**, 4466 (2000).

[64] W. Li *et al.*, *Evolution dynamics of a dense frozen Rydberg gas to plasma*, Phys. Rev. A **70**, 042713 (2004).

[65] T. C. Killian *et al.*, *Creation of an Ultracold Neutral Plasma*, Phys. Rev. Lett. **83**, 4776 (1999).

[66] T. C. Killian *et al.*, *Absorption imaging and spectroscopy of ultracold neutral plasmas*, J. Phys. B: At., Mol. Opt. Phys. **38**, S351 (2005).

[67] T. Killian, T. Pattard, T. Pohl, and J. Rost, *Ultracold Neutral Plasmas*, Phys. Rep. **449**, 77 (2007).

[68] G. Reinaudi, T. Lahaye, Z. Wang, and D. Guéry-Odelin, *Strong saturation absorption imaging of dense clouds of ultracold atoms*, Opt. Lett. **32**, 3143 (2007).

[69] K. Singer, M. Reetz-Lamour, T. Amthor, L. G. Marcassa, and M. Weidemüller, *Suppression of Excitation and Spectral Broadening Induced by Interactions in a Cold Gas of Rydberg Atoms*, Phys. Rev. Lett. **93**, 163001 (2004).

[70] N. Malossi *et al.*, *Full Counting Statistics and Phase Diagram of a Dissipative Rydberg Gas*, Phys. Rev. Lett. **113**, 023006 (2014).

[71] T. C. Liebisch, A. Reinhard, P. R. Berman, and G. Raithel, *Atom Counting Statistics in Ensembles of Interacting Rydberg Atoms*, Phys. Rev. Lett. **95**, 253002 (2005).

[72] I. Hughes and T. Hase, *Measurements and Their Uncertainties: A Practical Guide to Modern Error Analysis* (OUP Oxford, 2010).

[73] D. W. Sesko, T. G. Walker, and C. E. Wieman, *Behavior of neutral atoms in a spontaneous force trap*, J. Opt. Soc. Am. B **8**, 946 (1991).

[74] A. M. Steane, M. Chowdhury, and C. J. Foot, *Radiation force in the magneto-optical trap*, J. Opt. Soc. Am. B **9**, 2142 (1992).

[75] A. Fioretti, A. F. Molisch, J. H. Müller, P. Verkerk, and M. Allegrini, *Observation of radiation trapping in a dense Cs magneto-optical trap*, Opt. Commun. **149**, 415 (1998).

[76] G. Labeyrie *et al.*, *Slow Diffusion of Light in a Cold Atomic Cloud*, Phys. Rev. Lett. **91**, 223904 (2003).

[77] G. Labeyrie, D. Delande, C. A. Müller, C. Miniatura, and R. Kaiser, *Multiple scattering of light in a resonant medium*, Opt. Commun. **243**, 157 (2004).

[78] R. Loudon, *The Quantum Theory of Light*, 3rd edition ed. (OUP Oxford, 2000).

[79] A. F. Molisch and B. P. Oehry, *Radiation trapping in atomic vapours* (Oxford University Press, 1998).

[80] G. Labeyrie *et al.*, *Coherent Backscattering of Light by Cold Atoms*, Phys. Rev. Lett. **83**, 5266 (1999).

[81] R. Pierrat, B. Grémaud, and D. Delande, *Enhancement of radiation trapping for quasiresonant scatterers at low temperature*, Phys. Rev. A **80**, 013831 (2009).

[82] B. R. Mollow, *Power Spectrum of Light Scattered by Two-Level Systems*, Phys. Rev. **188**, 1969 (1969).

[83] E. del Valle and F. P. Laussy, *Mollow Triplet under Incoherent Pumping*, Phys. Rev. Lett. **105**, 233601 (2010).

[84] UlhaqA. *et al.*, *Cascaded single-photon emission from the Mollow triplet sidebands of a quantum dot*, Nat. Photon **6**, 238 (2012).

[85] G. Labeyrie, R. Kaiser, and D. Delande, *Radiation trapping in a cold atomic gas*, Appl. Phys. B **81**, 1001 (2005).

[86] Q. Baudouin, N. Mercadier, and R. Kaiser, *Steady-state signatures of radiation trapping by cold multilevel atoms*, Phys. Rev. A **87**, 013412 (2013).

[87] A. K. Mohapatra, T. R. Jackson, and C. S. Adams, *Coherent Optical Detection of Highly Excited Rydberg States Using Electromagnetically Induced Transparency*, Phys. Rev. Lett. **98**, 113003 (2007).

[88] S. Mauger, J. Millen, and M. Jones, *Spectroscopy of strontium Rydberg states using electromagnetically induced transparency*, J. Phys. B: At., Mol. Opt. Phys. **40**, F319 (2007).

[89] D. Tong *et al.*, *Local Blockade of Rydberg Excitation in an Ultracold Gas*, Phys. Rev. Lett. **93**, 063001 (2004).

[90] A. Gaetan *et al.*, *Observation of collective excitation of two individual atoms in the Rydberg blockade regime*, Nat Phys **5**, 115 (2009).

[91] M. Viteau *et al.*, *Melting a frozen Rydberg gas with an attractive potential*, Phys. Rev. A **78**, 040704 (2008).

[92] F. Y. Wu, R. E. Grove, and S. Ezekiel, *Investigation of the Spectrum of Resonance Fluorescence Induced by a Monochromatic Field*, Phys. Rev. Lett. **35**, 1426 (1975).

[93] J. T. Mendonça and R. Kaiser, *Photon Bubbles in Ultracold Matter*, Phys. Rev. Lett. **108**, 033001 (2012).

[94] T. A. Johnson *et al.*, *Rabi Oscillations between Ground and Rydberg States with Dipole-Dipole Atomic Interactions*, Phys. Rev. Lett. **100**, 113003 (2008).

[95] Y. N. M. de Escobar *et al.*, *Bose-Einstein Condensation of* ^{84}Sr, Phys. Rev. Lett. **103**, 200402 (2009).

[96] S. Stellmer, M. K. Tey, B. Huang, R. Grimm, and F. Schreck, *Bose-Einstein Condensation of Strontium*, Phys. Rev. Lett. **103**, 200401 (2009).

[97] S. Stellmer, R. Grimm, and F. Schreck, *Production of quantum-degenerate strontium gases*, Phys. Rev. A **87**, 013611 (2013).

[98] N. Henkel, R. Nath, and T. Pohl, *Three-Dimensional Roton Excitations and Supersolid Formation in Rydberg-Excited Bose-Einstein Condensates*, Phys. Rev. Lett. **104**, 195302 (2010).

[99] J. B. Balewski *et al.*, *Coupling a single electron to a Bose-Einstein condensate*, Nature **502**, 664 (2013).

[100] T. Macrì and T. Pohl, *Rydberg dressing of atoms in optical lattices*, Phys. Rev. A **89**, 011402 (2014).

[101] M. Boll *et al.*, *Spin and Charge Resolved Quantum Gas Microscopy of Antiferromagnetic Order in Hubbard Chains*, ArXiv e-prints (2016), 1605.05661.

[102] T. Keating *et al.*, *Robust quantum logic in neutral atoms via adiabatic Rydberg dressing*, Phys. Rev. A **91**, 012337 (2015).

[103] A. C. Wilson *et al.*, *A 750-mW, continuous-wave, solid-state laser source at 313 nm for cooling and manipulating trapped 9Be+ ions*, Applied Physics B **105**, 741 (2011).

[104] R. Grimm, M. Weidemüller, and Y. B. Ovchinnikov, *Optical Dipole Traps for Neutral Atoms*, in *Advances In Atomic, Molecular, and Optical Physics*, edited by B. Bederson and H. Walther, volume 42 of *Advances In Atomic, Molecular, and Optical Physics*, pp. 95 – 170, Academic Press, 2000.

[105] P. G. Mickelson, Y. N. Martinez de Escobar, M. Yan, B. J. DeSalvo, and T. C. Killian, *Bose-Einstein condensation of* ^{88}Sr *through sympathetic cooling with* ^{87}Sr, Phys. Rev. A **81**, 051601 (2010).

[106] J. Honer, H. Weimer, T. Pfau, and H. P. Büchler, *Collective Many-Body Interaction in Rydberg Dressed Atoms*, Phys. Rev. Lett. **105**, 160404 (2010).

[107] B. Arora, M. S. Safronova, and C. W. Clark, *State-insensitive bichromatic optical trapping*, Phys. Rev. A **82**, 022509 (2010).